DESIGNING OUTER-SPHERE REDOX SHUTTLES AND INVESTIGATING EFFICIENCY LIMITING ELECTRON TRANSFER PROCESSES FOR THE ADVANCEMENT OF DYE SENSITIZED SOLAR CELLS

By

Yuling Xie

A DISSERTATION

Submitted to
Michigan State University
in partial fulfillment of the requirements
for the degree of

Chemistry – Doctor of Philosophy

2016

ABSTRACT

DESIGNING OUTER-SPHERE REDOX SHUTTLES AND INVESTIGATING EFFICIENCY LIMITING ELECTRON TRANSFER PROCESSES FOR THE ADVANCEMENT OF DYE SENSITIZED SOLAR CELLS

By

Yuling Xie

Dye sensitized solar cells (DSSCs) are considered as a promising alternative technology to harness the solar energy cost-effectively for the purpose of tackling the energy crisis and climate change. The complex but also unique construction of DSSCs offers various designs utilizing abundant and cheap materials. This dissertation focuses on the design and development of one important component in DSSCs, redox shuttles. A primary goal presented here is exploring alternative outer-sphere redox shuttles which are able to strike a balance between the two efficiency determining electron transfer processes in DSSCs, dye regeneration and electron recombination. Utilizing Marcus theory allows us to investigate the effects of the two processes on overall efficiency and introduce new route for redox shuttles design, i.e. introduction of low spin cobalt-based outer-sphere redox shuttles. Several routes to design low spin cobalt based redox shuttles are discussed. The systematic study of regeneration and recombination in terms of Marcus theory using these redox shuttles is also presented which illustrated the effect of reorganization energy and driving force evolving from the redox shuttle molecular design.

ACKNOWLEDGEMENTS

There are many people I would like to thank over my graduate life. First of all, I cannot express enough thanks to my advisor, Prof. Hamann, for his expert advice, continued support and encouragement thoughout all the projects. You have been a role model for your extraordinary dedication in scientific research and guidance of all lab members. My completion of the degree could not have been accomplished without the help of my lab mates. To Jesse, thank you for your mentoring in my early graduate life, you have always been an excellent example of knowledgeable and efficient graduate student. Many thanks also to Ben, Kelly, Masha, Reena, Suraj for their continued assistance during my early stage of my graduate life, it has been a great pleasure to have all of you as colleagues and as friends. I also appreciate all the joys and fun discussions brought by the DSSCs subgroup - Josh, Mandal, Yujue and Kuang. Thanks to Yuan, Omid, Hamed to their support and infusion of brilliant research ideas in Hamann Lab. Dan, Arianna and Fae are also appreciated for sparing more available time slots on the 'light' calendar. I sincerely wish all of you the best and continue exploring fantastic ideas in your research fields. This thesis would have been impossible without the support of funding agency, U.S. Department of Energy, and MSU Dissertation Completion Fellowship (Summer 2015). I also owe many thanks to my relatives in China for their help to my family. I could not achieve all this without the support of all my dear friends and wish you all good luck and successful. Lastly, I would like to thank my parents and my loved one for their continued support, I believe we always live together wherever I go and I promise the wait would not be long.

TABLE OF CONTENTS

LIST OF TABLES

LIST OF FIGURES

Chapter 1 Motivation and Introduction

1.1 Motivation for solar energy conversion research

Developing economically viable renewable energy technologies has been a pressing need to address the global challenges of clean energy, climate change and sustainable development. At the beginning of twenty-first century 2001, the worldwide energy consumption is around 13 TW/yr, this number is projected to double to around 30 TW/yr by 2050 and triple to around 44TW/yr by 2100.[1,2] The world fuel mix in 2014 indicated that fossil fuels, supplied 87% of the total world energy with oil of 33%, natural gas of 24% and coal of 30%.[3] Although there are many reserves of fossil fuels which are capable of sustain the growing energy consumption, they are facing rapid resource depletion. The oil reserved are projected to last 40 years, while the natural gas and coals are projected to last for 60 years and 200 years respectively. In addition, due to the uneven distribution of these fossil fuel resources, their access is potentially insecure and geo-political restricted. Another significant potential issue of consuming fossil fuels is the climate change as a result of the accumulated CO_2 emission from burning fossil fuels. A strong correlation has been shown between the CO_2 level in atmosphere and earth surface temperatures.[4] In 2010, energy emissions, mostly CO_2, account for the largest share of global Green House Gas (GHG) emissions according to the CO_2 emissions from fuel combustion report 2015.[3,5,6] To stabilize atmospheric CO_2 levels with continued economic growth will require development of innovative, cost-effective and carbon-neutral technologies that can fill the terawatts energy gap in the coming decades. Nuclear power is one approach, the terrestrial U resource are sufficient to produce ~100TW/yr, however, it demands at least one 1GW capacity new power plant/day to be built for 27 years in order to supply 10 TW to address the energy consumption challenge in 2050. Although fusion is promising for providing significant commercial energy late in 21st century, it is too far to contribute

to cost-effective energy production. The second approach is carbon capture and storage by dissolving CO_2 in the underground aquifers which requires less than 1% leak at a globally averaged rate to compromise the initially mitigated CO_2 amount. However, the method is facing several technical issues including geographical consideration for implementation, cost-production rate et al. The third approach is renewable to use renewable energy.[1] As reported, renewable energy is responsible for ~13% of global energy consumption in 2013 which includes wind, hydro, biomass and solar energy. Amongst the renewable energy resources, solar energy is by far the most promising energy resource to meet the growing energy demand due to its huge energy capacity.[5,7] Around 1.2×10^5 TW/yr (3500 times the energy that humankind would consume in 2050 according to the *ETP 2014* 6-degree scenario) solar energy is irradiated on earth's surface with around 36,000 TW received on land, while no other renewable energy resources (wind, 2-4 TW/yr; biomass, 5-7 TW/yr; tide and ocean currents, 2TW/yr, hydroelectric, 4.6 TW/yr; geothermal, 9.6 TW/yr) are capable of filling the energy gap coming in 2050 as projected. Two crucial steps of solar energy utilization are solar energy capture/conversion and storage. In terms of solar energy storage, there are three approaches, the first is storing solar electricity in batteries, the second is to store the energy in chemical bonds to produce solar fuels in an artificial photosynthesis process, the third is the solar thermal technology. Solar capture and conversion is viable by various photovoltaics (PV) techniques. A practical terrestrial global solar energy potential value is estimated to be about 600TW, provided that 10% efficient solar farms are widely installed, about 60TW solar energy can be supplied to meet even the doubles of estimated 2050 energy demand. Solar energy is widely available throughout the world and can contribute to reduced dependence on energy imports.[8,9] Solar PV entails no GHG emissions during operation and consumes no or little water which is necessary for cooling thermal power plants. All the above benefits of solar energy are indicating

the only answer to solve the energy problem is solar energy, also because no single energy resources are able to provide scalable energy amount to meet the growing energy demand.

However, PV has had a share of only more than 1% of the global electricity supply, which is already the highest number achieved so far in 2014. [10] The value is yet far less than comparable to the share of 81% by fossil fuels. What is standing in front of the widely adaptation of solar energy is primarily the high cost. Crystalline silicon (c-Si) currently dominates the PV market with around 90% share, 10-20% efficient silicon based PV produce electricity at a cost of approximately 0.25 - 0.65 $/KWhr, several time higher than <20 ¢/KWhr by fossil fuel electricity production.[10] The silicon based PV market is highly dependent on the price of the silicon material which requires high purity standards ~99.9999%. Emerging PV techniques such as amorphous silicon, CIGS and CdTe thin film based technologies, so-called second generation solar cells, permits a price reduction for high tunability and achievable power conversion efficiency. However, toxicity and low material abundance are major concerns for thin film PV's wide application. They are only representing about 10% share of the PV market in 2014, down from 16% in 2009.[8,10,11] The third generation PVs designs which is aimed at overcoming the Shockley-Queisser limit of previous generations of single junction based technologies have potential to introduce a scalable PV production by means of tandem cells, multiexciton generation et al. Dye sensitized solar cells (DSSCs) is one of the highly interesting technology for potential third generation PVs, because it offers several advantages such as potential in lowering production cost, multiple design options, high material abundance et al.

In conventional PV technologies, such as silicon based PVs, photo excitation of silicon generates electron-hole pairs within the crystal lattice, followed by carrier separation and collection. The light absorption is confined to the silicon bandgap, while the bandgap can be tuned

using thin film PV techniques. However, all the carrier transport and separation processes are taken place within the only material, silicon. Unlike conventional PV operational principles, these processes are separated in dye sensitized solar cells.[12] In DSSCs, visible light absorption is achieved by the sensitizer monolayer adsorbed on the wide band gap semiconductor framework such as TiO_2 with ~3 eV wide band gap. Through careful molecular engineer, sensitizer with various absorption band gaps can be utilized for harness a wide range of the solar spectrum, thus increased the design options. Additionally, upon photoexcitation of the sensitizer, electrons are quickly injected into the semiconductor conduction band. This demonstrate a great advantage of DSSCs because theoretically electron and hole pairs are well separated into two materials, avoiding electrons recombining with holes during transport in the semiconductor which is the case for conventional PVs. Application of wide band gap semiconductor materials for electron transport allows for reducing production cost, typical example is anatase TiO_2. Hole transport through the electrolyte, and electron transfer at the counter electrode to the redox shuttles in the electrolyte is necessarily very fast. The separated electron transfer kinetics allows for determination and investigation of the efficiency limiting steps in DSSCs. Further, the favorable electron transfer kinetics allows for DSSCs application in low light intensities, and expands indoor PV applications.

1.2 Historical development of DSSCs

Date back to 1839, French scientist Edmond Becquerel observed measurable current passing between two platinum electrodes when electrodes are immersed in metal halide salt containing electrolyte under illumination, which founded the field of photoelectrochemistry. Several decades later in 1883, Vogel discovered that the photosensitivity can be extended to longer wavelengths by sensitizing the silver halide emulsions with a dye. Inspired by the concept, Moser reported the first photosensitization effects on silver halide grains in 1887. Not until 1938, Gurney and Mott

theoretically analyzed the dye sensitization effect of AgBr grain with erythrosine and reported that electrons can be transferred from dye molecule into AgBr crystal after photoexcitation of dye molecule from ground state to an excited state which lies above the conduction band of AgBr. However, the mechanism of sensitization is achieved whether by electron transfer or energy transfer was under debate for the next three decades. In 1968, the report by Gerischer and Tributsch[13] in which they examined the sensitization effects at different semiconductor surface, typical n-type ZnO and p-type hydrocarbon perylene using electrochemical methods to measure the photocurrent gave an end to the long term debate. Because electrical conductivity methods used in earlier studies on probing spectral sensitization effects cannot extract the charge carrier away the semiconductor surface layer. Gerischer's report in 1968 also demonstrated the first detailed electrochemical and photoelectrochemical studies of the semiconductor-electrolyte interface.

Earlier attempts [13,14] of dye-sensitized photoelectrochemical cells were performed on smooth semiconductor surfaces, however, the light harvest efficiency is limited by utilizing the monolayer on flat electrode surface. In order to enhance the light absorption, the light absorption path has to be improved. Following attempts on increasing the surface area to enhancing light absorption has been carried, such as in 1977 Matsumura and in 1981 Alonso[15,16] . The overall efficiencies of the early examples were relatively below 1% due to still insufficient light capture and dye instability. In 1985, Desilvestro and Moser[17] presented results on efficient sensitization of high surface colloidal anatase particles and polycrystalline electrodes, followed by the explosive increase in efficiency for DSSCs in 1991 Nature paper by O'Regan and Grätzel[18] using mesoporous semiconductor electrode.

Besides the advancement of using high surface area semiconductor material brought by O'Regan and Grätzel's [18] Nature report in 1991. Another stimulus in the DSSCs sensitizer research area was inspired by the seminal paper. A diverse combination of DSSCs components made its way forward for future advancement. The history of anchoring sensitizers to semiconductors can be dated back to 1976, Osa and Fujihira[19] developed a photocell using rhodamine B as a sensitizer covalently bound by silyl ether and amide bonds to the electrode surface (SnO_2 or TiO_2) which is in contact with electrolyte solution containing reducing agent as supersensitser.[13] They observed as large photocurrent and presented a solution to cope with the energy loss by photoexcited dye relaxation in earlier reported free dye solution/semiconductor systems. As mentioned above, dyes used in earlier examples of dye sensitization system were unstable. Starting from 1975, the first example of stable transition metal complexes based sensitizers, Ruthenium(II) tris-bipyridyl complexes ($[Ru(bpy)_3]^{3+/2+}$) came to stage, introduced by Gleria and Memming. They observed electron transfer processes from $[Ru(bpy)_3]^{3+/2+}$ excited state to the conduction band of SnO_2 as anodic photocurrent and quantitatively matched with results obtained by pure $[Ru(bpy)_3]^{3+/2+}$ photochemical studies. The utilization of $[Ru(bpy)_3]^{3+/2+}$ in corporation with high surface area semiconductor electrodes was first reported in the 1985 paper by Desilvestro and Moser[17] which was quickly followed by 1988 Vlachopoulos and Grätzel paper[20] using $[Ru(dcbpy)_3]^{3+/2+}$ as sensitizer. However, the overall energy efficiency is partially limited by the wide HOMO-LUMO gap of $[Ru(dcbpy)_3]^{3+/2+}$, which harvest only <460nm wavelength light. In the goal of harvesting more red light from the solar spectrum to improve photocurrent and voltage, a trinuclear complex, $[Ru(bpy)_2(CN)_2]_2Ru(bpy(COO)_2)_2^{2-}$, with narrower HOMO-LUMO band gap which absorbs to 650nm were developed by Amadelli and Scandola in 1990.[21] Soon afterwards, Nazeeruddin and Grätzel extended the series of trinuclear based sensitizer. [22] In the famous1991 Nature paper by

O'Regan and Grätzel, [18] they used the trinuclear sensitizer, $[Ru(bpy)_2(CN)_2]_2Ru(bpy(COO)_2)_2^{2-}$, on 10 μm thick transparent TiO_2 nanoparticle film, yielded over 7% energy conversion efficiency in simulated AM 1.5 illumination and 12% in diffuse day light and achieved >2 month stability under visible (>400nm) light. After the concept of diverse combination of DSSCs components brought by the paper, thousands of sensitizers have been developed. After 1991, the classical dyes N3 based series sensitizers which dominated the DSSCs efficiency record for one decade was developed. As reported in 1993 by Nazeeruddin and Grätzel, N3 dye – $Ru(dcbpy)_2(NCS)_2$, absorbs far to 800nm, achieving a 10% energy conversion efficiency for DSSCs. For the first time, DSSCs attains a conversion efficiency commensurate with conventional silicon-based PV cells at that time.[23] Analogues of N3, black dye N749 was soon developed later, extending the solar spectrum absorption between 650nm and 950nm, attaining a promising maximum photocurrent of 21 mA cm^{-2}.[24] The heteroleptic ruthenium complexes have bring the DSSCs efficiency to a new stage. Although there is a plethora of sensitizers developed for DSSCs after the 1991 seminal paper, the advancement of redox shuttles for DSSCs is not as prospect as that of sensitizers. The DSSCs record reached a plateau at 10%-11%, the main components of most efficient DSSCs systems have not been changed much utilizing iodide/triiodide redox shuttles with 4-tert butylpyridine additives.

New thoughts on diversify the redox shuttle systems to accelerate the DSSCs system progress was started by the introduction of outer-sphere redox shuttle to substitute conventional iodide/triiodide system which has been leading record efficiency over decades. In 2001, Gregg and Field[25,26] reported the first outer-sphere alternative redox shuttles, ferrocene/ferrocenium, however, the redox shuttles suffers from fast recombination and instability. Other outersphere redox shuttles such as Ni(III)/(IV) bis(dicarbollide)[27] and cobalt(III/II) polypyridyl complex have been investigated afterwards but received little attention. A break through is made by Feldt and

Hagfeldt [28] in 2010, utilizing cobalt trispyridyl redox shuttles ($[Co(bpy)_3]^{3+/2+}$) with triphenylamine-based organic sensitizer delivered ~7% energy conversion efficiencies. One year later, Yella and Gratzel reported a new record efficiency of 12.3% using cobalt trispyridyl redox shuttles in conjunction with co-sensitization of donor-π-bridge-acceptor zinc porphyrin and organic D- π-A dye (Y123).[29] The 2011 Science paper take the DSSCs development to a new level where research are focused on more complicated sensitizer molecular engineering (both organic and inorganic sensitizers) in corporation with cobalt based outer-sphere redox shuttles. By far, the efficiency record is still kept ~13% using $[Co(bpy)_3]^{3+/2+}$ and zinc-porphyrin based dye.[30]

1.3 DSSCs operation and key electron transfer processes

There are three main components of a DSSC, 1) photoanode composed of dye sensitized wide band gap semiconductor nanoparticle films (typically TiO_2) deposited on transparent conductive oxide coated substrate (abbreviated as TCO, typical TCO used are FTO or ITO, fluorine or indium doped tin oxide); 2) electrolyte composed of redox shuttles (donor/acceptor), supporting electrolyte and other additives dissolved in choices of solvent ;3) counter electrode with catalyst that are capable of reducing the acceptor species coated on TCO substrates. A schematic figure of a liquid electrolyte DSSC is shown in below in Figure 1.1.

The key kinetic processes in occurring during DSSCs operation are illustrated in Figure 1.2. Under illumination, light is absorbed by the dye molecule anchored to the surface of a TiO2 nanoparticle (k_1). Then an electron from the excited dye is injected into the conduction band of TiO_2, followed by electron diffusion through the mesoporous nanoparticle film and reaching the back contact at FTO substrate where electrons are collected and travel through the external circuit for photocurrent production. The reduced (donor) form of redox shuttles in the electrolyte will further regeneration the oxidized dye(k_{reg}). Then the oxidized form of redox shuttles will diffuse

(D_0) through the electrolyte to the counter electrode and be reduced back to its reduced form, thus complete the circuit. There are several processes are competing with the above favorable process, inhibiting efficient DSSCs operation. After photogeneration of dye excited state, the dye can undergo either radiative or nonradiative decay prior to injection (k_{-1}), the injected electrons in the TiO_2 conduction band can recombine with the oxidized dye (k_{rec1}) or redox shuttle in the electrolyte before being collected at back contact of photoanode (k_{rec2}).

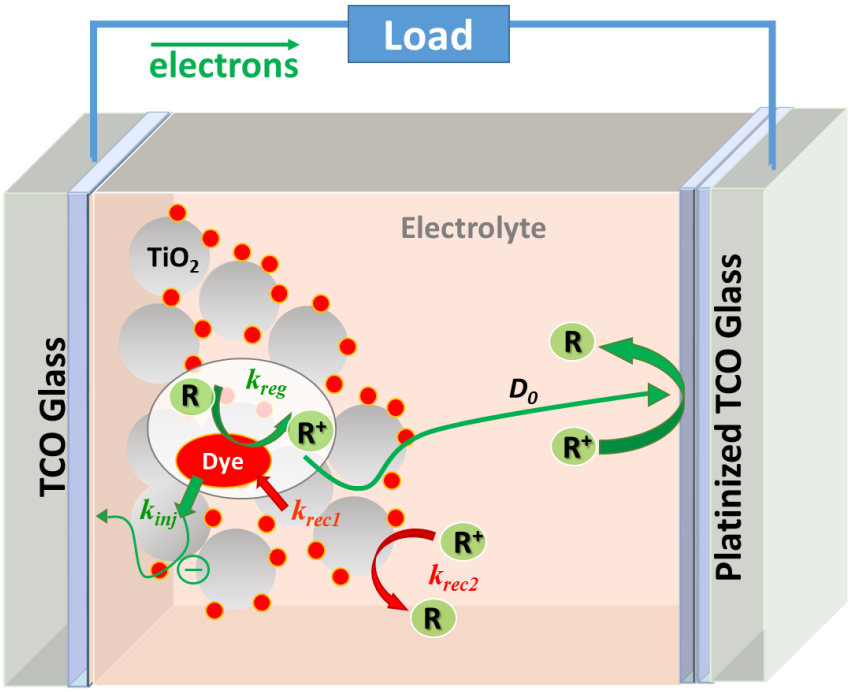

Figure 1.1 Schematic of a liquid electrolyte based dye-sensitized solar cell.

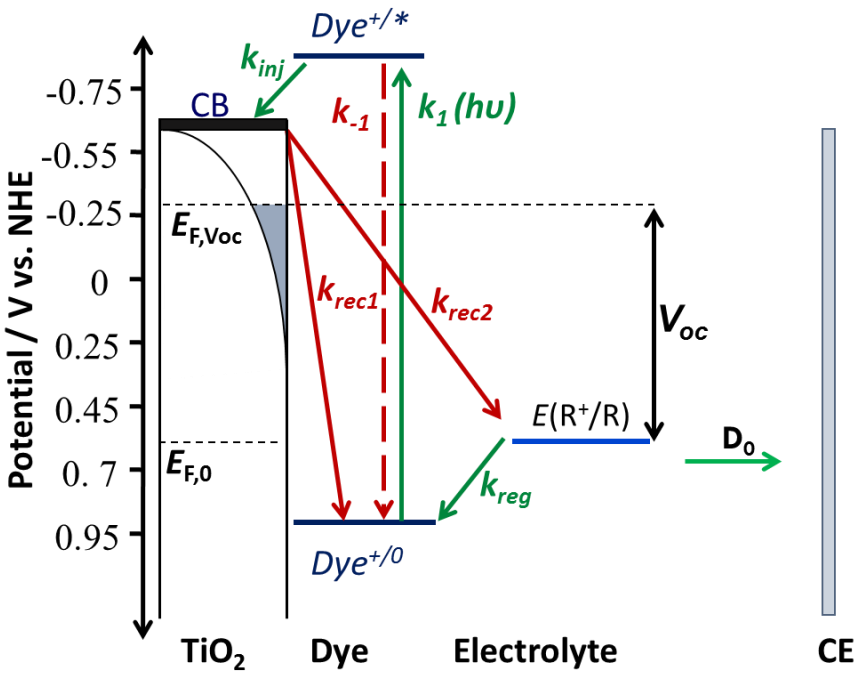

Figure 1.2 Energy diagram displaying the major kinetic processes in the operation of DSSCs.

1.4 Review on research of DSSCs electrolytes

As is illustrated in 1.3 above, there are several electron transfer processes occurring in DSSCs operation, while the favorable processes are producing photocurrent and photovoltage, thus breaking the equilibrium in the cell, the competing electron transfer processes are pull the cell back to equilibrium which hampered the cell energy conversion efficiency. In the case of efficient injection, the two electron recombination processes (k_{rec1}, to oxidized dye; k_{rec2}, to redox shuttles) are the major energy loss pathways. An ideal redox shuttle can be capable of regenerate the dye efficiently while possess slow recombination kinetics. This criterion makes it difficult to expand the choices of effective choice.

1.4.1 Iodide/triiodide electrolyte (I^-/I_3^-)

During the 1990s to 2010, The iodide/triiodide (I^-/I_3^-) electrolyte have been the favorable choice of DSSCs electrolyte, because it has a suitable redox potential and provide efficient regeneration for classical dyes such as N3 and N719,[31] and has a slow recombination kinetics due to its complicated multi-electron transfer feature.[32,33] Additionally, the conductivity and the solubility of iodide/triiodide is very good in many solvents, presenting a large diffusion coefficient due to its small size which make it favorable penetrating though the semiconductor nanoparticle film.[34] I^-/I_3^- also has a relative low light absorbance reducing competitive light absorption with the dye.[35] Long term stability is also an important feature of I^-/I_3^- for potential industrial application.

Though the I^-/I_3^- redox shuttle based electrolyte presented remarkable performance in DSSCs, there are several disadvantages limiting its further development. Firstly, iodine is highly corrosive to many sealing materials, especially metals, inducing problems assembling and sealing for large-area DSSC module production and long term stability.[36] Secondly, iodine has a relatively high vapor pressure which make it challenging for device encapsulation and may result in potential electrolyte leakage. Thirdly, the redox potential of I^-/I_3^- is a limiting factor for further improvement of device open circuit voltage (V_{oc}). A redox potential of E (I^-/I_3^-) = 0.32 *V* vs NHE is regenerating efficiently with most dyes of E (dye/dye$^+$) = 1.1 V vs NHE with a regeneration driving force loss ~ 0.8V which in turn reflected as limited V_{oc}.[32,37,38] Due to the complicated electron transfer nature of I^-/I_3^-, its dye regeneration mechanism is complex. Various mechanisms have been proposed for dye regeneration with I^-/I_3^- to understand the reaction order and limiting steps. [39,40,41,42] One prevailing scheme of dye regeneration with I^-/I_3^- involves [dye$^+\cdots$I$^-$] intermediate forming at first step, followed by $I_2^{\bullet-}$ radical formation in the second step, the last step is disproportionation of $I_2^{\bullet-}$. [31] This dye dependent regeneration mechanism is beneficial for dyes with binding sites for I- to

achieve efficient regeneration, for example, N3 and its analogues. A recent paper by Martiniani and O'Regan showed that the regeneration order is 2nd order in I^- for two organic dyes.[40] Identify the limiting steps and reaction orders is crucial to find proper materials to catalyze regeneration and facilitate incorporation of NIR absorbing dyes for DSSCs. However, this is still unsettled for I^-/I_3^- redox shuttles. The dye dependent regeneration mechanism refrained the research field's attention from many promising alternative dyes,[43,44] simply based on the fact of inefficient regeneration by I^-/I_3^-. The strong dependence on I^-/I_3 redox shuttles of DSSCs field has limited the systematic studies and optimization of cell efficiency.[35]

Alternative redox shuttles with slightly more positive redox potentials such as pseudohalogen redox shuttles $(SeCN)_2/SeCN^-$ (E_{redox} = 0.52 V vs NHE) and $(SCN)_2/SCN^-$ (E_{redox} = 0.76 V vs NHE)[45,46] have been reported, attaining 7.5% conversion efficiency in combination with N3 dye.[47] However, the pseudohalogen redox shuttles have poor stability which inhibit further application. Organic redox disulfide/thiolate(T^-/T_2^-) (T^-, 1-methyl-1-H-tetrazole-5-thiolate; T_2^- is the dimer) redox shuttles were reported to achieve a maximum 7.9% efficiency, but the redox potential of T^-/T_2^- is close to I^-/I_3^- thus bearing the same problem as I^-/I_3^- for limited tunability and large regeneration energy lost.[48,49]

1.4.2 Outer-sphere redox shuttles in DSSCs

First outersphere redox shuttle ferrocene/ferrocenium (Fc^+/Fc, E_{redox} = 0.62 V vs NHE) was introduced to DSSCs for its favorable fast electron transfer kinetic which is potentially attractive for fast regeneration, however, its performance is limited by rapid interfacial recombination. Proper surface treatment of semiconductor would passivate the interfaces and decrease recombination, thus help improve DSSCs performance employing Fc^+/Fc. However, Fc^+ is unstable in contact to oxygen and pyridines employed in typical electrolytes. The highest

efficiency for DSSCs with Fc^+/Fc was reported to be 7.5%, requiring all device fabrication and electrolyte to be done in glovebox. The difficulty of device preparation and sealing brought by the fact that Fc^+ is not stable exclude Fc^+/Fc from being a practical alternative redox shuttles. [25,50] Outersphere redox shuttles such as Ni(III)/(IV) bis(dicarbollide)[27] and Cu(I)/Cu(II) based redox shuttles[51] have been investigated, however, was not considered as a practical alternative redox shuttles owing to the unfavorable complicated synthesis and slow kinetics on counter electrodes respectively.[52] Kim and Jeong used $[Ru(bpy)_3]^{2+}$ as a single-component redox shuttle in junction with an organic dye JK2 and gave 4.67% efficiency at 0.1 Sun, but the performance is limited by solubility and diffusion partly from the effect of omitting the unstable oxidized form.[53] Jiang and Zhou recently [54] used other Ru(III)/Ru(II) based redox shuttles with structurally similarly sensitizers and achieved an high open-circuit voltage of 0.9 V and 2.5mV cm^{-2} photocurrent with nearly zero driving force, but the performance is still affected by the low solubility in commonly used electrolyte solvent.

Cobalt trisbipyridyl based redox shuttles which was used in the current champion DSSCs, was a promising outersphere redox shuttle for many advantages such as good stability, highly tunable structure and potential, and less competitive light absorption. Cobalt based redox shuttles was developed since 2001, first example Cobalt 2,6-bis(1'-butylbenzimidazol-2'-yl)pyridine ($[Co(dbbip)_2]^{3+/2+}$) [55] reported by Nusbaumer et al. was used in pair with a ruthenium dye (Z316) giving 2.2% efficiency under 1sun, in which the overall cell performance was discussed to be limited by fast recombination of electrons from conduction band and mass transport. Sapp and Elliott ,[42,34] screened a series of cobalt trispyridyl based redox shuttles and investigated the mass transport properties of the these redox shuttles, their best result is attained by Cobalt tris(4,4'-tert-butyl-2,2'-bipyridine) ($[Co(t\text{-}Bu_2bpy)_3]^{3+/2+}$) which exhibited efficiencies 80% as high as the I^-/I_3^-

control cells. In addition, Nelson and Elliott also showed that the diffusion of $[Co(t\text{-}Bu_2bpy)_3]^{3+}$ is one order of magnitude slower than the diffusion of I_3^- in bulk solutions, and suggested several strategies overcoming the drawbacks such as changing electrolyte solvent and/or counterion, TiO_2 pore sizes et al. Klahr and Hamann [56]investigated the cell performance of a series cobalt trispyridyl based redox shuttles, and found that they can regenerate N3 dye efficiently though overall performance is limited by recombination. They underlined the importance to address recombination problem of cobalt redox shuttles for achieving high efficiencies. Feldt and Hagfeldt investigated cell performances of several Co(II)/(III) ($[Co(bpy)_3]^{3+/2+}$ and $[Co(phen)_2]^{3+/2+}$) based electrolyte and organic dyes (D35, D29), their best result presents 6.7% overall conversion efficiency.[28] All these above studies showed that cobalt based redox shuttles could achieve high energy conversion efficiency through careful structure design of redox shuttles, choices of sensitizers and semiconductor modification et al. In 2011, Yella and Grätzel[29] reported a significant improvement of DSSCs efficiency record to 12.3% using $[Co(bpy)_3]^{3+/2+}$ and Zinc-porphyrin based sensitizer, driving the field of redox shuttles in to new directions. By far, the DSSCs efficiency record 13% is still kept by cells using $[Co(bpy)_3]^{3+/2+}$ and D-π-bridge-A structured zinc porphyrin dye SM315 in 2014.[30] Driven by the exciting progress of using cobalt trisbipyridyl based redox shuttles in DSSCs, other structurally similar redox shuttles with tunable structure design was also reported. Yum and Grätzel[57] reported redox shuttles $[Co(bpy\text{-}pz)_2]^{3+/2+}$ (bpy-pz = 6-(1H-pyrazol-1-yl)-2,2-bipyridine) in combination with Y123 dye, yielding over 10% power conversion efficiency and over 1V open circuit voltage. Kashif and Bach[58] also reported a series of alternative redox shuttles $[Co(PY5Me_2)(B)]^{3+/2+}$($PY5Me_2$ = 2,6-bis(1,1-bis(2-pyridyl)ethyl)pyridine, B = 4-tert-butylpyridine (tBP) or N-methylbenzimidazole (NMBI)), they attained ~9% power conversion efficiency with these redox shuttles in combination with organic

dye MK2. These progresses indicated that cobalt based redox shuttles can be a legitimate alternative to conventional I^-/I_3^- redox shuttles, realizing the promise of cost-effective DSSCs.

1.5 Motivation of use of low spin cobalt based redox shuttles in DSSCs

Despite of the advantages of cobalt-based redox shuttles, it is still not optimal. For example, Klahr and Hamann [42] found that $[Co(Me_2bpy)_3]^{3+/2+}$ and $[Co(t\text{-}Bu_2bpy)_3]^{3+/2+}$ attained higher incident photo to current conversion efficiency (IPCE) than I^-/I_3^- owing to better dye regeneration. $[Co(bpy)_3]^{3+/2+}$ can regenerate ruthenium-based dyes N719, Z907[59] and zinc porphyrin based dye[29]effectively given by high IPCE maximum values.$[Co(phen)_2]^{3+/2+}$ is able to regenerate organic dye C218 displaying a high efficiency of 8.3%. Feldt and Hagfeldt [28,60] screened a series of cobalt bipyridine and phenanthroline complexes redox shuttles and found that a minimal driving force of 390mV for dye regeneration to be more efficient than 80% is needed. All above discoveries revealed that although cobalt redox shuttles are able to regenerate certain dyes efficiently, a large regeneration driving force is still required. The large regeneration driving force can be attribute to the important feature that these cobalt complexes discussed above undergo a spin change from cobalt(II) (high spin, $t_{2g}^5e_g^2$) to cobalt (III) (low spin, $t_{2g}^6e_g^0$), which produces a large inner-sphere reorganization energy (~1 eV) and slow electron self-exchange kinetics (e.g. ~10 M^{-1} s^{-1} for $[Co(bpy)_3]^{3+/2+}$. [61–63] Additionally, the large reorganization energy also produces slow recombination kinetic at TiO_2 electrodes which makes cobalt redox shuttles stand out to substitute I^-/I_3^- redox shuttles.[64] However, the recombination rate of cobalt based redox shuttles is not low enough to obtain quantitative charge collection, unless strategies are taken to passivate the surface and introduce cell designs to overcome mass transfer limitations and counter electrode losses. For example, Hamann group reported treatment of TiO_2 by Atomic Layer Deposition (ALD) of thin insulating layer coating,[42,65] which effectively inhibited the back electron transfer from

TiO_2 to electrolyte, but the dye injection is also hindered by the insulating layer. [66] Other ways to reduce the demands of necessary diffusion length for good charge collection includes utilization sensitizer with steric blocking groups to minimize recombination, or using sensitizers with high molar extinction coefficient.[28,67] Application of porous conductive polymer based counter electrodes can effectively reduce the charge transfer resistance at counter electrode and relieve the diffusion limitation of photocurrent caused by slow diffusion and low solubility of Co(III) from.[68] Although there are exciting advancement of cobalt redox shuttles in recent years, further improvements is still in great need in addition to the strategies discussed above. One problem is how to further reduce the large regeneration driving force which results the largest energy loss in DSSCs. Previous studies showed that other outersphere redox shuttles, e.g. ferrocene, was an excellent dye regenerator but it was not stable and suffers from recombination due to its fast electron transfer kinetics. [25,50,69] Therefore, a motif to address the energy loss problem is introducing a redox shuttles capable of regenerate dye with minimal driving force, e.g. ferocene/ferrocenium, but that is stable, e.g. $[Co(bpy)_3]^{3+/2+}$. While an important feature of outersphere redox shuttles is the feasibility of simplified measurements, predictable electron transfer properties which enables generalization of systematic design of favorable redox shuttles for DSSCs. To proof the new motif of introducing low spin cobalt based redox shuttles (smaller barrier from low spin Co(II) ($t_{2g}^6e_g^1$) to low spin Co(III) ($t_{2g}^6e_g^0$) electron transfer), it would be beneficial if systematic research can be done on understanding the regeneration and recombination kinetics employing cobalt based outer-sphere redox shuttles.

This thesis thus first discusses use of a low spin cobalt (II) complex redox shuttles, $[Co(ttcn)_2]^{3+/2+}$ (ttcn = *1,4,7*-trithiacyclononane) in DSSCs, initial results allowed determination of overall performance limitations 1) electron recombination from TiO_2 is fast 2) regeneration is not

rate limiting compared to high spin cobalt (II) redox shuttles, $[Co(bpy)_3]^{3+/2+}$. The results showed great promises of achieving high efficiency with low spin cobalt based redox shuttles in DSSCs. Further detailed consideration of regeneration and recombination employing cobalt redox shuttles are thus discussed in Chapter 3. By means of illumination direction dependent IPCE results fitting and careful optical measurements, diffusion length, L_n, and charge collection efficiency, light harvest efficiency, dye regeneration and injection efficiency can be easily analyzed separated. Application of Marcus theory allowed for quantitative analysis of regeneration and recombination resulted from different self-exchange rate constant between high spin and low spin cobalt redox shuttles. Quantitative regeneration for low spin $[Co(ttcn)_2]^{3+/2+}$ was demonstrated, however, short diffusion length is still a significant limitation for $[Co(ttcn)_2]^{3+/2+}$. Therefore, in Chapter 4, to overcome the diffusion length limitation result from fast low spin to low spin electron transfer kinetics, but also to expand the low spin cobalt redox shuttles with more tunable structure. A redox shuttle with a strong pentakispyridyl chelating ligand and highly tunable sixth coordination site, $[Co(PY5Me_2)(CN)]^{3+/2+}$ ($PY5Me_2$ = 2,6- bis(1,1-bis(2-pyridyl)ethyl)pyridine) was investigated. By introduction of an anionic strong field ligand, CN^-, the complex is determined to be a low spin cobalt(II) with a redox potential ~400 mV negative of $[Co(ttcn)_2]^{3+/2+}$. Detailed synthesis and characterization of the redox shuttles are discussed, initial performance in DSSCs is indicated that the new redox shuttle is a better regenerator using $[Co(bpy)_3]^{3+/2+}$ as a control. Owing to a quite negative redox potential of $[Co(PY5Me_2)(CN)]^{3+/2+}$, which is 0.23 V vs NHE, a large energy loss ~0.7 eV from regeneration still exists (taken that most dye ground state level lies around 1 V vs NHE). It would be beneficial to pair the new redox shuttles with sensitizer with more negative ground state level. In Chapter 5, we thus investigated the effect of regeneration driving force using cobalt redox shuttles with a series highly tunable ruthenium cyclometalated sensitizers. The results

demonstrated the successful structure design of sensitizers could ultimate lead to better energy match with redox shuttles to improve overall performance. The discussion shines light on utilization of structurally similar osmium based cyclometalated sensitizers to pair with $[Co(PY5Me_2)(CN)]^{3+/2+}$, because of the tunability of cyclometalated structure and attractive features of osmium dyes such as a more negative ground state level for less energy loss and broad near infrared absorption. In Chapter 6, some other alternative low spin cobalt based redox shuttles, such as Co(III)/Co(IV) redox, are outline and discussed. In Chapter 7, future directions of current generation of redox shuttles are discussed.

REFERENCES

REFERENCES

(1) Lewis, N. S.; Nocera, D. G. *Proc. Natl. Acad. Sci.* **2007**, *103*, 15729–15735.

(2) Lewis, N. S. *MRS Bull.* **2007**, *32*, 808–820.

(3) IEA. *Key Trends in CO2 emissions*. 2015.

(4) Hoffert, M. I.; Caldeira, K.; Jain, A. K.; Haites, E. F.; Harvey, L. D. D.; Potter, S. D.; Schlesinger, M. E.; Schneider, S. H.; Watts, R. G.; Wigley, T. M. L.; Wuebbles, D. J. *Nature* **1998**, *395* (6705), 881–884.

(5) IEA. *Key World Energy Statistics*. 2015.

(6) IPCC. *Special Report Emissions Scenarios*. 2000.

(7) BP. *Statistical Review of World Energy*. 2015.

(8) IEA. *Technology Roadmap-Photovoltaic Energy*. 2014.

(9) Barkhouse, D. A. R.; Gunawan, O.; Gokmen, T.; Todorov, T. K.; Mitzi, D. B. *Prog. Photovoltaics Res. Appl.* **2015**, *23*, 805–812.

(10) IEA-PVPS. *Trends in Photovoltaic Applications*. 2015.

(11) Roeb, M.; Neises, M.; Monnerie, N.; Sattler, C.; Pitz-Paal, R. *Energy Environ. Sci.* **2011**, *4*, 2503.

(12) Grätzel, M.; O'Regan, B. C. *Nature* **1991**, *353*, 737–739.

(13) Gerischer, H.; Michel-Beyerle, M. E.; Rebentrost, F.; Tributsch, H. *Electrochim. Acta* **1968**, *13*, 1509–1515.

(14) Gerischer, H.; Tributsch, H. *Ber. Bunsen-Ges. Phys. Chem.* **1968**, *72*, 437–445.

(15) Alonso V., N.; Beley, M.; Chartier, P.; Ern, V. *Rev. Phys. Appl.* **1981**, *16*, 5–10.

(16) Matsumura, M.; Nomura, Y.; Tsubomura, H. *Bull. Chem. Soc. Jpn.* **1977**, *50*, 2533–2537.

(17) Desilvestro, J.; Graetzel, M.; Kavan, L.; Moser, J.; Augustynski, J. *J. Am. Chem. Soc.* **1985**, *107*, 2988–2990.

(18) Grätzel, M.; O'Regan, B. C.; O'Regan, B.; Grätzel, M. *Nature* **1991**, *353*, 737–740.

(19) Osa, T.; Fujihira, M. *Nature* **1976**, *264*, 349–350.

(20) Vlachopoulos, N.; Liska, P.; Augustynski, J.; Grätzel, M. *J. Am. Chem. Soc.* **1988**, *110*, 1216–1220.

(21) Amadelli, R.; Argazzi, R.; Bignozzi, C. a; Scandola, F. *J. Am. Chem. Soc.* **1990**, *112*, 7099–7103.

(22) Nazeeruddin, M. K.; Liska, P.; Moser, J.; Vlachopoulos, N.; Gratzel, M. *Helv. Chim. Acta* **1990**, *73*, 1788–1803.

(23) Nazeeruddin, M. K.; Kay, A.; Miiller, E.; Liska, P.; Vlachopoulos, N.; Gratzel, M.; Lausanne, C.-; April, R. *J. Am. Chem. Soc.* **1993**, *115*, 6382–6390.

(24) Nazeeruddin, M. K.; Péchy, P.; Renouard, T.; Zakeeruddin, S. M.; Humphry-Baker, R.; Cointe, P.; Liska, P.; Cevey, L.; Costa, E.; Shklover, V.; Spiccia, L.; Deacon, G. B.; Bignozzi, C. a.; Grätzel, M. *J. Am. Chem. Soc.* **2001**, *123*, 1613–1624.

(25) Gregg, B. a.; Pichot, F.; Ferrere, S.; Fields, C. L. *J. Phys. Chem. B* **2001**, *105*, 1422–1429.

(26) Gregg, B. a. *Coord. Chem. Rev.* **2004**, *248*, 1215–1224.

(27) Li, T. C.; Spokoyny, A. M.; She, C.; Farha, O. K.; Mirkin, C. a; Marks, T. J.; Hupp, J. T. *J. Am. Chem. Soc.* **2010**, *132*, 4580–4582.

(28) Feldt, S. M.; Gibson, E. a; Gabrielsson, E.; Sun, L.; Boschloo, G.; Hagfeldt, A. *J. Am. Chem. Soc.* **2010**, *132*, 16714–16724.

(29) Yella, A.; Lee, H.-W.; Tsao, H. N.; Yi, C.; Chandiran, A. K.; Nazeeruddin, M. K.; Diau, E. W.-G.; Yeh, C.-Y.; Zakeeruddin, S. M.; Grätzel, M. *Science* **2011**, *334*, 629–634.

(30) Mathew, S.; Yella, A.; Gao, P.; Humphry-Baker, R.; Curchod, B. F. E.; Ashari-Astani, N.;

Tavernelli, I.; Rothlisberger, U.; Nazeeruddin, M. K.; Grätzel, M. *Nat. Chem.* **2014**, *6*, 242–247.

(31) Clifford, J. N.; Palomares, E.; Nazeeruddin, K.; Gra, M.; Durrant, J. R. *J. Phys. Chem. C* **2007**, *111*, 6561–6567.

(32) Boschloo, G.; Hagfeldt, A. *Acc. Chem. Res.* **2009**, *42*, 1819–1826.

(33) Rowley, J.; Meyer, G. J. *J. Phys. Chem. Lett.* **2009**, *113*, 18444–18447.

(34) Nelson, J. J.; Amick, T. J.; Elliott, C. M. *J. Phys. Chem. C* **2008**, *112*, 18255–18263.

(35) Hamann, T. W. *Dalt. Trans.* **2012**, *41*, 3111–3115.

(36) Olsen, E.; Hagen, G.; Eric Lindquist, S. *Sol. Energy Mater. Sol. Cells* **2000**, *63*, 267–273.

(37) Hagfeldt, A.; Boschloo, G.; Sun, L.; Kloo, L.; Pettersson, H. *Chem. Rev.* **2010**, *110*, 6595–6663.

(38) Datta, J.; Bhattacharya, A.; Kundu, K. K. *Bull. Chem. Soc. Jpn.***1988**, *61*, 1735–1742.

(39) Anderson, A. Y.; Barnes, P. R. F.; Durrant, J. R.; Regan, B. C. O. *J. Phys. Chem. C* **2011**, *115*, 2439–2447.

(40) Martiniani, S.; Anderson, A. Y.; Law, C.; O'Regan, B. C.; Barolo, C. *Chem. Comm.* **2012**, *48* (18), 2406.

(41) Barnes, P. R. F.; Anderson, A. Y.; Durrant, J. R.; O'Regan, B. C. *Phys. Chem. Chem. Phys.* **2011**, *13*, 5798–5816.

(42) Klahr, B. M.; Hamann, T. W. *J. Phys. Chem. C* **2009**, *113*, 14040–14045.

(43) Alebbi, M.; Bignozzi, C. a; Heimer, T. a; Hasselmann, G. M.; Meyer, G. J. *J. Phys. Chem. B* **1998**, *102*, 7577–7581.

(44) Kuciauskas, D.; Freund, M. S.; Gray, H. B.; Winkler, J. R.; Lewis, N. S. *J. Phys. Chem. B* **2001**, *105*, 392–403.

(45) Oskam, G.; Bergeron, B. V; Meyer, G. J.; Searson, P. C. *J. Phys. Chem. B* **2001**, *105*, 6867–

6873.

(46) Wang, P.; Zakeeruddin, S. M.; Moser, J.-E.; Humphry-Baker, R.; Grätzel, M. *J. Am. Chem. Soc.* **2004**, *126*, 7164–7165.

(47) Bai, Y.; Cao, Y.; Zhang, J.; Wang, M.; Li, R.; Wang, P.; Zakeeruddin, S. M.; Grätzel, M. *Nat. Mater.* **2008**, *7*, 626–630.

(48) Wang, M.; Chamberland, N.; Breau, L.; Moser, J.-E.; Humphry-Baker, R.; Marsan, B.; Zakeeruddin, S. M.; Grätzel, M. *Nat. Chem.* **2010**, *2*, 385–389.

(49) Burschka, J.; Brault, V.; Ahmad, S.; Breau, L.; Nazeeruddin, M. K.; Marsan, B.; Zakeeruddin, S. M.; Grätzel, M. *Energy Environ. Sci.* **2012**, *5*, 6089.

(50) Daeneke, T.; Kwon, T.; Holmes, A. B.; Duffy, N. W.; Bach, U.; Spiccia, L. *Nat. Chem.* **2011**, *3*, 211–215.

(51) Hattori, S.; Wada, Y.; Yanagida, S.; Fukuzumi, S. *J. Am. Chem. Soc.* **2005**, *127*, 9648–9654.

(52) Bai, Y.; Yu, Q.; Cai, N.; Wang, Y.; Zhang, M.; Wang, P. *Chem. Commun.* **2011**, *47*, 4376–4378.

(53) Kim, J. Y.; Yun, W. S.; Son, H.-J.; Lee, J.; Jeong, N. C. *Chem. Commun.* **2015**, *51* (36), 7745–7748.

(54) Jiang, D.; Darabedian, N.; Ghazarian, S.; Hao, Y.; Zhgamadze, M.; Majaryan, N.; Shen, R.; Zhou, F. *ChemPhysChem* **2015**, 10.1002/cphc.201500641.

(55) Moser, J.; Zakeeruddin, S. M.; Nazeeruddin, M. K.; Gra, M. *J. Phys. Chem. B* **2001**, *105*, 10461–10464.

(56) Sapp, S. a; Elliott, C. M.; Contado, C.; Caramori, S.; Bignozzi, C. a. *J. Am. Chem. Soc.* **2002**, *124*, 11215–11222.

(57) Yum, J.-H.; Baranoff, E.; Kessler, F.; Moehl, T.; Ahmad, S.; Bessho, T.; Marchioro, A.; Ghadiri, E.; Moser, J.-E.; Yi, C.; Nazeeruddin, M. K.; Grätzel, M. *Nat. Commun.* **2012**, *3*, 631.

(58) Kashif, M. K.; Axelson, J. C.; Du, N. W.; Forsyth, C. M.; Chang, C. J.; Long, R.; Spiccia, L.; Bach, U. *J. Am. Chem. Soc.* **2012**, *134*, 16646–16653.

(59) Liu, Y.; Jennings, J. R.; Huang, Y.; Wang, Q.; Zakeeruddin, S. M.; Gr, M. *J. Phys. Chem. C* **2011**, *115*, 18847–18855.

(60) Feldt, S. M.; Wang, G.; Boschloo, G.; Hagfeldt, A. *J. Phys. Chem. C* **2011**, *115*, 21500–21507.

(61) Weaver, M. J.; Yee, E. L. *Inorg. Chem.* **1980**, *19*, 1936–1945.

(62) Sutin, N. *Acc. Chem. Res.* **1982**, *15*, 275–282.

(63) Marcus, R. A. *J. Phy. Chem.* **1990**, *94*, 1050–1055.

(64) Nakade, S.; Makimoto, Y.; Kubo, W.; Kitamura, T.; Wada, Y. *J. Phys. Chem. B* **2005**, *109*, 3488–3493.

(65) Ondersma, J. W.; Hamann, T. W. *J. Phys. Chem. C* **2010**, *114*, 638–645.

(66) Palomares, E.; Clifford, J. N.; Haque, S. a; Lutz, T.; Durrant, J. R. *J. Am. Chem. Soc.* **2003**, *125*, 475–482.

(67) Xie, Y.; Hamann, T. W. *J. Phys. Chem. Lett.* **2013**, *4*, 328–332.

(68) Tsao, H. N.; Burschka, J.; Yi, C.; Kessler, F.; Nazeeruddin, M. K.; Grätzel, M. *Energy Environ. Sci.* **2011**, *4*, 4921.

(69) Hamann, T. W.; Farha, O. K.; Hupp, J. T. *J. Phys. Chem. C* **2008**, *112*, 19756–19764.

Chapter 2 Fast Low-Spin cobalt complex redox shuttles for DSSCs

2.1 Abstract

A low spin cobalt(II) complex redox couple – cobalt bis-trithiacyclononane, $[Co(ttcn)_2]^{3+/2+}$ – was investigated for use as a redox shuttle in dye-sensitized solar cells, DSSCs. This unique cobalt complex redox shuttle is stable, transparent, easy to synthesize from commercial ligands, and has attractive energetic and kinetic features for use in DSSCs. Initial results indicate that the overall performance is limited by recombination. Variation of sensitizer and deposition of an ultra thin coating of alumina on nanoparticle based TiO_2 DSSC photoanodes reduced recombination which resulted in significantly improved quantum yields. The photovoltaic behavior was compared to the current record efficiency cobalt tris-bipyridine, $[Co(bpy)_3]^{3+/2+}$, redox shuttle and produced similar results. Further use of a high extinction organic sensitizers with only ~200 mV driving force for regeneration were examined which produced efficiencies of over 2%; importantly regeneration is not rate limiting in this system thus demonstrating the promise of using such fast redox shuttles.

2.2 Introduction

In 1991, O'Regan and Grätzel published a seminal paper which demonstrated that dye-sensitized solar cells, DSSCs, are capable of producing high power conversion efficiencies. [1] The exciting possibility of achieving efficient solar energy conversion with inexpensive materials sparked intense research interest in DSSCs, however the efficiency did not improve substantially over the subsequent decades. The plateau in efficiency over this period can largely be attributed to reliance on the I_3^-/I^- redox shuttle.[2–5] While there are several thousands of papers reporting significant advances in the sensitizer and photoanode, only a handful of alternative redox shuttles that show promise in replacing I_3^-/I^- have been reported. [6–8] The reason so few redox couples have

proven successful is largely due to the dual kinetic constraints of fast dye regeneration and slow recombination.

Ferrocene, Fc, was the first alternative redox shuttle to receive significant attention. [9,10] It was demonstrated that Fc is an excellent dye regenerator; however Fc^+ suffers from fast recombination. [10,11] The fast recombination was recently alleviated by employing a novel blocking sensitizer, which allowed efficiencies of nearly 8 % to be achieved. [7] Unfortunately, Fc^+ is unstable towards attack by oxygen and pyridines employed in typical electrolytes, which precludes the Fc^+/Fc from being used as a practical redox shuttle. [7,11] Recently a Ni(III)/(IV) bis(dicarbollide) complex was reported as a new fast redox shuttle for DSSCs which exhibited promising results.[8] The difficult synthesis of these Ni-based metallacarboranes makes them relatively inaccessible for further investigation by other groups, however. The best alternative redox shuttle to date consists of cobalt(III/II) polypyridyl complexes.[12] In early 2010, a breakthrough paper by Feldt *et al.* reported that a DSSC employing the cobalt tris-bipyridine, $[Co(bpy)_3]^{3+/2+}$, redox shuttle could achieve an efficiency of 6.7 % under full sun illumination when combined with an organic dye. [13] This was quickly followed by a landmark paper by Aswani Yella, *et al.* on a DSSC combining an organic dye with a Zn-porphyrin dye in conjunction with the $[Co(bpy)_3]^{3+/2+}$ redox couple which produced a new record power conversion efficiency of 12%. [6] An important feature of $[Co(bpy)_3]^{3+/2+}$ is the large inner-sphere reorganization energy which is attributed to the transition from high spin cobalt(II) to low spin cobalt(III). [14,15] This barrier is reflected in a very slow electron self-exchange rate constant of ~10 $M^{-1}s^{-1}$. [16] In addition to the slow self-exchange kinetics, the large reorganization energy results in slow recombination kinetics at TiO_2 electrodes.[17,18] On the other hand, the large reorganization energy also limits regeneration, where quantitative regeneration requires a driving force of ~0.5 eV. [19]

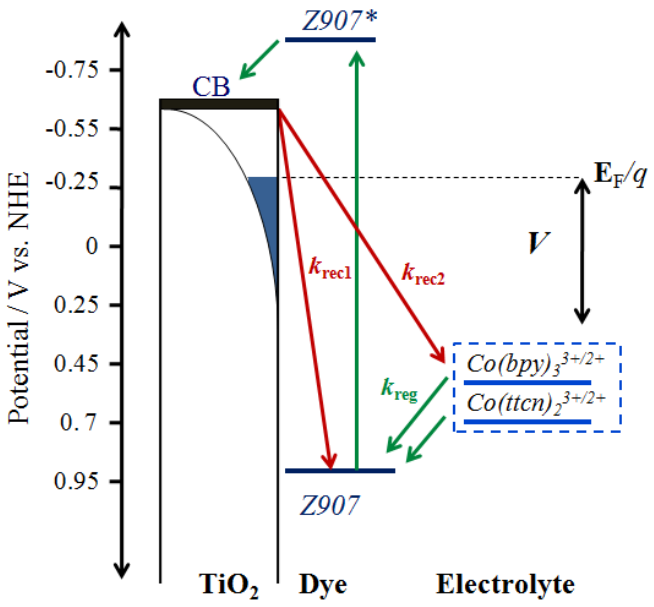

Figure 2.1 Energy diagram of a DSSC which shows the relevant kinetic processes involving $[Co(bpy)_3]^{3+/2+}$ and $[Co(ttcn)_2]^{3+/2+}$: dye regeneration (k_{reg}), recombination to the oxidized dye (k_{rec1}) and recombination to the Co(III) redox species (k_{rec2}).

We reasoned that it would be advantageous to have a redox couple capable of efficient dye regeneration with a minimal driving force, like ferrocene, but that is stable and transparent, like $[Co(bpy)_3]^{3+/2+}$. In this work we therefore introduce a low spin cobalt(II) complex as a redox shuttle in DSSCs: cobalt bis-trithiacyclononane, $[Co(ttcn)_2]^{3+/2+}$. [20–23] The chemical structure of $[Co(ttcn)_2]^{3+/2+}$ is displayed in figure 2.2. Magnetic susceptibility measurements of $[Co(ttcn)_2]^{2+}$ determined an effective magnetic moment, μ_{eff}, ~1.7 – 1.8 μ_B, indicating a low-spin d7 electronic configuration ($t_{2g}^6e_g^1$). [20,23] For comparison, $[Co(bpy)_3]^{2+}$ complexes have a μ_{eff} ~4.5 μ_B and are generally high spin ($t_{2g}^5e_g^2$). [15,24,25] The formal potential of $[Co(ttcn)_2]^{3+/2+}$ is 0.69 V vs NHE, which is ~60 mV positive of $[Co(bpy)_3]^{3+/2+}$, thus potentially allowing somewhat greater photovoltages, as shown in figure 2.3. The relatively fast $[Co(ttcn)_2]^{3+/2+}$ self exchange rate constant of ~10^5 $M^{-1}s^{-1}$, previously determined by NMR line broadening measurements, is also consistent with a low spin Co(II) species. [26] By contrast, the self exchange rate constant of

$[Co(bpy)_3]^{3+/2+}$ is ~10 $M^{-1}s^{-1}$. [16] The four order of magnitude higher self-exchange rate constant compared to $[Co(bpy)_3]^{3+/2+}$ should translate into approximately 100-fold faster regeneration kinetics; alternatively the faster regeneration kinetics can be exploited to decrease the driving force required for efficient regeneration. [27] Further, the $[Co(ttcn)_2]^{2+}$ low-spin octahedral complex is known to be quite stable with a formation constant of ~10^{14}, consistent with the reversible behavior indicated by cyclic voltammetry measurements, shown in figure 2.3. [23] In addition, absorption spectra indicate minimal competitive light absorption with the sensitizer, figure 2.4. Importantly, this complex is very simple to make from commercially available reagents and readily scalable and accessible to other researchers.

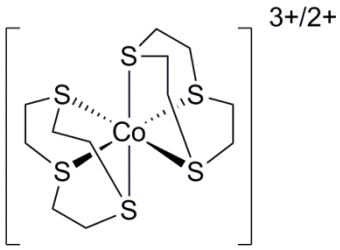

Figure 2.2 Chemical structure of $[Co(ttcn)_2]^{3+/2+}$.

2.3 Experimental

2.3.1 Solar cell preparation

Photoelectrodes were prepared on 12 Ω cm^{-2} FTO-coated glass (Hartford Glass) cleaned by sonicating in soap water solution, sonicating in isopropanol, ethanol, acetone, and then heating to 500 °C. Blocking layers of TiO_2 were deposited using 500 or 1000 ALD cycles (500 cycles for cells with electrolyte composition 1, and 1000 cycles for the rest) of titanium isopropoxide (TIPS, Aldrich) and water as precursors with a Savannah 100 instrument (Cambridge Nanotech, Inc.). TiO_2 was grown at 225 °C using reactant exposure times of 0.3 s and 0.015 s for TIPS and H_2O, respectively, and nitrogen purge times of 5 s between exposures. A transparent TiO_2 nanoparticle

layer (electrode area 0.36cm^2) was prepared by doctor blading a paste of TiO_2 nanoparticles (Ti-Nanoxide HT/SP, Solaronix) on the FTO. The resulting electrodes were annealed at 325 ^oC for 5 min, 375 ^oC for 5 min, 450 ^oC for 5 min, 500 °C for 15 min in air. TiO_2 film thickness, d, was measured using a Dektak3 Surface Profiler to be ~8 μm. Alumina was deposited immediately following removal from the oven by ALD using trimethylaluminum (TMA, Aldrich) and water as precursors. Al_2O_3 was grown at 250 °C using reactant exposure times of 10 s for both precursors and nitrogen purge times of 10 s between exposures. The TiO_2 electrodes were heated to 500 ^oC for 30 min, cooled to 100 ^oC, and immersed in dye solution (0.5 mM solution of Ru(2,2′-bipyridine-4,4′-dicarboxylato)(4,4'-di-nonyl-2, 2'-bipyridyl)$(NCS)_2$, Z907 from Sigma-aldrich, in ethanol or 0.3 mM solution of 2-Cyano-3-[5‴-(9-ethyl-9*H*-carbazol-3-yl)-3′,3″,3‴,4-tetra-*n*-hexyl-[2,2′,5′,2″,5″,2‴]-quater thiophen-5-yl] acrylic acid, MK2 dye from Sigma-aldrich, in 1:1:1 mixture of toluene: acetonitrile: tert-butanol). 10 equivalents of chenodeoxycholic acid were added during dye soaking for some of the optimized cells. After 20-24 hours, they were rinsed with acetonitrile. A ~25 μm thick Surlyn frame (Solaronix) was sandwiched between the TiO_2 nanoparticle electrode and a platinized FTO electrode, and light pressure was applied at 150 ^oC to seal the cell. Electrolyte was filled by capillary force through the two pre-drilled holes on the platinum counter electrode, and sealed with microglass and Surlyn film. Electrolyte compositions used are listed in table 2.7.

2.3.2 Synthesis of cobalt redox couples

$[Co(ttcn)_2](PF_6)_2$ and $[Co(ttcn)_2](PF_6)_3$ ($[Co(ttcn)_2](TFSI)_2$) and $[Co(ttcn)_2](TFSI)_3$))

1,4,7-trithiacyclononane, $Co(BF_4)_2•6H_2O$, ammonium hexafluorophosphate (NH_4PF_6), and $NOPF_6$ were used as received from Aldrich. 2 equiv of 1,4,7-trithiacyclononane was added to ethanol solution of $Co(BF_4)_2•6H_2O$ result purple precipitation $[Co(ttcn)_2](BF_4)_2$. Dissolve

$[Co(ttcn)_2](BF_4)_2$ in water and add excess NH_4PF_6 (or LiTFSI, lithium bis(trifluoromethanesulfonyl)imide) to precipitate $[Co(ttcn)_2](PF_6)_2$ ($[Co(ttcn)_2](TFSI)_2$). Further oxidation by adding 1 equiv $NOPF_6$ (or AgTFSI) to $[Co(ttcn)_2](PF_6)_2$ ($[Co(ttcn)_2](TFSI)_2$) in acetonitrile (or acetonitrile and DCM solvent mixture) will yield $[Co(ttcn)_2](PF_6)_3$ ($[Co(ttcn)_2](TFSI)_3$). The compounds are used after re-crystallization from acetonitrile using diethyl ether and dried under vacuum. Elemental analysis results are listed in table 2.8.

$[Co(bpy)_3](PF_6)_2$ and $[Co(bpy)_3](PF_6)_3$ ($[Co(bpy)_3](TFSI)_2$ and $[Co(bpy)_3](TFSI)_3$))

2,2′-bipyridine (bpy), cobalt chloride ($CoCl_2•6H_2O$), lithium hexaflurophosphate ($LiPF_6$), ammonium hexafluorophosphate (NH_4PF_6), and $NOPF_6$ were used as received from Aldrich. 4-tert-butylpyridine was purified by distillation. Solvents were the highest grade available and were used as received. The compound $[Co(bpy)_3](PF_6)_2$ was prepared as a modified literature method.[22] 1 equiv of $CoCl_2•6H_2O$ dissolved in a minimal amount of methanol was added to a methanolic solution containing 3 equiv of the bpy ligand, and the solution was stirred for 2 h. An excess of ammonium hexafluorophosphate was used to precipitate a yellow compound ($[Co(bpy)_3](PF_6)_2$) that was filtered, washed with ethanol, methanol, and ether, dried under vacuum, and used without further purification. Cobalt (III) tris(2,2′-bipyridyl) hexafluorophosphate, $[Co(bpy)_3](PF_6)_3$, was prepared as follows. To a stirring solution of $[Co(bpy)_3](PF_6)_2$ in minimal acetonitrile, 1.2 equivalents of $NOPF_6$ dissolved in minimal acetonitrile was added slowly. The solution was allowed to stir for 30 minutes before being rotary evaporated dry. The solid was re-dissolved in minimal acetonitrile, precipitated with diethyl ether, collected via vacuum filtration and washed with methanol, water, and diethyl ether. The resulting $[Co(bpy)_3](PF_6)_3$ was used after re-crystallizing from acetonitrile using diethyl ether and drying under vacuum. $[Co(bpy)_3](TFSI)_2$ was prepared in a similar way as $[Co(bpy)_3](PF_6)_2$. Instead of using NH_4PF_6, LiTFSI was used to

precipitate the product out, and AgTFSI was employed to oxidize $[Co(bpy)_3](TFSI)_2$ to $[Co(bpy)_3](TFSI)_3$ in a similar way preparing $[Co(ttcn)_2]^{3+}$. Elemental analysis results are listed in table 2.8.

2.3.3 DSSCs device characterization

Photoelectrochemical measurements were performed with a Gamry Reference 600 potentiostat interfaced with a Xe Arc Lamp. An AM 1.5 solar filter was used to simulate sunlight at 100 mW cm^{-2}. An additional 400 nm long-pass filter was used to prevent direct excitation of the TiO_2 in all light *J-V* measurements. A Horiba Jobin Yyon MicroHR was used for monchromatic light for IPCE measurements.

Open circuit voltage decay measurements are done at open circuit. The cell was in the dark at the beginning of the measurement, and then the lights was turned on and let the voltage stabilize, followed by switching the light off and recording the decay of the voltage. Lifetime data was transformed from the voltage decay part of the measurement through equation (1). The stabilized voltage data when light was on was used in V_{oc} vs light intensity plot. OCVD measurements were taken at different light intensities by using absorptive neutral density filters, (Thorlabs NEK01S).

$$\tau_{\mathrm{n}} = \frac{k_{\mathrm{B}}T}{q}\left(\frac{dV_{\mathrm{OC}}}{dt}\right)^{-1} \quad (1)$$

Current transients are taken at short circuit. The cell was in the dark at the beginning, and then light source was turned on and off every 2 seconds. Current transient measurements were also taken at different light intensity by using absorptive neutral density filters (Thorlabs NEK01S). The limiting current when light was on was used in J_{sc} vs light intensity plot.

All electrochemical impedance spectroscopy (EIS) measurements were performed in the dark with an Autolab PGSTAT 126N. The impedance spectra were recorded at direct applied voltages

from -0.4 to -0.8 V, stepped in 25 mV increments, with a 10 mV alternating potential superimposed on the direct bias. Each impedance measurement consisted of frequency sweeps from 5×10^{-2} to 1×10^{5} Hz in equally spaced logarithmic steps.

Cyclic voltametry was performed with an Autolab PGSTAT128N potentiostat with a Au disk or Pt disk working electrode, a high surface area Pt mesh counter electrode, and Ag/Ag^{+} as reference, ferrocene was used as an internal reference, 0.1 M Bu_4NPF_6 as a supporting electrolyte.

UV-Vis data was acquired using a Lambda 35 (Perkinelmer) spectrometer, and 400 times diluted electrolyte are used for measurement (electrolyte composition 1). The spectrochemical cell width used here is 1cm which is 400 times of the thickness of the Surlyn film spacer used in the sandwich DSSCs, so the electrolytes were diluted 400 times for measurement to get the actual absorbance of electrolyte in DSSCs.

2.4 Result and Discussions

2.4.1 DSSCs performance optimization via blocking dye and blocking layer

Figure 2.3 shows *J-V* curve and incident photon to current efficiency, IPCE, plots of a DSSC sensitized with the commonly used N719 dye, $(Bu_4N)_2$[Ru(4-carboxy,4'-carboxylato-2,2'-bipyridine)$_2$(NCS)$_2$], employing an electrolyte consisting of 80 mM $[Co(ttcn)_2]^{2+}$, 8 mM $[Co(ttcn)_2]^{3+}$, 100 mM $LiPF_6$ and 100 mM *tert*-butyl pyridine. Some attempt was made to optimize this electrolyte through variations of the counter ion and concentrations of the redox active constituents. The maximum IPCE achieved of 8 %, however, is still quite low. Due to the more positive potential and larger self-exchange rate constant of $[Co(ttcn)_2]^{3+/2+}$ compared to $[Co(bpy)_3]^{3+/2+}$, it is reasonable to expect faster recombination which can limit the electron diffusion length and thus the IPCE.[2] The sensitizer Z907, [Ru(4,4'-dicarboxylato-2,2'-bipyridine)(4,4'-dinonyl-2,2'-bipyridine) (NCS)$_2$], which contains nonyl chains on one of the bpy

ligands, has been shown to block recombination with outersphere redox shuttles; [28] we therefore employed Z907 in combination with the same $[Co(ttcn)_2]^{3+/2+}$ electrolyte. The IPCE maximum increased to nearly 20 % with this sensitizer. This result is consistent with the IPCE being controlled by recombination. We therefore additionally applied one ALD coating of alumina on the TiO_2 substrate prior to immersing it in the sensitizer solution, which has been demonstrated to reduce recombination and thereby improve the efficiency of DSSCs employing alternative redox shuttles.[29] Through these simple modifications to the photoanode and sensitizer, a promising IPCE of 25 % was achieved. In order to confirm that it is indeed recombination that accounts for the differences in IPCEs, we also performed open-circuit voltage decay (OCVD) measurements on these cells.[30] The voltage decay data (*V*oc vs. time) were transformed into electron lifetimes. [30] The electron lifetime at a given potential is inversely proportional to the rate of recombination, thus allowing for a quantitative comparison.[18] The lifetimes clearly increase by approximately an order of magnitude for $[Co(ttcn)_2]^{3+/2+}$ with Z907 compared to N719, and is consistent with previous reports.[28] The addition of an alumina blocking layer further reduces recombination by approximately another order of magnitude, also consistent with a previous reports. [29,31] These results are displayed in figure 2.4.

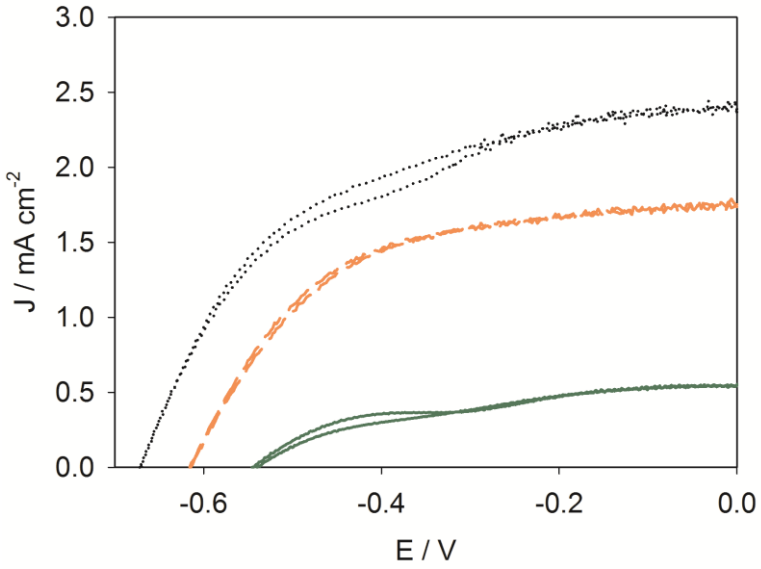

a)

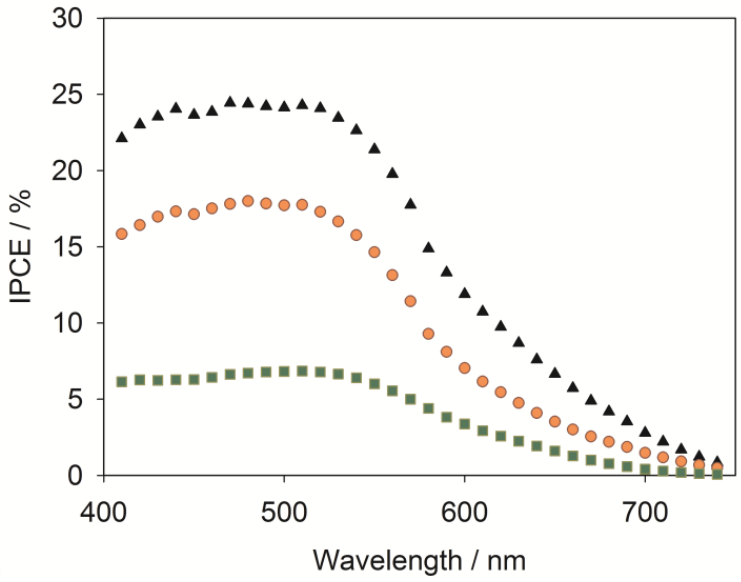

b)

Figure 2.3 a) *J-V* curves of DSSCs employing $[Co(ttcn)_2]^{3+/2+}$ and dye N719 (green solid), Z907 (orange long dashed), Z907 and $1Al_2O_3$ layer(black dotted) applying electrolyte composition 1; b)Plot of IPCE's for $[Co(ttcn)_2]^{3+/2+}$ with N719 (Green squares), Z907 (red circles) and Z907 with the addition of one ALD cycle of alumina (black triangles).

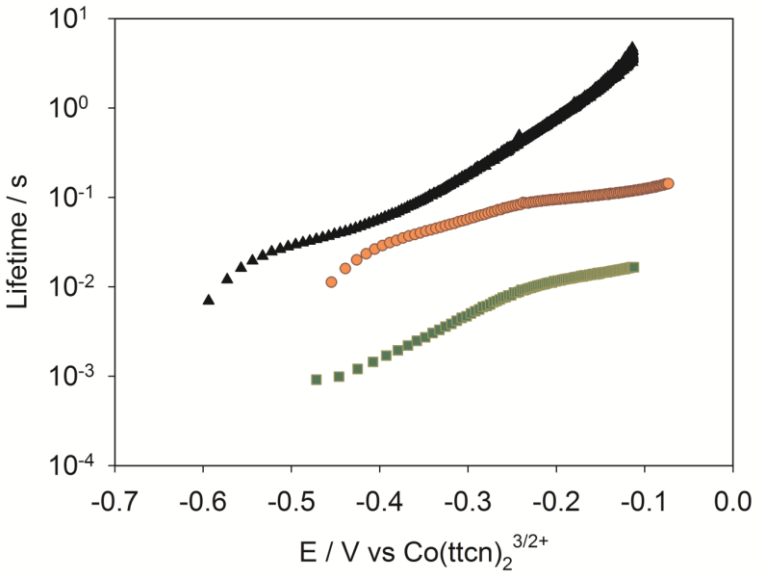

Figure 2.4 Lifetime vs. voltage plots of DSSCs employing $[Co(ttcn)_2]^{3+/2+}$ and dye N719 (green square), Z907 (orange circle), Z907 and $1Al_2O_3$ layer (black triangle) applying electrolyte composition 1.

2.4.2 DSSCs performance limited by recombination using low spin $[Co(ttcn)_2]^{3+/2+}$

Since many factors can affect the IPCE and *J-V* behavior of DSSCs, [2] making comparisons with literature results is difficult. We therefore compared the performance of $[Co(ttcn)_2]^{3+/2+}$ with $[Co(bpy)_3]^{3+/2+}$ (the current champion redox shuttle) using the nominally identical photoanodes, electrolyte concentrations and counter ions; optimized electrolytes consisted of 150 mM of the reduced redox shuttle, 8 mM of the oxidized redox shuttle and 100 mM of LiTFSI ($TFSI^-$: bis(trifluoromethane)sulfonimide anion). In addition, 10 mM of chenodeoxycholic acid, Cheno, was added to the electrolyte in place of *tert*-butyl pyridine since this was found to improve the performance. Figure 2.5 shows plots of representative *J-V* curves for DSSCs containing these two electrolytes. The performance of the cell containing $[Co(bpy)_3]^{3+/2+}$ produces ~50 % higher photocurrent densities and ~60 mV higher *V*oc compared to $[Co(ttcn)_2]^{3+/2+}$. Comparisons of IPCE,

J-V curves under 0.1 sun illumination and current transients allowed us to rule out mass transport as causing the difference in performance , see table 2.5 in Appendix.

Electrochemical impedance spectroscopy, EIS, measurements were therefore performed in order to determine the cause of the differences in *J-V* behavior of $[Co(bpy)_3]^{3+/2+}$ and $[Co(ttcn)_2]^{3+/2+}$. Representative Nyquist plots are shown in the appendix, figure 2.11. All EIS data were fit to the equivalent circuit developed by Bisquert and co-workers ,see figure 2.10 in Appendix, which has been demonstrated to accurately describe electron transfer behavior in DSSCs.[30] Fitted results produced values of the charge transfer resistance, R_{CT}, and chemical capacitance of the TiO_2, C_μ. The R_{CT} is inversely proportional to the rate of recombination to the oxidized form of redox couple in the electrolyte for a given potential dependant electron concentration in the TiO_2, *n*. Since the two electrolytes have different solution potentials, a given applied voltage would produce different potentials in the TiO_2. The C_μ is proportional to the occupancy of states in the TiO_2, therefore comparing values of R_{CT} at a given C_μ would reflect differences in recombination rate constants (see Scheme 1). Figure 2.7 shows plots of R_{CT} vs. C_μ for the two electrolytes examined. $[Co(ttcn)_2]^{3+/2+}$ has smaller R_{CT} than $[Co(bpy)_3]^{3+/2+}$ at a given C_μ which indicates a faster recombination rate constant. The decreased electron lifetime with $[Co(ttcn)_2]^{3+/2+}$ can account for the differences in charge collection yield and thus photocurrent as well as the lower photovoltage. [2]

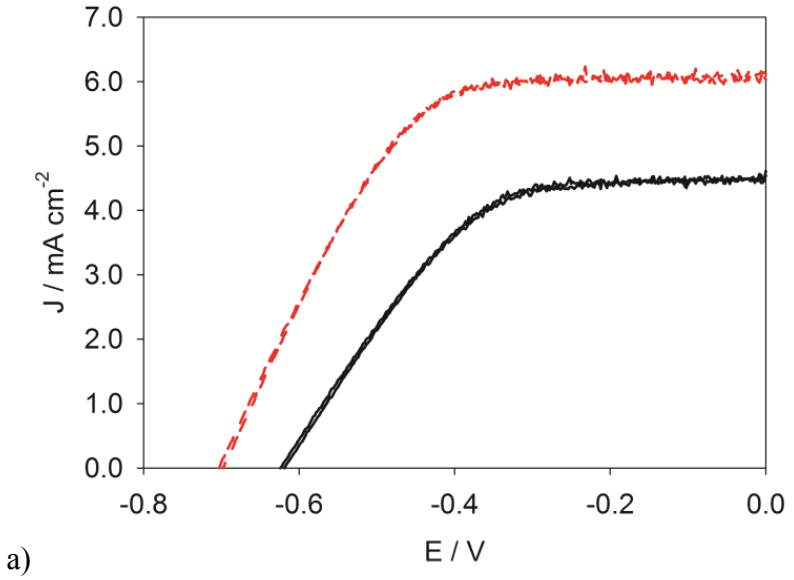

a)

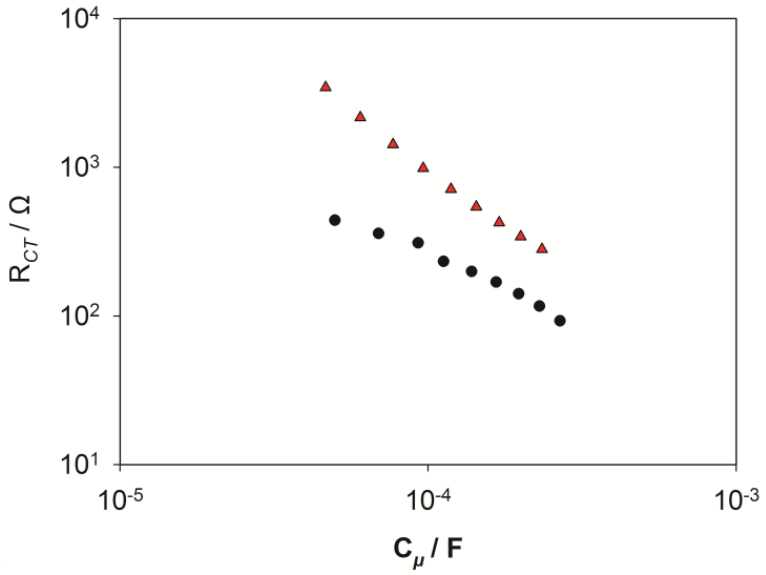

b)

Figure 2.5 a) *J-V* curves of DSSCs employing $[Co(ttcn)_2]^{3+/2+}$ (black), $[Co(bpy)_3]^{3+/2+}$ (red); b) Comparison of charge transfer resistance, R_{CT} vs. chemical capacitance C_μ for the $[Co(ttcn)_2]^{3+/2+}$ (black circle) and $[Co(bpy)_3]^{3+/2+}$ (red triangle) electrolytes.

2.4.3 Improving charge collection via strongly absorbing organic dye

In addition to employing steric blocking groups on sensitizers to minimize recombination (e.g. Z907), increasing the molar extinction coefficient of the sensitizer reduces the demands of the necessary diffusion length needed for good charge collection efficiencies. Both of these strategies were successfully demonstrated first by Feldt et. al., and later by Bach's group, by employing strongly absorbing, bulky organic sensitizers with outersphere redox shuttles.[7,13] We therefore employed the sensitizer MK-2 with the $[Co(ttcn)_2]^{3+/2+}$ redox shuttles. The ground state potential of MK-2 is 0.889 V vs NHE, which results in only ~200 mV driving force for regeneration by $[Co(ttcn)_2]^{2+}$.[28,32] Figure 2.6 shows a *J-V* curve of this system. The performance with the MK-2 dye is substantially improved compared to DSSCs employing Z907, with an efficiency of over 2 % being achieved for the $[Co(ttcn)_2]^{3+/2+}$ / MK-2 system.

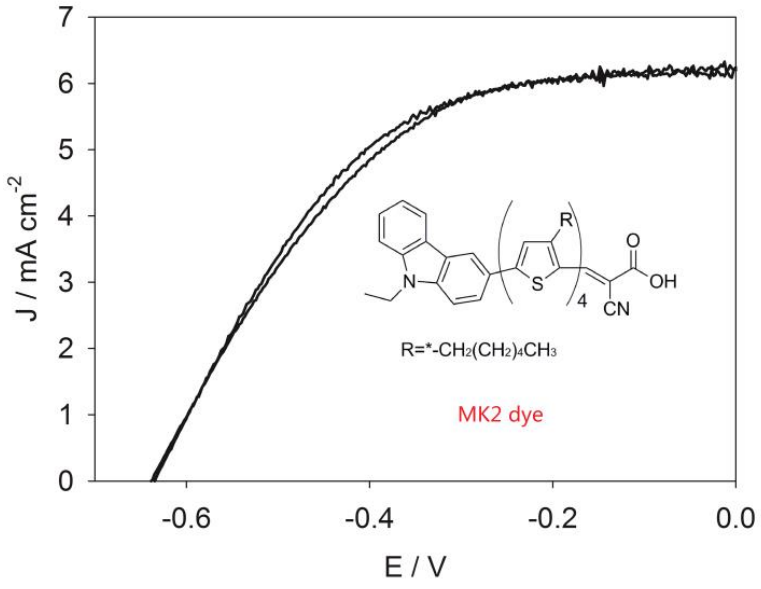

Figure 2.6 *J-V* curve of DSSC employing $[Co(ttcn)_2]^{3+/2+}$ in combination with MK-2 sensitizer (structure shown in figure) which produces an efficiency of > 2 %.

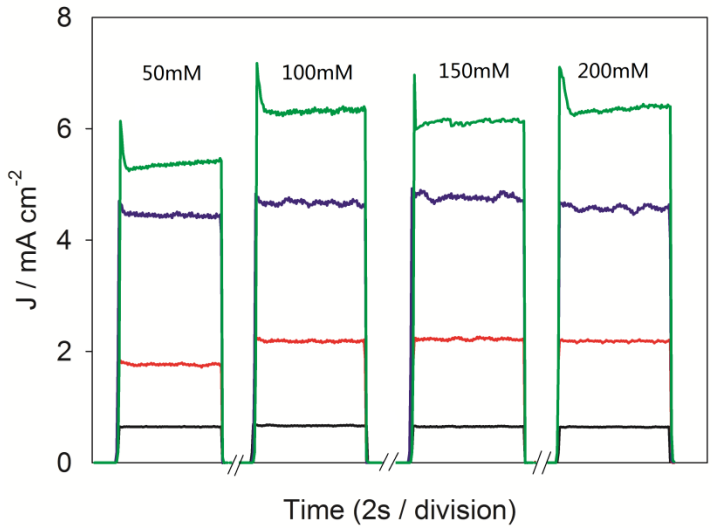

Figure 2.7 Current transients for cells containing different concentrations of Co(II) under different light intensities, 10 mW cm^{-2} (black), 32 mW cm^{-2} (red), 63 mW cm^{-2} (blue), and 100 mW cm^{-2} (green).

2.4.4 Efficient dye regeneration of DSSCs using $[Co(ttcn)_2]^{3+/2+}$

In order to test whether regeneration is limiting the performance of the MK-2 / $[Co(ttcn)_2]^{3+/2+}$ system, current transients and open circuit voltage decay measurements were taken at different light intensities for variant Co(II) concentrations. The short circuit photocurrent density increases linearly with light intensity until 1 sun (100 mW cm^{-2}) illumination. At 1 sun there is a spike in photocurrent which quickly decays to a slightly lower steady state value. The instantaneous photocurrent reflects the kinetically achievable photocurrent, comparable to that determined by integrating IPCE plots. The slightly lower steady state photocurrent is attributed to photocurrents limited by the diffusion of the Co(III) species to the counter electrode. [31] Nominally identical behavior is observed for all Co(II) concentrations except the lowest (50mM), where the spike at 1 sun intensity is lower by ~1 mA cm^{-2}. We attribute this diminished performance to the low Co(II) concentration not producing a sufficient dye regeneration rate to compensate the increasing regeneration demand at high light intensities. See figure 2.8 in a plot of steady state photocurrent

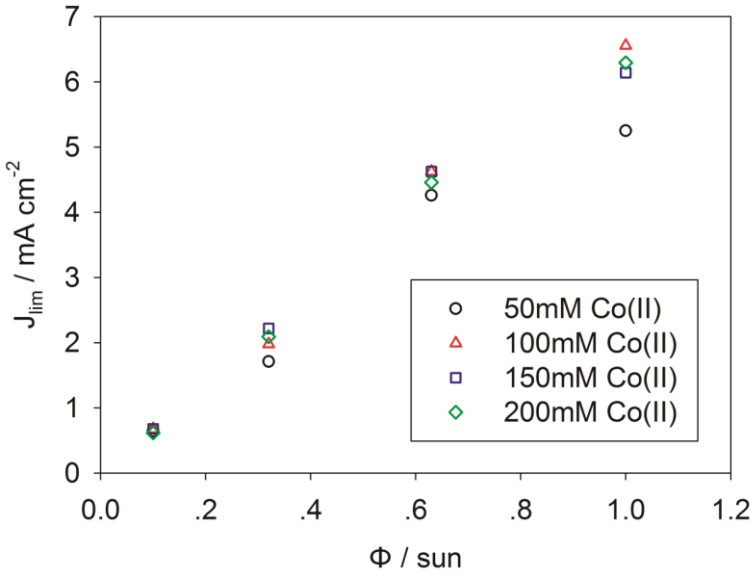

a)

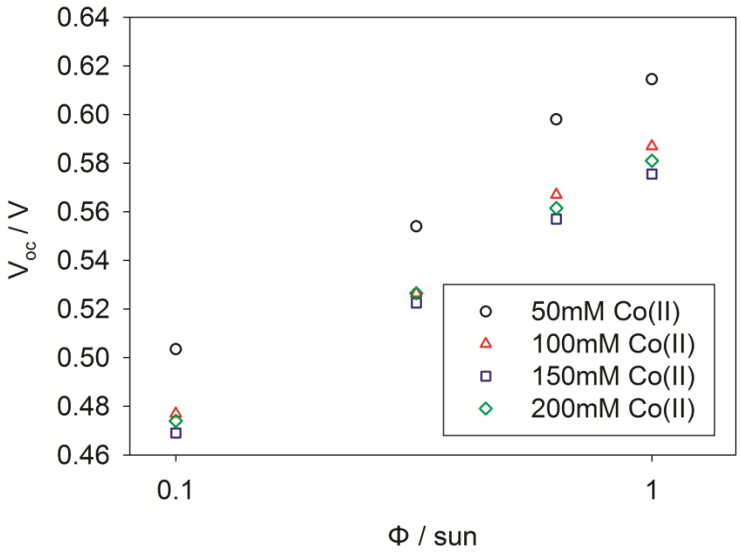

b)

Figure 2.8 a) Average limiting current density vs light intensity for $[Co(ttcn)_2]^{3+/2+}$ electrolyte with variant Co(II) concentrations; b) Average open circuit voltage vs light intensity for $[Co(ttcn)_2]^{3+/2+}$ electrolyte with variant Co(II) concentrations.

density vs. light intensity. While fast recombination therefore still limits the overall performance, initial attempts at overcoming this hurdle through dye variation clearly demonstrates the promise of the $[Co(ttcn)_2]^{3+/2+}$ redox shuttle.

2.5 Conclusions

In summary, we presented a new motif of low spin cobalt redox shuttles for use in DSSCs. These results illustrate that the DSSC performance can be controlled through manipulation of the spin state of cobalt complexes via judicious choice of ligand. Comparable efficiencies to $[Co(bpy)_3]^{3+/2+}$ were achieved, however the much larger self-exchange rate constants indicate lower driving forces for efficient dye regeneration should be necessary thus allowing increased currents and/or voltages when used in combination with optimized sensitizers and photoanode materials. A comprehensive investigation is presented in chapter 3. We note that the initial proof-of-concept performance of $[Co(ttcn)_2]^{3+/2+}$ reported herein is already quite high for an alternative redox shuttle in DSSCs and we expect that further understanding of the effects of electrolyte composition, solvent, sensitizer and photoanode on regeneration and recombination will allow the $[Co(ttcn)_2]^{3+/2+}$ redox shuttle to produce very high efficiencies.

APPENDIX

APPENDIX

Table 2.1 Peak values and potentials of cyclic voltammograms in Figure 2.3.

Redox Couple	$E_{p,a}$	$E_{p,c}$	ΔE	E_{mid}
	V vs. Ag/AgCl	V vs. Ag/AgCl	mV	V vs. Ag/AgCl
$[Co(bpy)_3]^{3+/2+}$	0.377	0.306	71	0.342
$[Co(ttcn)_2]^{3+/2+}$	0.439	0.365	74	0.402
$Fc^{0/+}$	0.438	0.366	72	0.402

Table 2.2 *J-V* charateristics of DSSCs employing $[Co(ttcn)_2]^{3+/2+}$ and $[Co(bpy)_3]^{3+2+}$ applying electrolyte composition 2 and dye Z907 at 1sun light intensity.

Electrolyte		$[Co(ttcn)_2]^{3+/2+}$			$[Co(bpy)_3]^{3+/2+}$		
Cell NO.		1	2	3	1	2	3
η	%	1.43	1.12	1.26	2.16	1.90	1.94
J_{sc}	mA cm^{-2}	3.94	3.50	3.70	5.46	5.17	5.04
V_{oc}	V	0.57	0.54	0.55	0.68	0.66	0.65
FF		0.63	0.59	0.61	0.58	0.55	0.59

Table 2.3 *J-V* charateristics of DSSCs employing $[Co(ttcn)_2]^{3+/2+}$ and $[Co(bpy)_3]^{3+2+}$ applying electrolyte composition 2 and dye Z907 at 0.1sun light intensity.

Electrolyte		$[Co(ttcn)_2]^{3+/2+}$			$[Co(bpy)_3]^{3+2+}$		
Cell NO.		1	2	3	1	2	3
η	%	1.06	0.79	0.38	2.05	2.11	2.06
J_{sc}	mA cm^{-2}	0.31	0.25	0.27	0.52	0.52	0.51
V_{oc}	V	0.46	0.41	0.39	0.55	0.56	0.55
FF		0.73	0.75	0.37	0.71	0.72	0.74

Table 2.4 *J-V* charateristics of DSSCs employing $[Co(ttcn)_2]^{3+/2+}$ electrolyte applying electrolyte composition 3 and dye MK2 at 1sun and 0.1 sun light intensity.

Light intensity		1 sun			0.1 sun	
Cell NO.		1	2	3	1	2
η	%	2.05	2.03	1.71	2.05	2.22
J_{sc}	mA cm^{-2}	6.19	6.24	5.13	0.60	0.66
V_{oc}	V	0.64	0.64	0.60	0.49	0.49
FF		0.51	0.51	0.55	0.71	0.69

Table 2.5 *J-V* charateristics of DSSCs employing $[Co(ttcn)_2]^{3+/2+}$ with variant Co(II) concentrations, Co(III) 8mM, LiTFSI 0.1M and Chenodeoxylic acid 10mM with dye MK2 at 0.1sun light intensity.

Co(II) conc.		50mM			100mM			150mM			
Cell NO.		1	2	3	1	2	3	1	2	3	4
η	%	2.52	2.40	2.62	2.56	2.61	2.51	2.00	2.30	2.07	2.45
J_{sc}	mA cm^{-2}	0.88	0.65	0.66	0.73	0.67	0.69	0.54	0.66	0.59	0.65
V_{oc}	V	0.53	0.54	0.55	0.51	0.53	0.50	0.50	0.51	0.49	0.51
FF		0.54	0.68	0.73	0.69	0.74	0.72	0.75	0.68	0.72	0.74

Table 2.6 Electrolyte compositions used in DSSCs assembly.

Electrolyte	Counter ion	Co(II)	Co(III)	Li^+	4-tert-Butylpyridine	Chenodeoxycholic acid
		mM	mM	M	M	mM
1	PF_6^-	80	8	0.1	0.1	none
2	$TFSI^-$	150	8	0.1	none	10
3	$TFSI^-$	200	8	0.1	none	10

Table 2.7 Elemental analysis results of synthesized cobalt redox couples.

Compound		Calculated			Found		
		C%	H%	N%	C%	H%	N%
$[Co(ttcn)_2](PF_6)_2$	$C_{12}H_{24}S_6CoP_2F_{12}$	20.31	3.41	0	19.44	3.12	0.04
$[Co(ttcn)_2](PF_6)_3$	$C_{12}H_{24}S_6CoP_3F_{18}$	16.87	2.83	0	17.06	2.55	0.10
$[Co(ttcn)_2](TFSI)_2$	$C_{18}H_{24}N_2CoO_8S_{10}F_{12}$	19.61	2.47	2.86	19.77	2.70	3.00
$[Co(ttcn)_2](TFSI)_3$	$C_{18}H_{24}N_3CoO_{12}S_{12}F_{18}$	17.16	1.92	3.33	17.28	1.77	3.46
$[Co(bpy)_3](PF_6)_2$	$C_{30}H_{24}N_6CoP_2F_{12}$	44.08	2.96	10.28	43.01	3.16	10.40
$[Co(bpy)_3](PF_6)_3$	$C_{30}H_{24}N_6CoP_3F_{18}$	37.44	2.51	8.73	38.02	2.60	9.91
$[Co(bpy)_3](TFSI)_2$	$C_{34}H_{24}N_8CoO_8S_4F_{12}$	37.54	2.22	10.30	37.00	2.30	10.50
$[Co(bpy)_3](TFSI)_3$	$C_{36}H_{24}N_9CoO_{12}S_6F_{18}$	31.61	1.77	9.22	33.00	1.79	9.50

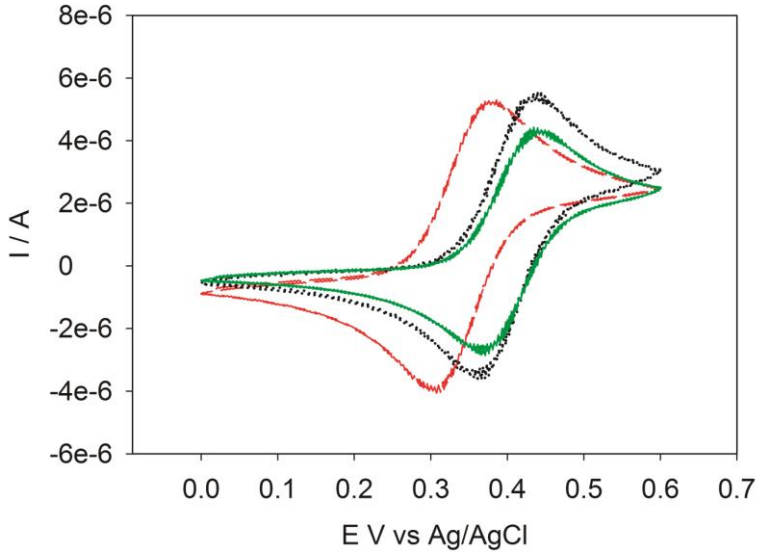

Figure 2.9 Cyclic voltammogram of $[Co(ttcn)_2]^{3+/2+}$ (black dotted), $[Co(bpy)_3]^{3+/2+}$ (red dashed) and $Fc^{0/+}$ (green solid) as a standard.

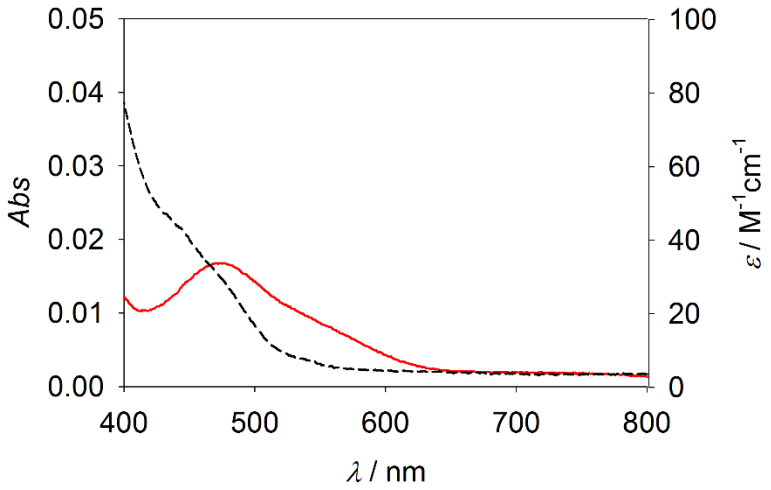

Figure 2.10 Absorbance of 400 times diluted electrolyte composition 1 $[Co(ttcn)_2]^{3+/2+}$ (black solid), $[Co(bpy)_3]^{3+/2+}$ (red dashed). Molar extinction coefficient is calculated based on the Co(II) concentration for an electrolyte composition with Co(II)/Co(III) concentration ratio of 10.

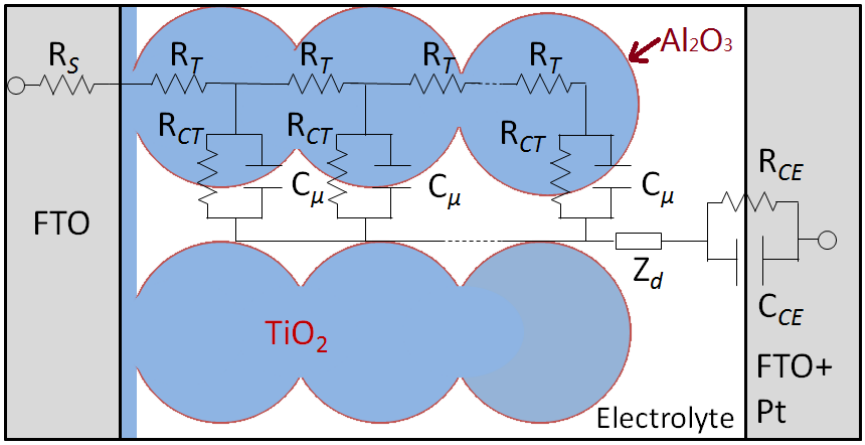

Figure 2.11 Equivalent circuit used for impedance data fitting. In this model RS is the series resistance resulting from the FTO and contact resistance of the cell, R_T is the transport resistance through the TiO_2 film, R_{CT} is the charge transfer resistance of recombination between electrons in the TiO_2 and the oxidized form of the redox shuttle in solution, C_μ is the chemical capacitance of the TiO_2 film, Z_d is the Warburg impedance resulting from the diffusion of redox shuttle between the electrodes, R_{CE} is the charge transfer resistance at the counter electrode, and C_{CE} is the double layer capacitance at the counter electrode.

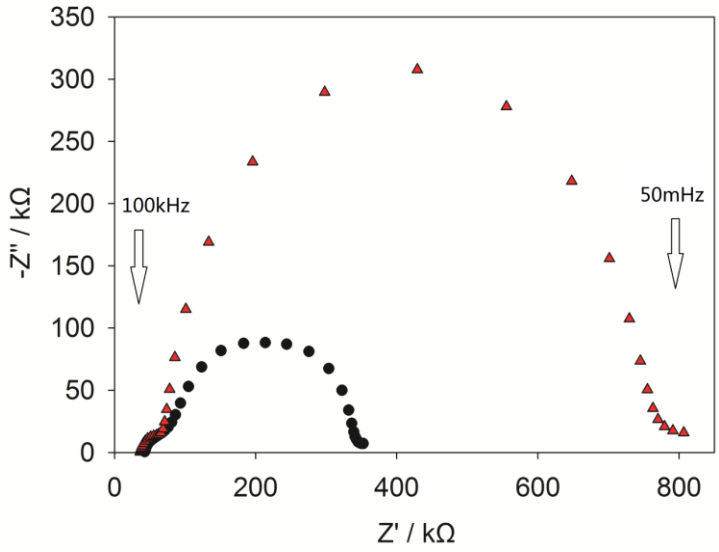

Figure 2.12 Electrochemical impedance spectra of sandwish DSSC at same C_{μ} (10^{-4} F) for the $[Co(ttcn)_2]^{3+/2+}$ (black circle), $[Co(bpy)_3]^{3+/2+}$ (red triangle) electrolytes applying electrolyte composition 2.

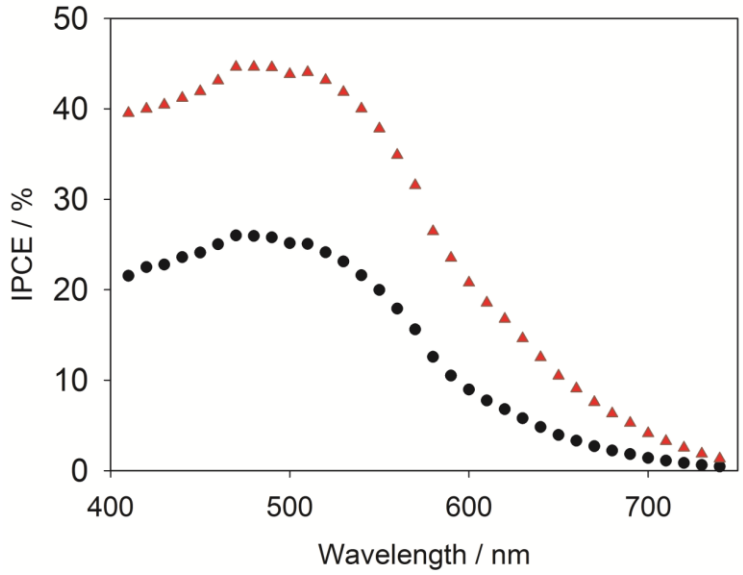

Figure 2.13 IPCE plots of DSSCs employing $[Co(ttcn)_2]^{3+/2+}$ (black circle), $[Co(bpy)_3]^{3+/2+}$ (red triangle) applying dye Z907 electrolyte composition 2.

REFERENCES

REFERENCES

(1) Grätzel, M.; O'Regan, B. C.; O'Regan, B.; Grätzel, M. *Nature* **1991**, *353*, 737–740.

(2) Hamann, T. W.; Ondersma, J. W. *Energy Environ. Sci.* **2011**, *4*, 370.

(3) Boschloo, G.; Hagfeldt, A. *Acc. Chem. Res.* **2009**, *42*, 1819–1826.

(4) Hagfeldt, A.; Boschloo, G.; Sun, L.; Kloo, L.; Pettersson, H. *Chem. Rev.* **2010**, *110*, 6595–6663.

(5) Ardo, S.; Meyer, G. J. *Chem. Soc. Rev.* **2009**, *38*, 115–164.

(6) Yella, A.; Lee, H.-W.; Tsao, H. N.; Yi, C.; Chandiran, A. K.; Nazeeruddin, M. K.; Diau, E. W.-G.; Yeh, C.-Y.; Zakeeruddin, S. M.; Grätzel, M. *Science* **2011**, *334*, 629–634.

(7) Daeneke, T.; Kwon, T.; Holmes, A. B.; Duffy, N. W.; Bach, U.; Spiccia, L. *Nat. Chem.* **2011**, *3*, 211–215.

(8) Li, T. C.; Spokoyny, A. M.; She, C.; Farha, O. K.; Mirkin, C. a; Marks, T. J.; Hupp, J. T. *J. Am. Chem. Soc.* **2010**, *132*, 4580–4582.

(9) Gregg, B. a.; Pichot, F.; Ferrere, S.; Fields, C. L. *J. Phys. Chem. B* **2001**, *105*, 1422–1429.

(10) Gregg, B. a. *Coord. Chem. Rev.* **2004**, *248*, 1215–1224.

(11) Hamann, T. W.; Farha, O. K.; Hupp, J. T. *J. Phys. Chem. C* **2008**, *112*, 19756–19764.

(12) Hamann, T. W. *Dalt. Trans.* **2012**, *41*, 3111–3115.

(13) Feldt, S. M.; Gibson, E. a; Gabrielsson, E.; Sun, L.; Boschloo, G.; Hagfeldt, A. *J. Am. Chem. Soc.* **2010**, *132*, 16714–16724.

(14) Liu, Y.; Jennings, J. R.; Huang, Y.; Wang, Q.; Zakeeruddin, S. M.; Gr, M. *J. Phys. Chem. C* **2011**, *115*, 18847–18855.

(15) Mosconi, E.; Yum, J.-H.; Kessler, F.; Gómez García, C. J.; Zuccaccia, C.; Cinti, A.; Nazeeruddin, M. K.; Grätzel, M.; De Angelis, F. *J. Am. Chem. Soc.* **2012**, *134*, 19438–19453.

(16) Weaver, M. J.; Yee, E. L. *Inorg. Chem.* **1980**, *19*, 1936–1945.

(17) Nakade, S.; Makimoto, Y.; Kubo, W.; Kitamura, T.; Wada, Y. *J. Phys. Chem. B* **2005**, *109*, 3488–3493.

(18) Ondersma, J. W.; Hamann, T. W. *J. Am. Chem. Soc.* **2011**, *133*, 8264–8271.

(19) Feldt, S. M.; Wang, G.; Boschloo, G.; Hagfeldt, A. *J. Phys. Chem. C* **2011**, *115*, 21500–21507.

(20) Weighardt, K.; Kueppers, H. J.; Weiss, J. *Inorg. Chem.* **1985**, *24*, 3067–3071.

(21) Kuppers, H.; Neves, A.; Pomp, I. C.; Ventur, D.; Wieghardt, I. K. *Inorg. Chem.* **1986**, *6*, 2400–2408.

(22) I, O.; Setzer, W. N.; Ogle, C. A.; Wilson, G. S.; Glass, R. S.; Trans, D.; Chim, F. L. I. *Inorg. Chem.* **1983**, *2*, 266–271.

(23) Wilson, G. S.; Swanson, D. D.; Glass, R. S. *Inorg. Chem.* **1986**, *25*, 3827–3829.

(24) Krivokapic, I.; Zerara, M.; Daku, M. L.; Vargas, A.; Enachescu, C.; Ambrus, C.; Tregenna-Piggott, P.; Amstutz, N.; Krausz, E.; Hauser, A. *Coord. Chem. Rev.* **2007**, *251*, 364–378.

(25) Gaddie, R. S.; Moss, C. B.; Elliott, C. M. *Langmuir* **2013**, *29*, 825–831.

(26) Chandrasekhar, S. .; McAuley, A. *Inorg. Chem.* **1992**, *31*, 480–487.

(27) Marcus, R. A.; Sutin, N. *Biochim. Biophys. Acta - Rev. Bioenerg.* **1985**, *811*, 265–322.

(28) Zaban, A.; Greenshtein, M.; Bisquert, J. *ChemPhysChem* **2003**, *4*, 859–864.

(29) Ondersma, J. W.; Hamann, T. W. *J. Phys. Chem. C* **2010**, *114*, 638–645.

(30) Bisquert, J.; Zaban, A.; Greenshtein, M.; Mora-Seró, I. *J. Am. Chem. Soc.* **2004**, *126*, 13550–13559.

(31) Nelson, J. J.; Amick, T. J.; Elliott, C. M. *J. Phys. Chem. C* **2008**, *112*, 18255–18263.

(32) Klahr, B. M.; Hamann, T. W. *J. Phys. Chem. C* **2009**, *113*, 14040–14045.

Chapter 3 Kinetics of Regeneration and Recombination Reactions in Dye Sensitized Solar Cells Employing Cobalt Redox Shuttles

* Josh Baillargeon is acknowledged for his contribution to chapter 3.4.1. Josh Baillargeon performed all measurements and calculations of the self-exchange rate constant and reorganization energy values which are used in following discussion section, chapter 3.

3.1 Abstract

The key to achieving high efficiency dye-sensitized solar cells (DSSCs) is the realization of a redox shuttle which exhibits quantitative dye regeneration with a minimal driving force. Since the electron diffusion length, L_n, is controlled by recombination to the redox shuttle, an optimal redox shuttle must balance the kinetics of these two key electron-transfer reactions. In this work the dye regeneration efficiency, η_{reg}, and the electron diffusion length were determined for DSSCs employing cobalt tris-bipyridine, $[Co(bpy)_3]^{3+/2+}$, and cobalt bis–trithiacyclononane, $[Co(ttcn)_2]^{3+/2+}$, redox shuttles from optical and incident photon to current efficiency, IPCE, measurements of the cells under front side and backside illumination directions. The regeneration of the D35cpdt dye was found to be quantitative with $[Co(ttcn)_2]^{3+/2+}$; however dye regeneration with the current champion redox shuttle $[Co(bpy)_3]^{3+/2+}$ is sub-optimal despite a larger driving force of the reaction. The electron diffusion length was found to be shorter for DSSCs with the $[Co(ttcn)_2]^{3+/2+}$ redox shuttle compared to $[Co(bpy)_3]^{3+/2+}$, however, due to faster recombination despite the smaller driving force for the reaction. The self-exchange rate constants of the two redox shuttles were determined from cross-exchange measurements and were found to differ by over four orders of magnitude. Application of Marcus theory allowed the difference in self-exchange rate constants to quantitatively account for the differences in regeneration efficiency and electron diffusion length of the two redox shuttles. Atomic Layer Deposition (ALD) was used to add a

single layer of alumina on the TiO_2 film prior to immersing it in the sensitizer solution; this treatment resulted in improved performance for DSSCs employing both redox shuttles, however the improvement was shown to arise from different causes. The alumina layer reduces recombination to the redox shuttle and thereby increases L_n for $[Co(ttcn)_2]^{3+/2+}$. The alumina layer was also shown to improve the dye regeneration efficiency for the $[Co(bpy)_3]^{3+/2+}$ redox shuttle through reduction of recombination to the oxidized dye. These findings clearly demonstrate the fine balance between the regeneration and recombination reactions when outersphere redox shuttles are employed in DSSCs. Isolation of the efficiency-limiting reactions, however, allows for strategies to overcome these barriers to be identified.

3.2 Introduction

Dye-sensitized solar cells (DSSCs) have garnered substantial interest since the seminal report in 1991 by O'Regan and Grätzel that demonstrated they are capable of producing high solar power conversion efficiencies with potentially inexpensive materials.[1] The vast majority of subsequent research on DSSCs has utilized the I_3^-/I^- redox shuttle since it long produced the highest efficiencies with a variety of sensitizers and photoanode materials. This good performance is a consequence of slow recombination which allows excellent charge collection even with a high surface area photoanode. Despite the advantages of I_3^-/I^-, it suffers from several well-known drawbacks. Most importantly in terms of device efficiency is the large energy penalty required to achieve efficient dye regeneration. In addition, it is not possible to systematically tune the properties of I_3^-/I^- which would allow general design principles to be established that would lead to a superior redox shuttle. One-electron outersphere redox shuttles are attractive alternatives to I_3^-/I^- as their properties are generally tunable and capable of being utilized in broader systematic investigations. [2–6]

The most promising outersphere redox shuttles examined to date are based on cobalt complexes. The first example was a report in 2001 by Nusbaumer *et al*. who investigated cobalt 2,6-bis(1′-butylbenzimidazol-2′-yl)pyridine as a redox shuttle in DSSCs.[7] Interest in cobalt redox shuttles really exploded following the report in 2010 by Feldt *et al*. on a DSSC with an efficiency of 6.7% under one sun illumination using the cobalt tris-bipyridine, $[Co(bpy)_3]^{3+/2+}$, redox shuttle in combination with an organic dye.[8] This redox shuttle is especially attractive since it is simple to make with commercial ligands, is nonvolatile, noncorrosive, and has minimal competitive light absorption. Follow up work on optimizing the sensitizer and electrolyte has since allowed the $[Co(bpy)_3]^{3+/2+}$ to produce the current highest reported efficiencies for a DSSC of 13%.[9,10]

Since it is possible to tune the potential of this motif of redox shuttle through modification of the ligands, it is amenable to systematic study to obtain more detailed understanding of the structure-function relationship which is expected to lead to even further optimization. The cobalt complexes of interest are one-electron outersphere redox shuttles, therefore their behavior should be interpretable using Marcus theory. For example, Feldt *et al*. recently studied the regeneration and recombination kinetics in DSSCs using a series cobalt tris-bipyridine and cobalt bis-phenanthroline redox couples and interpreted their results in terms of Marcus theory. Interestingly, a plot of the regeneration half times vs. driving force plateaued at a driving force of ~0.6 eV to a value of $\sim 10^5$ s^{-1} which they interpreted as an indication of the inverted region.[11] There are many explanations for such rates to plateau,[12] however, with the most likely being diffusion limited reaction. Indeed, diffusion limited regeneration was demonstrated in a related study by Daeneke et al. using a series of ferrocene derivatives, however with an apparent diffusion limited rate constant about an order of magnitude larger that observed for the cobalt complexes.[6] Cobalt polypyridyl complexes are known to have very slow diffusion coefficients in mesoporous TiO_2,[13]

which may account for this discrepancy. While, as the authors noted, the maximum rate constant observed is slower than expected for a diffusion limited reaction, it is orders of magnitude lower than expected for a maximum rate constant ($-\Delta G^0 = \lambda$).[14,15] In addition, the combination of the driving force corresponding to the maximum regeneration rate with dark current and lifetime measurements of recombination indicate a reorganization energy of only 0.6 eV for these cobalt complexes, which was taken as evidence that both regeneration and recombination reactions occur in the inverted region. This is in disagreement with known low self-exchange rate constants of such cobalt(II) complexes due to large inner sphere reorganization energy,[16] all previous ground state bimolecular solution measurements of electron transfer,[15] measurements of electron transfer rate constants at ideal ZnO single electrodes,[17] and modeling of recombination in DSSCs.[3] Since the regeneration and recombination reactions (in addition to light absorption and diffusion coefficient) dictate the performance of any redox shuttle in a DSSC, it is crucial to fully understand the behavior in a framework that would allow predictive power. Therefore, we believe the interpretation of the behavior of one-electron outersphere redox shuttles in DSSCs in terms of Marcus theory is still an open question which urgently needs to be addressed.

In addition to driving force, the Marcus model also indicates a strong dependence of electron transfer on reorganization energy. To date, there are no reports on the reorganization energy dependence on regeneration, nor any steady-state measurements of regeneration with cobalt-based redox shuttles. In this work we compare the self exchange rate constants, photovoltaic performance, dye regeneration efficiency and electron diffusion length of DSSCs employing the $[Co(bpy)_3]^{3+/2+}$ and cobalt bis(trithiacyclononane), $[Co(ttcn)_2]^{3+/2+}$, redox shuttles.[18] All results were interpreted using the Marcus formalism of electron transfer theory to help form a comprehensive picture of the effect of reorganization energy and driving force of the two key reactions involving a redox

shuttle (regeneration and recombination) on the overall performance of DSSCs employing such one-electron outersphere redox shuttles. The conclusions derived from these results are in stark contrast to previous reports. In addition, Atomic Layer Deposition (ALD) was used to add a single layer of alumina on the TiO_2 film prior to immersing it in the sensitizer solution which is known to improve performance for DSSCs employing these redox shuttles. Interestingly, however, we found the improvement arises from two distinct causes.

3.3 Experimental

3.3.1 Materials

Acetonitrile (anhydrous, Sigma Aldrich) and lithium bis(trifluoromethane)sulfonimide (99.95% trace metals basis, Sigma Aldrich) were stored under inert and moisture free atmosphere and used as received. D35cpdt (95%, Dyenamo) dye and chenodeoxycholic acid (Solaronix) were used as received. The redox couples $[Co(bpy)_3](TFSI)_2$, $[Co(bpy)_3](TFSI)_3$, $[Co(ttcn)_2](TFSI)_2$, and $[Co(ttcn)_2](TFSI)_3$, where bpy is 2,2′-bipyridine, ttcn is 1,4,7-trithiacyclononane and TFSI is bis(trifluoromethane) sulfonimide, were prepared as described previously.[18]

3.3.2 Solar cell preparation

TiO_2 photonanodes and Pt counter electrodes were prepared and sandwiched as described in chapter 2.3.1. For some electrodes, alumina was deposited immediately following removal from the oven by ALD and treated using same procedure outlined in chapter 2.3.1. Highly transparent nanoparticle TiO_2 paste, average particle size ~10-15nm, was used for preparing the TiO_2 film on photoanodes. The film thicknesses, *d*, were measured using a Dektak3 Surface Profiler. Two film thicknesses (7.2 μm and 3.7 μm) were prepared and used in DSSCs described in chapter 3. D35cpdt dye solution consisting of 0.2 mM D35cpdt and 5 mM chenodeoxycholic acid in ethanol was used for dye soaking process. Electrolytes consisting of 0.2 M Co(II), 20 mM Co(III), 0.1 M LiTFSI

and 10 mM Chenodeoxycholic acid in acetonitrile was introduced by capillary force through the two pre-drilled holes on the platinum counter electrode, which were subsequently sealed with microglass and Surlyn film. Note that the holes drilled on the counter electrode were positioned apart from the cell active area to avoid unwanted light loss from the sealing glass when light was illuminated from the counter electrode side.

3.3.3 Sample Cells for Optical Measurements Preparation

Quantitative *in situ* measurements of transmittance of complete dye sensitized solar cells is difficult because most of the light from 400 nm to 600 nm is absorbed by the sensitized TiO_2 films used in the assembled DSSCs (see appendix, figure 3.6). Therefore, additional TiO_2 films of various thicknesses (600 nm, 810 nm, 1.50 µm and 1.80 µm) were prepared by diluting the Solaronix HT/SP TiO_2 paste with α-terpineol and organic binders. Further, to avoid light leakage[19] from the side of the substrate and minimize substrate light absorption, high-quality microglass (VWR Micro Slides, 1.2mm thick) substrates were used instead of FTO glass substrate (see Figure 3.7 in appendix for comparisons of the different substrates). The TiO_2 (HT/SP) film was deposited on the glass substrate using the same method as TiO_2 nanoparticle electrodes described above. The resulting glass substrates with TiO_2 films were then sensitized using same dye solution composition and dye soaking condition described above. The glass substrate with sensitized TiO_2 film was then sandwiched with another 1.2 mm thick high quality microglass using a 25 µm Surlyn film frame in a same manner as the solar cell assembly procedure described above. Electrolyte was induced through predrilled holes in the glass slide. Four sample sandwich cells of each thickness (600 nm, 810 nm, 1.50 µm and 1.80 µm) with each electrolyte ($[Co(bpy)_3]^{3+/2+}$ and $[Co(ttcn)_2]^{3+/2+}$) were assembled, 48 cells were made in total for 12 conditions. Un-sensitized blank control cells were made in parallel with sensitized sample cell series conditions used above.

3.3.4 Current-Voltage Measurements

Photoelectrochemical measurements were performed with a potentiostat (Autolab PGSTAT 126N) interfaced with a Xenon Arc Lamp. An AM 1.5 solar filter was used to simulate sunlight at 100 mW cm^{-2} and the light intensity was calibrated with a certified reference cell system (Oriel® Reference Solar Cell & Meter). An additional 400 nm long-pass filter was used to prevent direct excitation of the TiO_2 in all light measurements. A black mask with an aperture area (0.4 × 0.4 cm^2) was applied on top of the cell. Open circuit voltage decay measurements were performed by turning on the light until the voltage stabilized, followed by switching the light off and recording the decay of the voltage. Electrochemical impedance spectroscopy, EIS, measurements were performed in the dark using a FRA2 integrated with the PGSTAT 128N. The impedance spectra were recorded at applied voltages from -0.3 to -0.6 V, stepped in 25 mV increments, with a 10 mV alternating potential superimposed on the direct bias. Each impedance measurement consisted of frequency sweeps from 5×10^{-2} to 1×10^{5} Hz in equally spaced logarithmic steps.

3.3.5 IPCE Measurements

A monochromator (Horiba Jobin Yyon MicroHR) attached to the 450 W Xenon arc light source was used for monchromatic light for IPCE measurements. Both entrance and exit slit width were set to 0.75 mm to meet an 8 nm line width for good resolution IPCEs. The photon flux of the light incident on the samples was measured with a laser power meter (Nova II Ophir). IPCE measurements were made at 10 nm intervals between 400 nm and 750 nm at short circuit in the absence of bias light. The cells were illuminated from either the TiO_2 photoanode side or the Pt counter electrode side.

3.3.6 Optical Measurements

Optical transmission and reflectance measurements were performed using a Perkin-Elmer Lambda 35 UV-vis spectrometer with a Labsphere integrating sphere. Measurements of sample cells and blank cells were taken and the absorbance of dye-sensitized TiO_2 films (A_D) of various film thicknesses were calculated through the following equation (1) which is adapted from thin film absorbance measurements:[20]

$$A_D = -\lg\left(\frac{T_B \times T_D}{T_B{}^2 - (R_D - R_B)T_E{}^2}\right) = \frac{-\alpha_{dye} \times d}{\ln 10} \quad (1)$$

Here T_B and R_B are the transmittance and reflectance of the unsensitized blank cell, T_D and R_D are the transmittance and reflectance of the sensitized sample cell. This equation applies when competitive absorption from the electrolyte is minimal compared to absorption from sensitized film. Because there is negligible absorption from the TiO_2 film and glass substrate employed in the visible light region, the blank sample cell thus can be simplified as an integrated substrate without any solid liquid interface, and the sensitized sample can be considered as adding one layer of strongly light absorbing thin film layer to the blank. In this way, measuring the dyed film absorbance can be simplified to a two-layer thin film model while taking into account the overall reflection and scattered light of the complicated sandwiched sample cell system. Detailed derivation of the equation is included in the appendix. The sensitized film absorbance was used to make a plot of A_D vs. d; a straight line was fit to the plot and the absorptivity of sensitized film was determined from the fitted slope (see figures 3.10 - 3.14 in the appendix,). This procedure assumes dye loading is homogeneous throughout the TiO_2 film. The electrolyte solution absorbance was also measured to determine the electrolyte absorptivity (see figure 3.15 in the appendix), α_e. A porosity, $P = 0.7$, was used to account for light absorption by the electrolyte filled in the pores. Transmittance and reflectance of FTO with TiO_2 blocking layer (T_{FTO}, R_{FTO}) and

platinized FTO (T_{Pt}, R_{Pt}) were measured with incident light illuminated through the FTO nonconductive side (see figure 3.8 in the appendix).

3.4 Results

*3.4.1 Self-Exchange Rate Constants**

Table 3.1 Summary of self-exchange rate constants, k_{11}, k_{22}, and k_{33}, and the corresponding reduction potentials, E°, for $[Fe(C_5H_4CH_3)_2]^{+/0}$, $[Co(bpy)_3]^{3+/2+}$ and $[Co(ttcn)_2]^{3+/2+}$ in acetonitrile with 0.1 M LiTFSI at 25 ± 0.4°C.

x	Redox Couple	E° (mV vs. Fc)	k_{xx} ($M^{-1}s^{-1}$)
1	$[Fe(C_5H_4CH_3)_2]^{+/0}$	- 114 ± 5	$(8.3 \pm 0.8) \times 10^6$
2	$[Co(bpy)_3]^{3+/2+}$	- 51 ± 2	0.27 ± 0.06
3	$[Co(ttcn)_2]^{3+/2+}$	3 ± 3	$(9.1 \pm 0.7) \times 10^3$

3.4.2 Solar Cell Measurements

Figure 3.1a shows plots of typical current density (*J*) vs. applied voltage (*V*) curves of DSSCs employing $[Co(bpy)_3]^{3+/2+}$ and $[Co(ttcn)_2]^{3+/2+}$ redox shuttles under simulated 1 sun illumination from the front side (FS) and back side (BS) directions. Front side refers to the TiO_2 substrate and back refers to the counter electrode / electrolyte. The average short circuit photocurrent density (J_{sc}), open circuit photovoltage (V_{oc}) and fill factors (*ff*) derived from the *J-V* curves of 12 cells are given in Table 3.2. We note that the V_{oc} is smaller than literature reports on optimized devices.[11]This is largely due to the differences in electrolytes, since we omitted 4-*tert*-butylpyridine, which is well known to increase the V_{oc} in DSSCs,[21] in order to have a reliable value for the conduction band energy and ensure quantitative injection as discussed in detail below. *J-V* curves of DSSCs with and without 4-tert-butylpyridine in the electrolyte are displayed in the supporting information to demonstrate this effect (See figure 3.24 in appendix). Under FS illumination, the J_{sc}'s, V_{oc}'s and *ff*'s of the $[Co(bpy)_3]^{3+/2+}$ cells were comparable to the

$[Co(ttcn)_2]^{3+/2+}$ cells. The overall performance of the cells under BS illumination was worse, with a significant difference between the cells with the two redox shuttles. While the BS J_{sc} decreased by ~70 % compared to FS illumination for the $[Co(bpy)_3]^{3+/2}$ cells, the J_{sc} for the $[Co(ttcn)_2]^{3+/2+}$ cells decreased by ~90%. The reduced photocurrent under BS illumination is likely due to lower charge collection efficiencies resulting from electron diffusion lengths shorter than the film thickness.[22] Figure 3.1b shows the average incident photon to current efficiency (IPCE) derived from eight cells containing the two different electrolytes under FS and BS illumination, with error bars representing the standard deviation. The IPCE values exhibit the same trends, and the integrated IPCE produce J_{sc} values agree with the measured J_{sc}, indicating they contain the information relevant to the *J-V* behavior as expected. The observed agreement between presumably low intensity IPCE and high intensity JV measurements suggests that the diffusion length is not strongly dependent on electron density, consistent with recombination predominantly via the conduction band.

Table 3.2 Average *J-V* characteristics of twelve DSSCs under simulated AM 1.5G illumination (100 mW cm^{-2})

Redox shuttle	$[Co(bpy)_3]^{3+/2+}$		$[Co(ttcn)_2]^{3+/2+}$	
Illumination Direction	Front side	Back Side	Front side	Back Side
η (%)	1.64 ± 0.10	0.45 ± 0.14	1.55 ± 0.17	0.05 ± 0.00
J_{sc} (mA cm^{-2})	4.64 ± 0.41	1.19 ± 0.55	4.62 ± 0.59	0.22 ± 0.23
V_{oc} (V)	0.53 ± 0.01	0.50 ± 0.01	0.48 ± 0.05	0.48 ± 0.02
FF	0.66 ± 0.04	0.76 ± 0.04	0.69 ± 0.05	0.66 ± 0.02

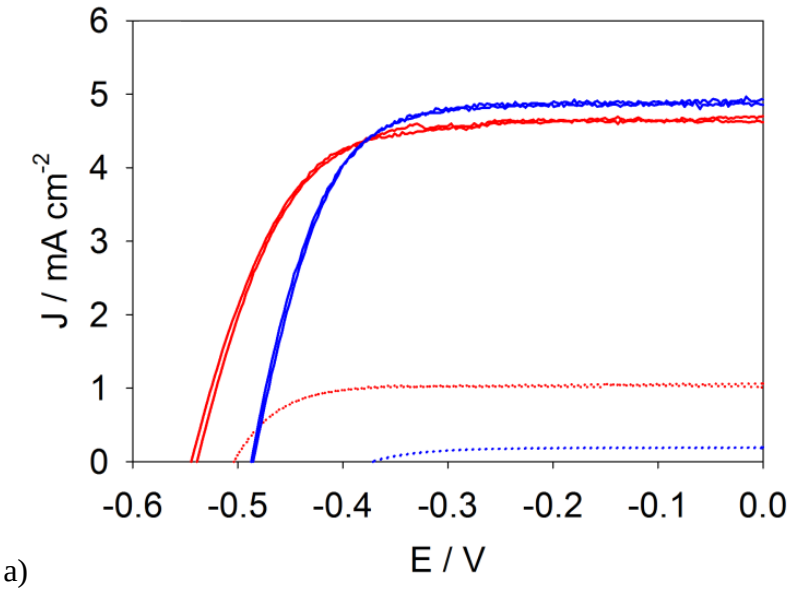

a)

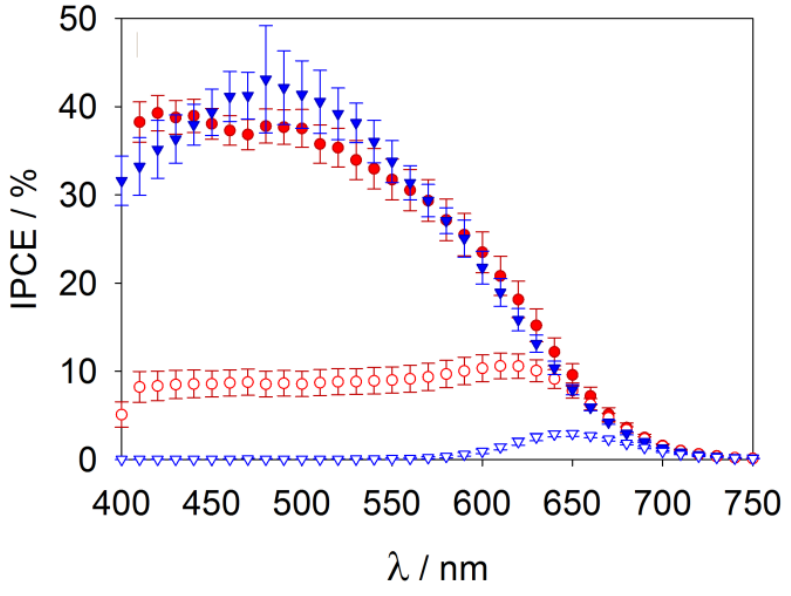

b)

Figure 3.1 a) Plots of representative *J-V* curves of DSSCs with the $[Co(bpy)_3]^{3+/2+}$ (red) and $[Co(ttcn)_2]^{3+/2+}$ (blue) redox shuttles for FS (solid) and BS (dotted) illumination directions. b) IPCE curves of DSSCs with the $[Co(bpy)_3]^{3+/2+}$ (red circles) and $[Co(ttcn)_2]^{3+/2+}$ (blue triangles) redox shuttles for FS (filled) and BS (hollow) illumination directions; film thickness, 7.1 μm.

The IPCE can generally be described by the product of the light harvesting efficiency, η_{LH}, the electron injection efficiency, η_{inj}, the dye regeneration efficiency, η_{reg}, and the charge collection efficiency η_{cc}:

$$IPCE(\lambda) = \eta_{LH}(\lambda)\eta_{cc}(\lambda)\eta_{Inj}(\lambda)\eta_{reg}(\lambda) \quad (2)$$

Figure 3.2 shows the light harvesting efficiency for both FS and BS illumination directions, determined from the photogeneration profiles as described in detail in the SI. The cells absorb strongly up to 600 nm; the η_{LH} of BS illumination is slightly attenuated by the platinized counter electrode and the electrolyte layer between counter electrode and TiO_2 film, however there is no obvious difference between FS and BS illumination for at $\lambda > 600$ nm. Differences in light harvesting efficiency cannot explain the difference in IPCEs for the different illumination directions. In addition, the light harvesting efficiency is essentially the same for the two redox shuttles as show in Figure 3.2 and thus cannot account for the difference in their IPCE curves either.

Assuming that η_{inj} and η_{reg} are position independent, they cancel out by taking the BS/FS ratio of the IPCEs, which leaves the product of charge collection efficiency ratio and light harvesting efficiency ratio. The optical parameters that determine the light harvesting efficiency ratio are measured independently and shown in Figure 3.2. Therefore, the light harvesting normalized IPCE ratio is just the ratio of charge collection efficiencies, which is a function of the electron diffusion length, L_{n}, and film thickness, d, as well as a function of absorption coefficient (and thus wavelength) through the carrier generation profile. The film thickness is also determined independently via profilometry. Thus, L_{n} can be derived from fitting the ratio of IPCE spectra for BS and FS illumination, which is given by:[23–25]

$$\frac{IPCE(BS)}{IPCE(FS)} = \frac{T_{pt}T_e[-(L_n(\alpha_{dye}+\alpha_e)+1)e^{2d/L_n} + 2L_n(\alpha_{dye}+\alpha_e)e^{d(\alpha_{dye}+\alpha_e)+(1/L_n))} - L_n(\alpha_{dye}+\alpha_e)+1]}{(L_n(\alpha_{dye}+\alpha_e)-1)e^{d(\alpha_{dye}+\alpha_e)+(2/L_n))} + (L_n(\alpha_{dye}+\alpha_e)+1)e^{d(\alpha_{dye}+\alpha_e)} - 2L_n(\alpha_{dye}+\alpha_e)e^{d/L_n}}$$

(3)

Plots of T_{Pt}, T_e, α_{dye} and α_e are provided in the supporting information. IPCE(BS) / IPCE(FS) spectra were fitted with L_n as the only free-fitting parameter using a nonlinear least-squares method. The IPCE(BS) values for the cells containing $[Co(ttcn)_2]^{3+/2+}$ with a 7.1 µm TiO_2 film were too low to get a meaningful fit from the IPCE ratio, see figure 3.17 in the appendix. Therefore, additional sets of cells were prepared with a TiO_2 thickness of 3.7 µm which exhibited larger IPCE(BS), see figure 3.18 in the appendix. Figure 4 shows the BS/FS IPCE ratios for DSSCs employing $[Co(bpy)_3]^{3+/2+}$ (7.1 µm thick TiO_2) and $[Co(ttcn)_2]^{3+/2+}$ (3.7 µm thick TiO_2) redox shuttles, as well as the results from fitting to equation (3). From these fits, the electron diffusion length is found to be ~3.3 µm for $[Co(bpy)_3]^{3+/2+}$ and ~1.3 µm for $[Co(ttcn)_2]^{3+/2+}$. The electron diffusion length result agrees well with a recent literature reported value of 2.8 µm for $[Co(bpy)_3]^{3+/2+}$.[26]

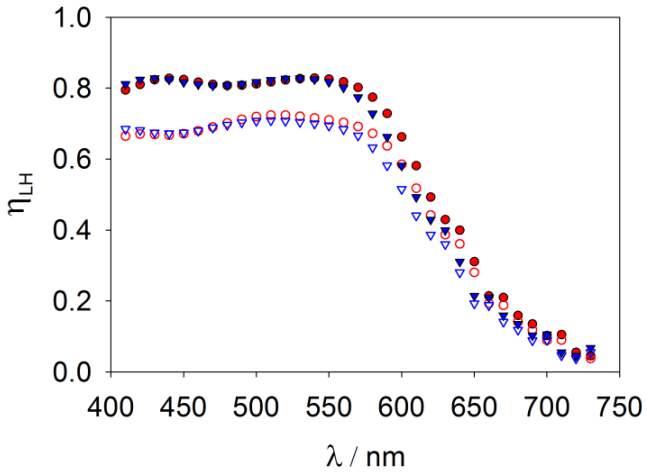

Figure 3.2 Light harvesting efficiency (η_{LH}) of 7.1µm thick TiO_2 film in DSSCs with the $[Co(bpy)_3]^{3+/2+}$ (red) and $[Co(ttcn)_2]^{3+/2+}$ (blue) redox shuttles, Front side illumination (filled), Back side illumination (hollow).

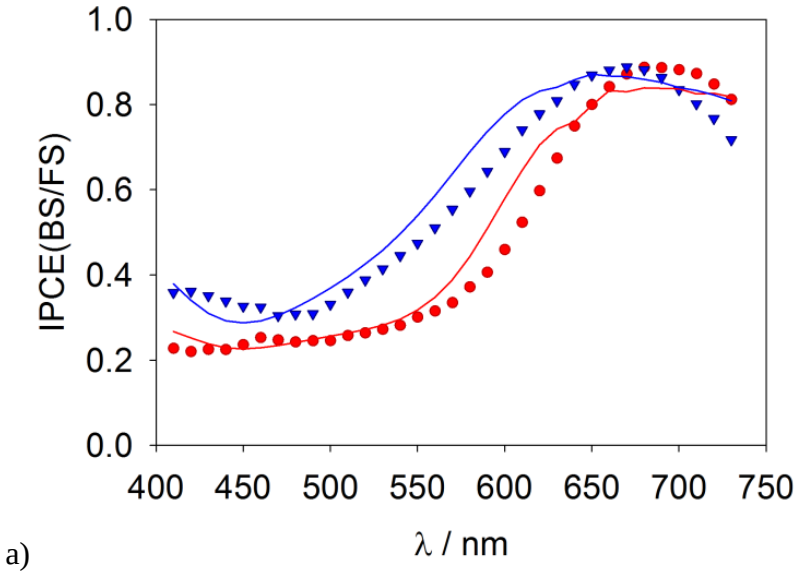

a)

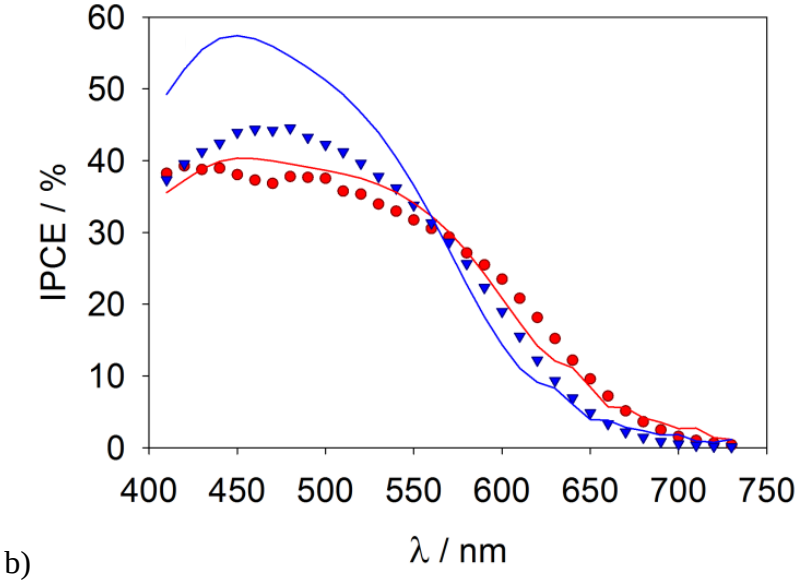

b)

Figure 3.3 Experiment (shape) and fit (line) results of a) IPCE(BS/FS) ratios and b) IPCEs for DSSCs employing the $[Co(bpy)_3]^{3+/2+}$ (red circle) and $[Co(ttcn)_2]^{3+/2+}$ (blue triangle) redox shuttles.

Once the value of L_n is known, the IPCE, either FS or BS, can be fit to extract values for $\eta_{inj} \times \eta_{reg}$. For example, the IPCE(FS) is given by equation (4):

$$IPCE(F) = \frac{(1-R)L_n\eta_{inj}\eta_{reg}\alpha_{dye}e^{-d(\alpha_{dye}+\alpha_e)}(L_n(\alpha_{dye}+\alpha_e)-1)e^{d(\alpha_{dye}+\alpha_e)+(2/L_n))} + (L_n(\alpha_{dye}+\alpha_e)+1)e^{d(\alpha_{dye}+\alpha_e)} - 2L_n(\alpha_{dye}+\alpha_e)e^{d/L_n}}{[L_n^2(\alpha_{dye}+\alpha_e)^2-1)](e^{2d/L_n}+1)}$$

(4)

with only the product of η_{inj} and η_{reg} as a single fitting parameter. Using this approach, the product $\eta_{inj} \times \eta_{reg}$ is ~0.54 for $[Co(bpy)_3]^{3+/2+}$ and ~1 for $[Co(ttcn)_2]^{3+/2+}$. Since the same sensitizer and electrolyte, except for identity of redox shuttle, is used in both systems, the electron injection efficiency is taken to be identical. Therefore, the difference in $\eta_{inj} \times \eta_{reg}$ for the two redox shuttles can be attributed to only differences in dye regeneration efficiency; the regeneration efficiency for $[Co(bpy)_3]^{3+/2+}$ is ~0.54. Thus, the $[Co(ttcn)_2]^{3+/2+}$ redox shuttle is limited by fast recombination, which diminishes the charge collection efficiency, while the $[Co(bpy)_3]^{3+/2+}$ redox shuttle is limited by slow dye regeneration. This result is consistent with the very different self-exchange rate constants of the two redox shuttles determined above and as discussed in more detail below.

3.4.3 Effect of alumina layer

The deposition of insulating blocking layers on the TiO_2 surface has been demonstrated to be an effective means of reducing the rate of back electron transfer to the oxidized redox shuttle in order to increase the electron diffusion length and overall efficiency of DSSCs employing outersphere redox shuttles.[2,27,28] We note that a blocking layer on the TiO_2 surface should likewise slow the rate of recombination to the oxidized dye. Since the regeneration efficiency is determined by the kinetic competition of dye reduction by the reduced form of the redox shuttle and electrons in TiO_2, slowing down back electron transfer from TiO_2 should also improve the regeneration efficiency. Thus, the addition of a blocking layer should improve the performance of $[Co(ttcn)_2]^{3+/2+}$ and $[Co(bpy)_3]^{3+/2+}$, however for different reasons. In order to test these ideas, we applied one ALD cycle of alumina on the TiO_2 substrate prior to immersing it in the sensitizer

solution. Figure 3.4 shows the FS and BS IPCEs of DSSCs employing the $[Co(bpy)_3]^{3+/2+}$ (7.1 µm thick TiO_2) and $[Co(ttcn)_2]^{3+/2+}$ (7.1 µm thick TiO_2) redox shuttles with the addition of 1 ALD cycle of alumina.

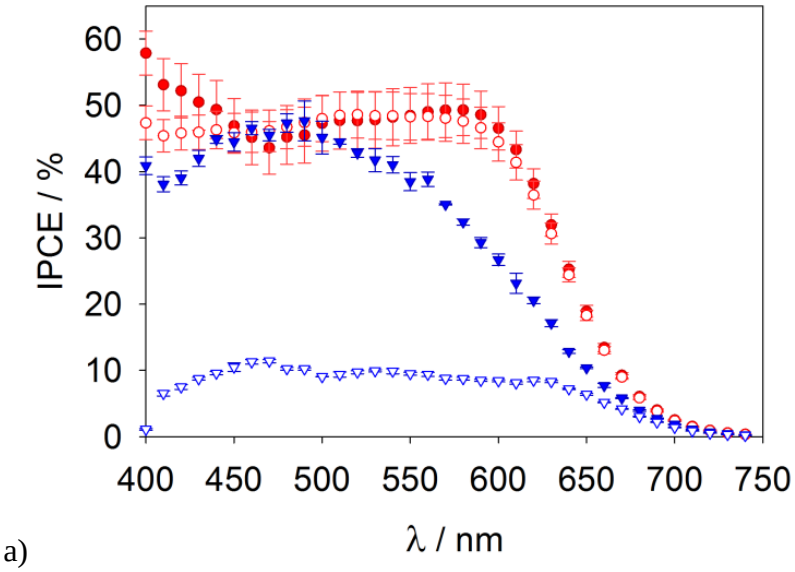

a)

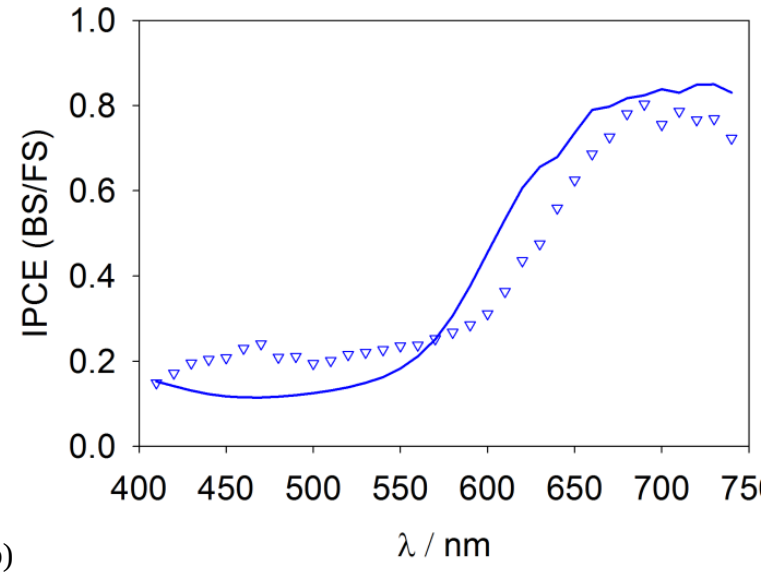

b)

Figure 3.4 a) IPCE curves of DSSCs with 1 ALD cycle of Al_2O_3 employing the $[Co(bpy)_3]^{3+/2+}$ (red) and $[Co(ttcn)_2]^{3+/2+}$ (blue) redox shuttles, Front side illumination (filled), Back side illumination (hollow). b) IPCE ratio (symbols) and fit results (line) to equation (11) for DSSC with 1 ALD cycle Al_2O_3 coating employing the $[Co(ttcn)_2]^{3+/2+}$ redox shuttle.

The FS and BS IPCE's for $[Co(bpy)_3]^{3+/2+}$ are nominally identical, which indicates that $L_n > d$ and a good fit for a value of L_n is not feasible. In this case, assuming that the η_{cc} is unity, the product of $\eta_{inj} \times \eta_{reg}$ can be extracted simply by dividing the IPCE by the η_{LH}. This results in a value of ~0.7 for $\eta_{inj} \times \eta_{reg}$. (see figure 3.21 in the appendix) The FS and BS IPCEs are sufficiently different with the $[Co(ttcn)_2]^{3+/2+}$ redox shuttle, however, to allow for an accurate fit of the IPCE ratio. This fit produced a value of ~2.5 μm for $[Co(ttcn)_2]^{3+/2+}$. Fitting the IPCEs with this value of L_n produced a value of ~0.7 for $\eta_{inj} \times \eta_{reg}$. A summary of all fit values for above DSSCs conditions are given in Table 3.3.

Table 3.3 Fit values of L_n and $\eta_{inj} \times \eta_{reg}$ for DSSCs employing $[Co(bpy)_3]^{3+/2+}$ and $[Co(ttcn)_2]^{3+/2+}$ redox shuttles for with and without 1 ALD cycle of alumina as a blocking layer. Also shown is the driving force of regeneration, $-\Delta G^0_{reg}$, for the two redox shuttles.

Redox shuttle	ALD Cycles	L_n / μm	$\eta_{inj} \times \eta_{reg}$	$-\Delta G^0_{reg}$ (eV)
$[Co(bpy)_3]^{3+/2+}$	0	3.25 ± 0.16	0.54 ± 0.03	0.506
	1		0.74 ± 0.04	
$[Co(ttcn)_2]^{3+/2+}$	0	1.30 ± 0.05	1.00 ± 0.05	0.452
	1	2.45 ± 0.04	0.72 ± 0.01	

Figure 6 shows electron lifetimes plotted as a function of cell voltage which were determined from open circuit photovoltage decay measurements.[29] Electrochemical impedance spectroscopy measurements were also performed which produced similar values of τ_n, and verified that the conduction band and electron concentration was constant through comparisons of the capacitance as shown previously (see Figure 3.22 in the appendix).[27] Through a global fit of the lifetimes with a fixed slope, which was done to avoid bias by choosing an arbitrary voltage, the electron lifetime was found increased by a factor of 8.6 ± 1.1 for both redox shuttles with an alumina layer compared to unmodified electrodes. Further, DSSCs containing $[Co(bpy)_3]^{3+/2+}$ exhibited a 10 times longer

lifetime compared to DSSCs containing $[Co(ttcn)_2]^{3+/2+}$ for both modified and unmodified TiO_2 electrodes.

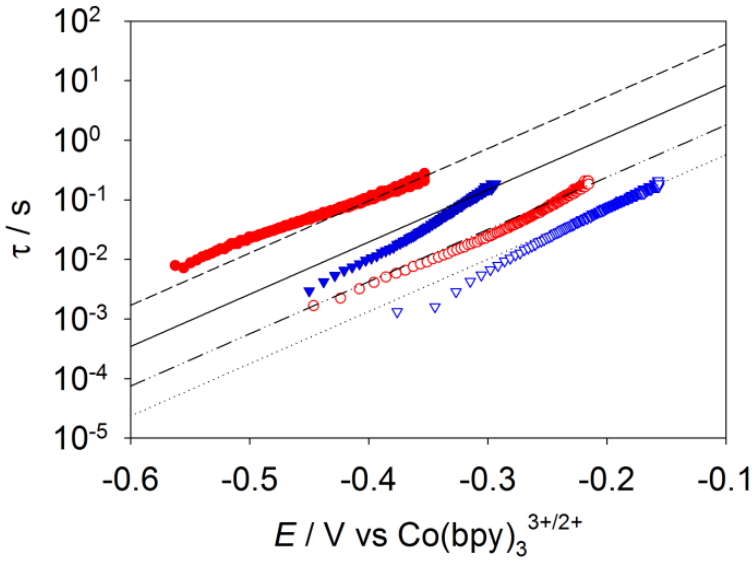

Figure 3.5 a) Lifetimes vs. applied voltage (symbols) and global fit (lines) of DSSCs used for IPCE ratio fits, $[Co(bpy)_3]^{3+/2+}$ (red) and $[Co(ttcn)_2]^{3+/2+}$ (blue) redox shuttles, with 1 ALD cycle Al_2O_3 coating (filled), without Al_2O_3 coating (hollow). b) IPCE ratio (symbols) and fit results (line) to equation (3) for DSSC with 1 ALD cycle Al_2O_3 coating employing the $[Co(ttcn)_2]^{3+/2+}$ redox shuttle.

3.5 Discussion

3.5.1 Regeneration

The regeneration efficiency is determined by the branching ratio of dye regeneration and recombination as given by:

$$\eta_{reg} \cong \frac{[R]k_{reg}}{[R]k_{reg} + n_s k_{rec}} \tag{5}$$

where $[R]$ is the concentration of the reduced form of the redox shuttle, n_s is the surface electron concentration in TiO_2, k_{reg} is the dye regeneration rate constant and k_{rec} is a rate constant reflecting recombination from TiO_2 to the oxidized dye.[30] The concentration of the electrolytes are the same,

thus [*R*] is constant. As a first order approximation, we assume that n_s is also constant for the two redox shuttles at short circuit under low light intensity, i.e. the conditions of the IPCE measurements. This simplification allows for elucidating the observed effect on regeneration by changing redox shuttle for a given dye or altering the photoanode with alumina. Since the redox shuttles investigated herein are one-electron outersphere redox couples, the rate constant for dye regeneration can be described using the Marcus cross relation, equation (6) below.[14]

$$k_{12} = \left(k_{11}k_{22}K_{12}f_{12}\right)^{1/2} W_{12} \tag{6}$$

According to equation (6), the cross-exchange rate constant is a function of the corresponding self-exchange rate constants, k_{11} and k_{22}, of the acceptor (dye) and donor species (redox couples), the equilibrium constant, K_{12}, for the forward electron-transfer reaction, a non-linear correction term, f_{12}, and an electrostatic work term, W_{12}, related to bringing the reactants into contact. The self-exchange rate constant for the D35cpdt or related dyes attached to the TiO_2 surface is not known, however it is independent of redox shuttle and therefore cancels out when taking the ratio of rate constants. The correction term, *f*, and work term, *W*, are also expected to be the same for the two redox couples which have a similar size and same charge. Therefore, the relative rates of regeneration can be determined by taking the ratio of the redox shuttle self exchange rate constants and equilibrium constants:

$$\frac{k_{reg,ttcn}}{k_{reg,bpy}} = \frac{\sqrt{k_{33}K_{D/ttcn}}}{\sqrt{k_{22}K_{D/bpy}}} \tag{7}$$

where $K_{D/ttcn}$ and $K_{D/bpy}$ are the equilibrium constants for the dye (*D*) regeneration reactions with $[Co(ttcn)_2]^{3+/2+}$ and $[Co(bpy)_3]^{3+/2+}$, respectively. The equilibrium constants are determined from the potential difference of the dye and redox shuttles according to equation (8).

$$nF\Delta E = RT \ln K_{12} \tag{8}$$

where n is the number of electrons transferred (n = 1), F is Faraday's constant, ΔE is the formal potential difference between the oxidant and reductant in solution, R is the gas constant and T is the temperature. The ground state potential of the dye adsorbed on the nanoparticle film was determined to be 1.08 V vs. NHE by cyclic voltammetry (see figure 3.23 in the appendix) and it is in agreement with literature reported value,[26] resulting a regeneration driving force of 0.506 eV and 0.452 eV for $[Co(bpy)_3]^{3+/2+}$ and $[Co(ttcn)_2]^{3+/2+}$ respectively. Based on differences in self-exchange rate constants and equilibrium constants, the regeneration rate constant with $[Co(ttcn)_2]^{2+}$ is expected to be 57 times larger than $[Co(bpy)_3]^{2+}$, despite the 54 mV smaller driving force. Given that the rate of recombination to the oxidized dye is constant, this increase in regeneration rate constant corresponds to an increase in regeneration efficiency from 0.54 to 0.99, in good agreement with our results.

Addition of the alumina blocking layer was shown to reduce the rate of recombination to the oxidized redox shuttle by a factor of 8.6 ± 1.1, as it presents essentially a tunneling barrier layer for electrons to transfer from TiO_2 to solution. Since the alumina layer is also between the TiO_2 and dye, it should also slow recombination to the oxidized dye by a comparable amount. The addition of a barrier layer should not affect the rate of dye regeneration, however. Therefore, assuming the rate constant of recombination to the oxidized dye is reduced by a factor of 8.6 ± 1.1 upon the addition of an alumina layer, and a constant rate of regeneration, the regeneration efficiency for $[Co(bpy)_3]^{3+/2+}$ would increase from 0.54 to 0.91. The product of $\eta_{inj} \times \eta_{reg}$ for DSSCs with an alumina layer and the $[Co(bpy)_3]^{3+/2+}$ redox shuttle was found to be ~0.7, however. These results suggest that the injection efficiency is diminished.

Since regeneration with $[Co(ttcn)_2]^{3+/2+}$ is quantitative, slowing down recombination to the oxidized dye with the addition of an alumina blocking layer cannot increase the regeneration

efficiency. We note that it is also not reasonable to expect the alumina layer to decrease the regeneration efficiency, since the dye contacting the solution and redox shuttle are unaltered. Because the Al_2O_3 blocking layer is between the TiO_2 nanoparticle and the dye, however, it should reduce the rate of charge injection as it weakens the electronic coupling between the dye and TiO_2 surface.[31,32] Therefore, the decrease in $\eta_{inj} \times \eta_{reg}$ to ~0.7 for DSSCs with an alumina layer and the $[Co(ttcn)_2]^{3+/2+}$ redox shuttle is attributed to a decrease in injection efficiency. This assignment is consistent with both redox shuttles, which should both produce quantitative regeneration (with an alumina layer), but D35cpdt only injects through the alumina barrier layer with an efficiency of 0.7.

The excited state lifetime of the D35 dye co-absorbed with chenodeoxycholic acid on TiO_2 and ZrO_2 surfaces from time resolved fluorescence measurements are reported to be τ_{TiO_2} ~ 0.15 ns and τ_{ZrO_2} ~ 1.42 ns. Since the conduction band of ZrO_2 is too high for electron injection by the excited dye, the injection efficiency can be determined via $\eta_{inj} \approx 1 - \tau_{TiO_2} / \tau_{ZrO_2}$ which produces ~90% injection efficiency.[33] Because D35 and D35cpdt dyes have the same donor and anchoring groups, they have similar LUMO levels (E_{LUMO}(D35) = -1.21V vs. NHE[34] and E_{LUMO}(D35cpdt) = -1.17 V vs. NHE[35]) situated on the cyanoacetic acid unit that binds to the TiO_2 surface. The similar driving forces and electronic couplings between the two dyes should result in negligible differences in rates of electron injection with the two dyes. Therefore, assuming the electron injection rate is also slowed down by a factor of 8.6 ± 1.1 upon the addition of an alumina barrier layer, with a constant rate of competitive decay processes, the injection yield would decrease from 90% to 51%. Relatively small differences in cell preparation can affect the band edge positions and therefore rate of injection, which can account for quantitative injection found here compared to the 90 % injection efficiency reported previously.[33] In addition, the tunneling barrier height of

injection should be somewhat smaller than for recombination since the electrons are higher in energy, which should result in a smaller attenuation of injection compared to recombination with the addition of the alumina layer. Some combination of these factors can readily account for the differences in injection efficiency from 100–70% found here, compared to the 90–51% predicted from literature values. In any case, the quantitative injection for D35cpdt on a bare TiO_2 electrode and the 30% reduction in injection efficiency with an alumina barrier layer reported herein is in good general agreement with previous literature results. Finally we note that the large effect of decreasing the injection efficiency with an Al_2O_3 blocking layer found here differs from previous reports using inorganic Ru-based dyes, since the latter exhibits longer excited state lifetimes of ~20 ns.[24,36]

Finally, we note that when $[Co(bpy)_3]^{3+/2+}$ used with the very similar D35 dye, it was found that a driving force of 0.39 eV produced a regeneration efficiency of 91 %, which is higher than observed here.[37] The regeneration efficiency in that work was determined with transient absorption (TA) measurements on sensitized photoanodes in contact with electrolyte solutions instead of complete devices. The importance of using complete devices to make accurate measurements of regeneration has been addressed by Barnes and coworkers.[38] Jennings and Li, *et al.* also characterized dye regeneration and dye recombination kinetics for the iodide/triiodide redox shuttle in complete DSSCs by TA, IPCE and impedance spectroscopy measurements over a range of background light intensities at open circuit. They found that the regeneration efficiency measured from an incomplete cell system is an overestimation.[39,40] Thus, the differences between our reported regeneration efficiencies and prior reports of this system can be attributed to the different measurement conditions.

3.5.2 Recombination

The charge collection efficiency is a function of diffusion length and thus the electron lifetime. The electron lifetime can be expressed as the ratio of surface electron concentration (at a given potential) to the rate at which they are being lost, i.e. the rate of recombination, *U*. Under the assumption that the rate of recombination is dominated by electron transfer from the conduction band to the oxidized form of the redox shuttle, Co(III), it can be described by the second order rate equation:

$$U = [Co(III)] n_s k_{et} \tag{9}$$

where k_{et} is the electron transfer (recombination) rate constant. The rate constant can be described with Marcus theory using the following equation:[17]

$$k_{et} = k_{et,\max} e^{-\left(\Delta G^0 + \lambda_{et}\right)^2 / 4\lambda_{et} k_B T} \tag{10}$$

where $-\Delta G^0$ is the driving force of the electron transfer and λ_{et} is the reorganization energy associated with the electron transfer. The prefactor, $k_{et,max}$, is the rate constant at optimal exoergicity, obtained when $-\Delta G^0 = \lambda_{et}$, which has been shown to have a value of $10^{-17} - 10^{-16}$ cm^4 s^{-1}. In addition, $k_{et,\,max}$ has a weak dependence on the reorganization energy ($k_{et,max} \propto \lambda_{et}^{-1/2}$). The driving force is the difference between the conduction band energy, $\mathbf{E}_{cb}$, and the formal potential of the redox shuttle. Ondersma et al. used variable temperature spectroelectrochemistry to measure $\mathbf{E}_{cb}$ for TiO_2 in a comparable electrolyte (Li^+ in acetonitrile) with a value of approximately -0.8 V vs Ag/AgCl.[3] Thus, the driving force of recombination to $[Co(bpy)_3]^{3+}$ and $[Co(ttcn)_2]^{3+}$ is -1.106 eV and -1.165 eV, respectively.

The reorganization energy of recombination can be derived from results of the self-exchange rate constants, k_{22} and k_{33}, described above. The total reorganization energy, λ_{22} or λ_{33}, for the

$[Co(bpy)_3]^{3+/2+}$ and $[Co(ttcn)_2]^{3+/2+}$ self-exchange reactions can be calculated using the relationship shown in equation (11).[41]

$$k_{22} = \nu_n e^{-\lambda_{22}/4k_BT} \tag{11}$$

where ν_n is the frequency factor.[14] The value for the vibrational frequency term can range from $10^{11} - 10^{13}$ s^{-1} depending on the changes attributed to the outer-sphere (solvent) or inner-sphere (bond length changes) reaction coordinate during electron transfer.[16,17,41] A value of 10^{13} s^{-1} was used as the frequency factor for both $[Co(bpy)_3]^{3+/2+}$ and $[Co(ttcn)_2]^{3+/2+}$ due to the larger inner-sphere contribution to the total reorganization energy, *vide infra*.[17] The total reorganization energies, λ_{22} or λ_{33}, are the sum of both the outer-sphere, λ_o, and inner-sphere reorganization energies, λ_i. The outer-sphere self-exchange reorganization energy can be obtained from the dielectric continuum theory, equation (12),[14]

$$\lambda_o = \frac{(\Delta z q)^2}{4\pi\varepsilon_0}\left(\frac{1}{a} - \frac{1}{R_e}\right)\left(\frac{1}{n_{sol}^2} - \frac{1}{\varepsilon_{sol}}\right) \tag{12}$$

where Δz is the change in charge of the cobalt complex after electron transfer, q is the charge of an electron, ε_o is the permittivity of free space, ε_{sol} is the static dielectric of acetonitrile (36)[42], n_{sol} is the refractive index of acetonitrile (1.3442)[43], a is the radius of the reactant, and R_e is the reactant center-to-center separation distance ($R_e = 2a$). The radii of $[Co(bpy)_3]^{3+/2+}$ and $[Co(ttcn)_2]^{3+/2+}$ were taken to be 6.5 Å and 5 Å, respectively.[17] Using the total reorganization energy calculated from equation (18), and the outer-sphere reorganization energy calculated from equation (19), the inner-sphere reorganization energy was also determined for each complex via subtraction. Results of all reorganization energies are displayed in Table 3.4.

For the recombination reaction, the inner-sphere reorganization energy is half of the value derived from the self-exchange because half as many molecules participate in each electron transfer. The outer-sphere reorganization energy for the acceptor is again calculated using the

dielectric continuum theory, but revised to include the refractive index of anatase TiO_2 (n_{TiO2} = 2.54)[43] and the static dielectric of anatase TiO_2 (ε_{TiO2} = 114):[44,45]

$$\lambda_{o,TiO_2} = \frac{(\Delta zq)^2}{8\pi\varepsilon_0}\left[\frac{1}{a}\left(\frac{1}{n_{sol}^2}-\frac{1}{\varepsilon_{sol}}\right)-\frac{1}{2R_e}\left(\frac{1}{n_{sol}^2}\left(\frac{n_{TiO_2}^2-n_{sol}^2}{n_{TiO_2}^2+n_{sol}^2}\right)-\frac{1}{\varepsilon_{sol}}\left(\frac{\varepsilon_{TiO_2}-\varepsilon_{sol}}{\varepsilon_{TiO_2}+\varepsilon_{sol}}\right)\right)\right] \quad (13)$$

Thus, the total reorganization energy associated with recombination at the TiO_2 interface becomes $\lambda_{et} = \lambda_{o,TiO_2} + \lambda_i/2$. λ_i represents the innersphere reorganization energy for bimolecular self-exhchange reaction, λ_i is divided by 2 in the electron recombination from TiO_2 to Co(III) because only one molecule is involved. Equation (13) represents the outersphere reorganization energy to reduce Co(III) at TiO_2 surface. It is evident that the reorganization energy of $[Co(bpy)_3]^{3+/2+}$ is dominated by the large inner-sphere reorganization energy as expected.[16]

Table 3.4 Summary of the reorganization energies determined for the $[Co(bpy)_3]^{3+/2+}$ and $[Co(ttcn)_2]^{3+/2+}$ redox shuttles, and the parameters used for calculation of k_{et}.

	$[Co(bpy)_3]^{3+/2+}$	$[Co(ttcn)_2]^{3+/2+}$
λ_o (eV)	0.583	0.757
λ_{in} (eV)	2.63	1.38
λ_{22} or λ_{33} (eV)	3.21	2.14
$\lambda_{o,TiO2}$ (eV)	0.417	0.543
λ_{et} (eV)	1.73	1.23
$-\Delta G^0$ (eV)	1.11	1.17
$k_{et,max}$ (cm^4s^{-1})	5.42×10^{-17}	6.41×10^{-17}

Substituting the values of $k_{et,max}$, $-\Delta G^0$, and λ_{et} determined for $[Co(bpy)_3]^{3+/2+}$ and $[Co(ttcn)_2]^{3+/2+}$ into equation (10), allows the rate constants for recombination from the TiO_2 conduction band to be calculated which is 6.02×10^{-18} $cm^4s^{-1}$and 6.14×10^{-17} cm^4s^{-1} for $[Co(bpy)_3]^{3+/2+}$ and $[Co(ttcn)_2]^{3+/2+}$respectively. Since the concentration of the oxidized redox shuttles was kept constant, and assuming that the surface electron concentration is nominally

identical at the same electrode potentials, the relative electron lifetimes of the two redox shuttles can be determined. The rate constant for recombination to $[Co(ttcn)_2]^{3+}$ is 10 times larger than for $[Co(bpy)_3]^{3+}$, corresponding to a 10 times lower electron lifetime for $[Co(ttcn)_2]^{3+}$ compared to $[Co(bpy)_3]^{3+}$. The measured lifetime for $[Co(bpy)_3]^{3+/2+}$, normalized to a constant potential/capacitance, however, is only ~4 times longer than that of $[Co(ttcn)_2]^{3+/2+}$, see Figure 6 and Figure SI17 in SI. Knowledge of differences in recombination rate constants further allows comparisons of the expected electron diffusion length, which is equal to the square root of the product of the electron diffusion coefficient, D_n, and τ_n according to:

$$L_n = \sqrt{D_n \tau_n} \tag{14}$$

Therefore, the electron diffusion length with $[Co(bpy)_3]^{3+/2+}$ is estimated to be ~3.2 times longer than that of $[Co(ttcn)_2]^{3+/2+}$. The electron diffusion length derived from IPCE measurement for $[Co(bpy)_3]^{3+/2+}$ is 3.25 μm, which is ~2.5 times longer than the 1.30 μm derived for $[Co(ttcn)_2]^{3+/2+}$, in the absence of an alumina layer. The results of the electron lifetime measurements and electron diffusion lengths derived from analysis of the IPCE measurements are in good general agreement with the values estimated using Marcus theory applied to heterogeneous electron transfer. Finally, we note that recombination from trap states was ignored in this analysis. Recombination from the conduction band for both redox shuttles is well in the Marcus normal region; under these conditions, recombination from conduction band electrons should dominate contributions from trap states.[3] However, we there will still be a contribution of recombination from trap states, which should participate more in recombination to $[Co(ttcn)_2]^{3+}$ compared to $[Co(bpy)_3]^{3+}$ due to the larger overlap of acceptor states with trap states. This effect may account for the relatively minor

differences between predicted differences of rate constants and measured electron lifetimes and diffusion lengths.

3.6 Conclusions

Cross-exchange rate constant measurements were performed with two redox shuttles to determine their self-exchange rate constants and reorganization energies associated with electron transfer. The self-exchange rate constant of $[Co(ttcn)_2]^{3+/2+}$ is ~10^4 larger than $[Co(bpy)_3]^{3+/2+}$. This can generally be attributed to the fact that $[Co(ttcn)_2]^{2+}$ is low spin d^7 whereas $[Co(bpy)_3]^{2+}$ is high spin d^7, whereas both Co^{3+} complexes are low spin d^6. As a consequence, charge transfer changes the electron occupancy of the antibonding e_g orbitals both cobalt complexes (assuming approximately O_h symmetry) which produces a change in ligand bond length represented as the inner sphere reorganization energy. Indeed, a change of 0.19 Å in Co-N bond length from the reduction of the related $[Co(phen)_3]^{3+}$ to $[Co(phen)_3]^{2+}$ complexes was determined previously by EXAFS measurements. [16]The reduction of $[Co(ttcn)_2]^{3+}$ is expected to have a smaller effect on bond length change since the occupation of the e_g orbitals changes by one electron compared to two for the $[Co(bpy)_3]^{3+}$ or $[Co(phen)_3]^{3+}$, consistent with the faster self-exchange rate constant and lower innersphere reorganization energy determined herein. The faster self-exchange rate constant of $[Co(ttcn)_2]^{3+/2+}$ is consistent with the more efficient dye regeneration. For both redox shuttles, the reorganization energies are much larger (>1 eV) than the driving force for regeneration. The larger reorganization energy of $[Co(bpy)_3]^{3+/2+}$ compared to $[Co(ttcn)_2]^{3+/2+}$ is also consistent with slower recombination and longer diffusion lengths found. We further found that the addition of insulating alumina layer between TiO_2 and the dye is able to improve the electron diffusion length as well as dye regeneration efficiency. For the dye used in this paper, the injection efficiency

was diminished, however this drawback can be surmounted by utilizing a dye with a longer excited state lifetime.

All results reported herein are consistent with the regeneration and recombination reactions involving cobalt redox shuttles, including the low spin Co(II) shuttle, are in the Marcus normal region. This is obviously a very important point in considering design rules of alternative redox shuttles. The key to significantly improving the device efficiency is to minimize the energy required to drive the key forward reactions (injection and regeneration), without compromising the electron diffusion length by increasing recombination. The results herein point to two potential pathways to further improve the efficiency of DSSCs with outersphere redox shuttles. Further hinder recombination to fast redox shuttles such as $[Co(ttcn)_2]^{3+/2+}$ (or ferrocene) which are capable of quantitative dye regeneration with minimal driving force, but are limited by short electron diffusion lengths. The alternative is to utilize a redox shuttle with sufficient electron diffusion length to allow quantitative carrier collection such as $[Co(bpy)_3]^{3+/2+}$, but is limited by inefficient regeneration. As demonstrated herein, both of these strategies can be effectively utilized through modification of the photoanode with a tunneling barrier layer, as it can increase both the dye regeneration efficiency and collection efficiency by slowing recombination to the dye and redox shuttle, respectively. For this to be really effective, however, an energetically matched dye must be identified with a sufficient excited state lifetime to efficiently inject through the barrier layer. Alternatively, as these reactions are in the Marcus normal region, it should be possible to concomitantly increase regeneration and collection with a fast redox shuttle by moving the redox potential to more negative values. For this strategy to be effective, the redox shuttle would also have to be matched to a near-IR absorbing dye with a more negative ground state potential. We believe, however, that such a multi-component optimization will ultimately lead to DSSCs which

exhibit efficiencies competitive with Perovskite and other third generation PVs. The pursuit of this is ongoing in our lab.

APPENDIX

APPENDIX

Optical measurement results

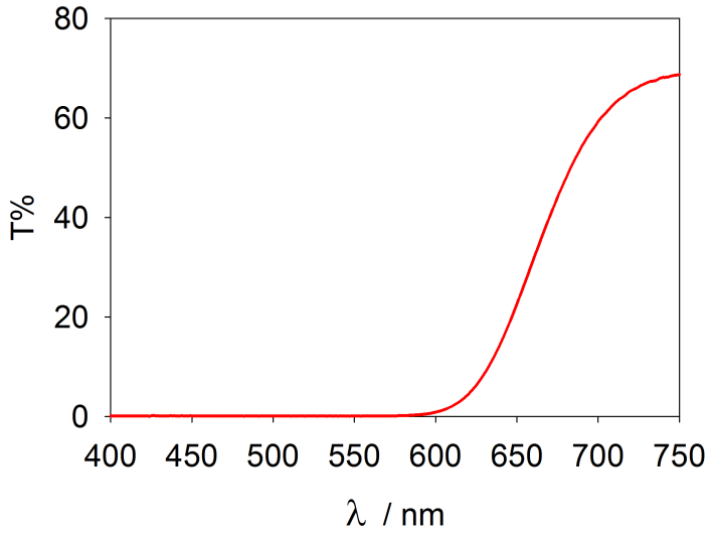

Figure 3.6 Transmittance of dye sensitized solar cell with 7.1μm thick TiO_2 film.

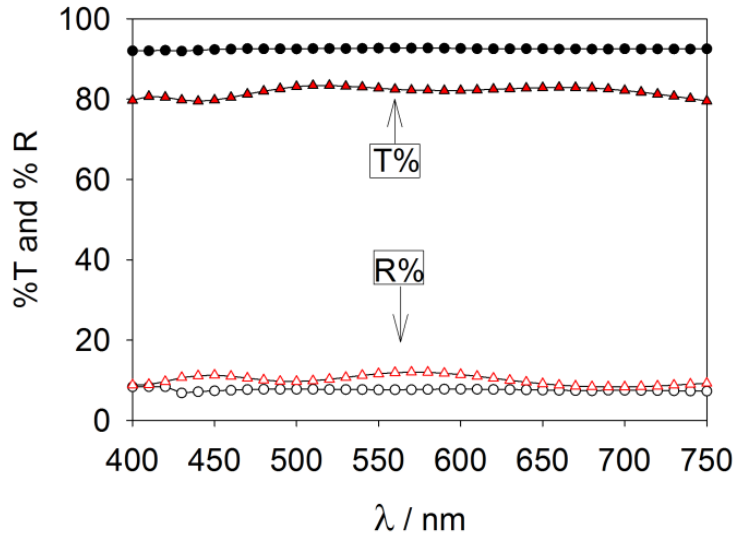

Figure 3.7 Transmittance (T%) (filled) and reflectance (R%) (hollow) of FTO (red triangle) and 1.2 mm high quality glass substrate (black circle).

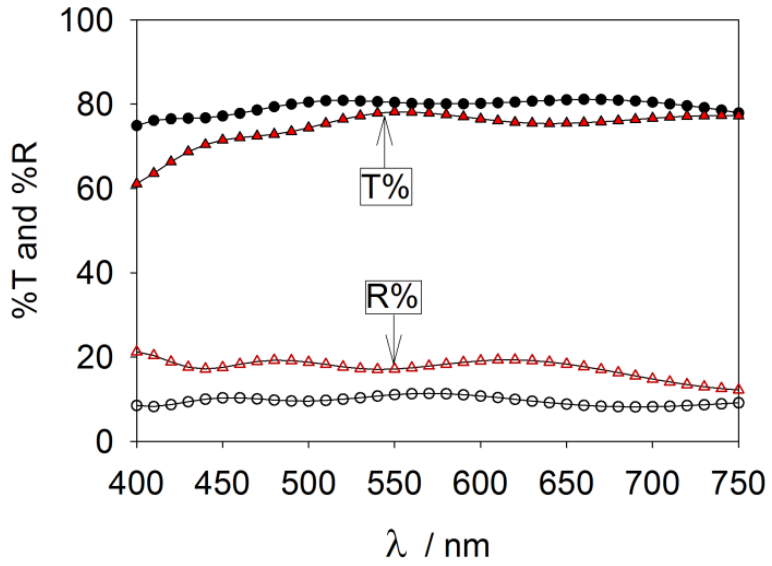

Figure 3.8 Transmittance (T%) (filled) and reflectance (R%) (hollow) of DSSC photoanode substrate - FTO with TiO_2 ALD blocking layer (black circle) and counter electrode - platinized FTO (red triangle).

Figure 3.8 shows the transmittance (T%) and reflectance (R%) of photoanode substrate and platinized counter electrode. T = 77% - 82% at λ =450 -750nm for photoanode substrate, but ca. 4 -5 % units lower for the counter electrode, due to mainly the light absorption by the platinum catalyst layer. R = 10% - 12% at λ =450 -750nm for photoanode substrate, and ca. 5% -10% units higher for the counter electrode, due to mainly the roughness induced by the platinum catalyst layer.

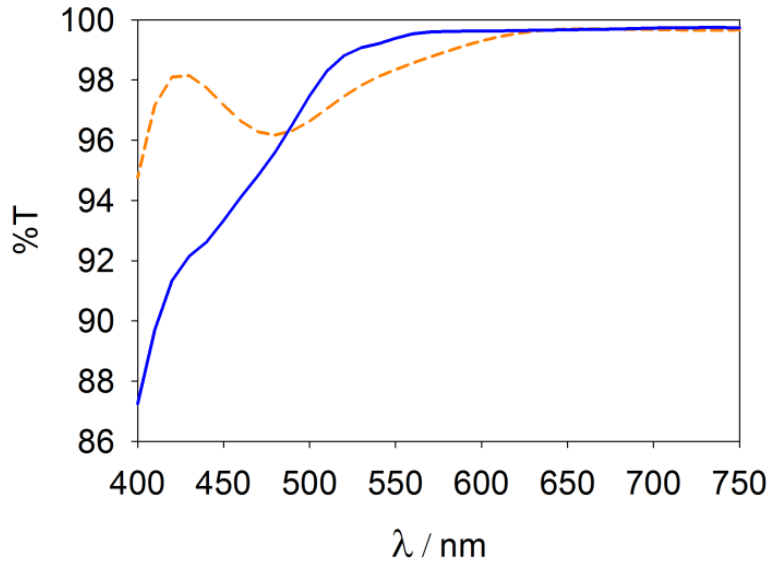

Figure 3.9 Transmittance (T%) of electrolyte layer between counter electrode and TiO_2 film for $[Co(bpy)_3]^{3+/2+}$ (blue solid line) and $[Co(ttcn)_2]^{3+/2+}$ (orange dashed line).

Figure 3.9 shows the transmittance of the electrolyte layer between the counter electrode and TiO_2 film. The light absorption by the $[Co(bpy)_3]^{3+/2+}$ electrolyte is notable below 520nm, and $[Co(ttcn)_2]^{3+/2+}$ has a very small absorption from 420nm to 650nm. The electrolytes transmittances are normalized to the path length of the actual cell which is ~18μm (25 μm sealing Surlyn film thickness subtracted by the TiO_2 film thickness, 7.1μm).

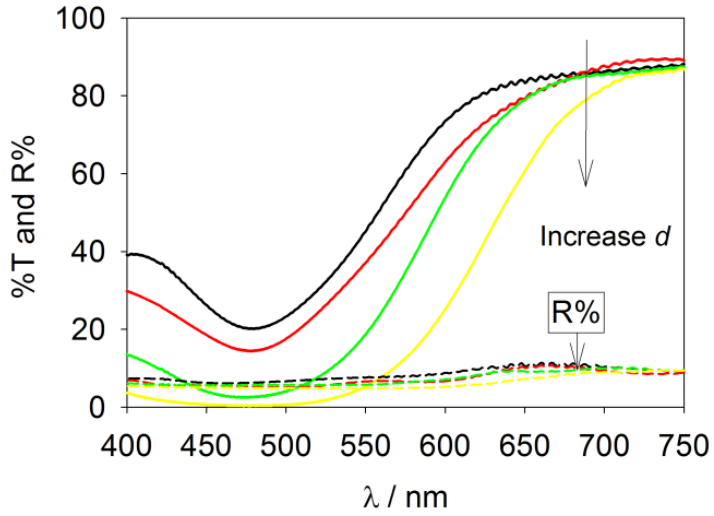

Figure 3.10 Transmittance (T%) and reflectance (R%) of sample cells (sandwich cells assembled using bare 1.2 mm high quality microglass substrates filled with electrolyte) of various TiO_2 film thicknesses, *d*. Electrolyte composition: 0.2M Co(II), 20mM Co(III), 0.10M LiTFSI, 10mM Chenodeoxycholic acid.

Figure 3.10 shows the transmittance (T%) and reflectance (R%) of sample cells with various TiO_2 film thicknesses, *d*, (600nm, 810nm, 1.50µm, 1.80µm) at λ = 450 -750 nm. The absorption maximum of the adsorbed dye is at λ ≈ 470 nm and the transmittance decreases with increasing film thickness. T is close to zero at λ = 450 -500 nm for film thickness 1.80 µm, this indicates the film is thick enough to absorb all incident photons effectively in the wavelength range, and adding thickness to the film will further broaden the zero transmittance range. The transmittance and reflectance at λ > 700 nm is quite similar for all film thicknesses, indicating that the dye can absorb photons up to about 700 nm. The reflectance of the sample cells is ~ 10% and decrease slightly with increasing film thickness at λ = 400nm – 700nm, indicates that the dye absorbs the light strongly and suppresses the light scattering from the film effectively.

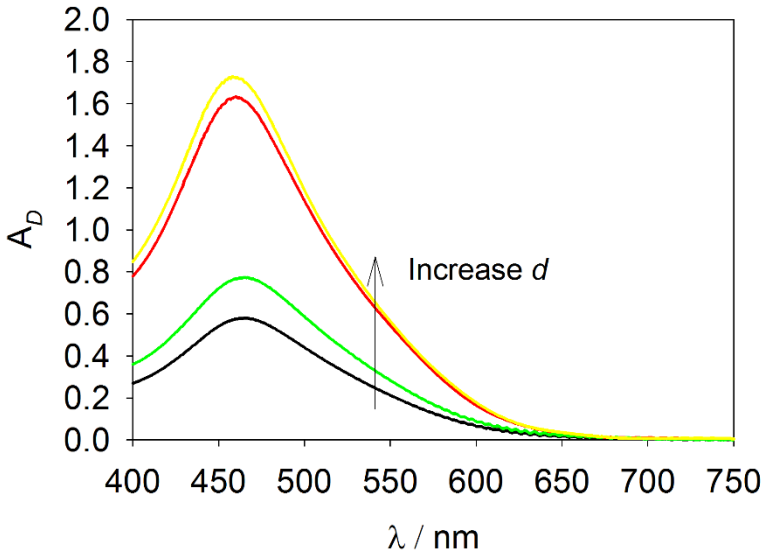

Figure 3.11 Absorbance of D35cpdt sensitized TiO_2 film with various thicknesses.

Figure 3.11 shows the absorbance of D35cpdt sensitized TiO_2 film with various thicknesses, calculated using equation (1) of the main text, and demonstrates that the absorbance increases with film thickness. The dye absorption maximum is around 470nm which blue shifted ~50nm as compared to ethanolic dye solution absorption maximum as shown in Figure S9. This is because when the dye is dissolved in ethanol, the free carboxylate group forms hydrogen bonds with the solvent, which stabilizes the HOMO and shifts the absorption maximum to a longer wavelength. When the dye is absorbed on the nanoparticle surface, it become dehydrolized and is no longer available for hydrogen bonding.

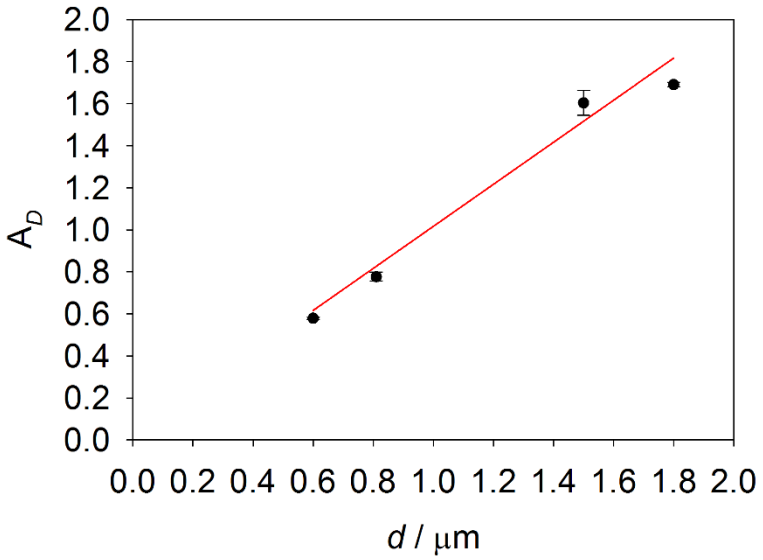

Figure 3.12 Absorbance of sensitized film (A_D) vs. film thickness, *d*, at 467nm and its linear least square fit curve y =1.004x + 0.0159, R=0.970. The error bars indicate the standard deviation from transmittance and reflectance measurements.

Figure 3.12 shows the absorbance of the sensitized film (A_D) vs. film thickness, *d*, at 467nm. The linear relation of A_D and *d* indicates a homogeneous dye loading across the film; a linear least square fit function: y =1.004x + 0.0159 (R^2 = 0.970) was drawn to describe the linearity. The y-intercept value is small and negligible. The value of the slope, 1.004 μm^{-1} at 467nm (peak absorption wavelength), was used to calculate the absorptivity of D35cpdt sensitized TiO_2 film using equation (1). The normalized absorptivity profile of D35cpdt dyed TiO_2 film is shown in Figure S8 and was further used for calculation of light harvest efficiency and IPCEs.

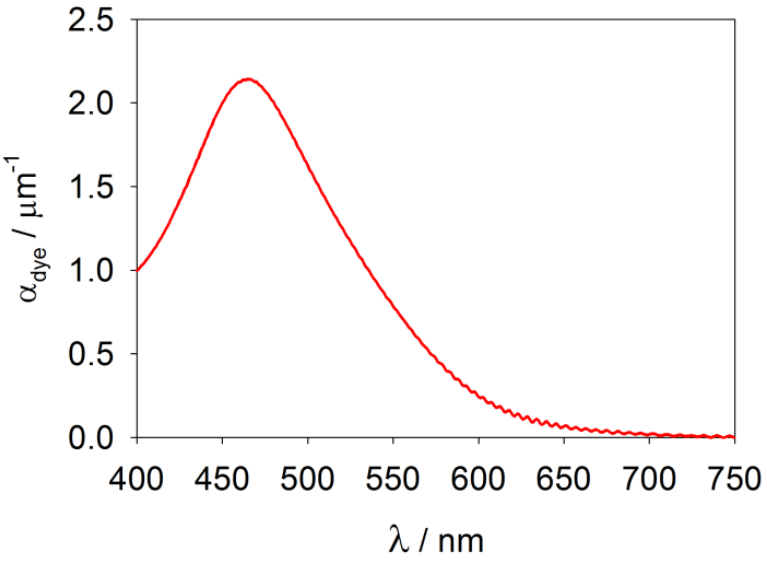

Figure 3.13 Absorptivity of D35cpdt sensitized TiO_2 film.

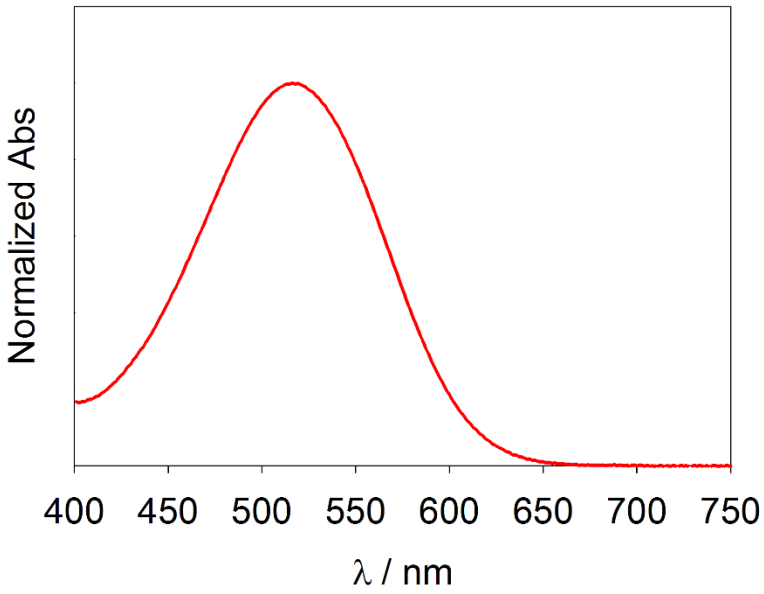

Figure 3.14 Normalized D35cpdt dye absorbance in ethanol.

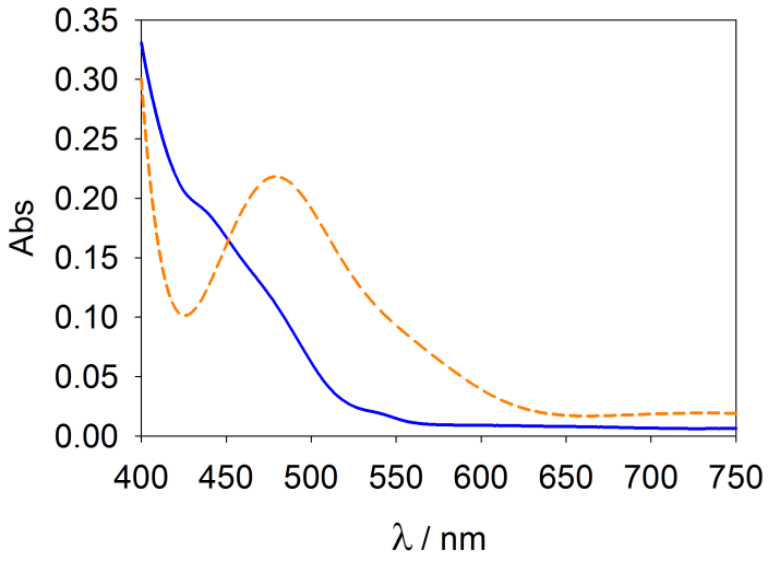

Figure 3.15 Absorbance of 100 times diluted electrolyte solution (0.2 M Co(II), 20mM Co(III), 0.1M LiTFSI and 10mM Chenodeoxycholic acid), $[Co(bpy)_3]^{3+/2+}$ (blue, solid) $[Co(ttcn)_2]^{3+/2+}$ (orange, dashed). Electrolyte solution is diluted to keep maximum absorbance below 2 (According A= -lg T, when 99% light is absorbed) for calculating extinction coefficient of the electrolyte, α_e.

Calculation of light harvest efficiency

$$LHE(FS) = \frac{(1-R)\alpha_{dye}(1-e^{-(\alpha_{dye}+\alpha_e)d})}{\alpha_{dye}+\alpha_e} \qquad LHE(BS) = \frac{(1-R)T_{Pt}T_e\alpha_{dye}(1-e^{-(\alpha_{dye}+\alpha_e)d})}{\alpha_{dye}+\alpha_e}$$

The above two equations are used for calculating light harvest efficiency for front side illumination and back side illumination conditions. [23]

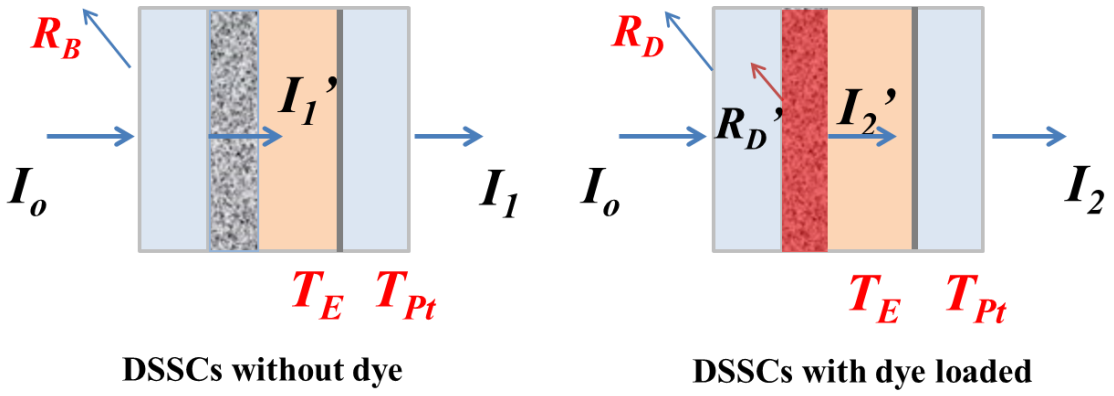

Figure 3.16 Demonstrations of light path in sample cells for optical measurements in UV-vis with integrating sphere detector. Parameters shown are defined below, followed by derivatization of equations for calculating absorption coefficient of dye sensitized TiO_2 film.

Parameters in Figure 3.16.

(I_0 is incident light intensity, I_1 is light intensity transmitted the complete sandwich cell, I_1' is light intensity transmitted after the photoanode substrate, I_2' is light intensity transmitted after the photoanode and dye sensitized nanoparticle TiO_2 film layer.)

T_B & R_B are transmittance and reflectance of a blank sandwich sample cell (no dye loaded).

T_D & R_D are transmittance and reflectance measured from a sensitized sandwich sample cell.

T_D' is the transmittance of dye sensitized nanoparticle TiO_2 film layer

T_E is transmittance of electrolyte layer between counter electrode and nanoparticle film electrolyte side end.

T_{Pt} is the transmittance of a platinized FTO glass.

α_{dye} is absorption coefficient of dye sensitized nanoparticle TiO_2 film.

α_e is absorption coefficient of electrolyte.

P is porosity of the TiO_2 film, P = 0.7 here.

Derivatization of equations for calculating absorption coefficient

$$\frac{I_1}{I_0} = T_B \qquad \frac{I_2}{I_0} = T_D$$

$$I_1 = I_1^{'} \times T_{Pt} \times T_E \qquad I_2 = I_2^{'} \times T_{Pt} \times T_E$$

$$T_D^{'} = \frac{I_2^{'}}{I_1^{'}(1-R_D^{'})} = \frac{I_2}{I_1(1-R_D^{'})} = \frac{T_D}{T_B(1-R_D^{'})}$$

$$R_D^{'} = \frac{R_D - R_B}{T_B^{'2}} \qquad (T_B^{'} = \frac{I_1^{'}}{I_0} = \frac{I_1}{T_{Pt} \times T_E \times I_0} = \frac{T_B}{T_{Pt} \times T_E})$$

$$R_D^{'} = \frac{(R_D - R_B)(T_{Pt} \times T_E)^2}{T_B^{\ 2}}$$

$$T_D^{'} = \frac{T_D}{T_B(1-\frac{(R_D - R_B)(T_{Pt} \times T_E)^2}{T_B^{\ 2}})} = \frac{T_B \times T_D}{T_B^{\ 2} - ((R_D - R_B)(T_{Pt} \times T_E)^2)}$$

$$A_D = -\lg(T_D^{'}) = -(\alpha_{dye}^{10} + \alpha_e P) \times d = \frac{-(\alpha_{dye} + \alpha_e P) \times d}{\ln 10}$$

In a sample cell for optical measurement, 1.2 mm high quality glass substrates are used and no platinum layer was deposited thus term T_{Pt}=1.

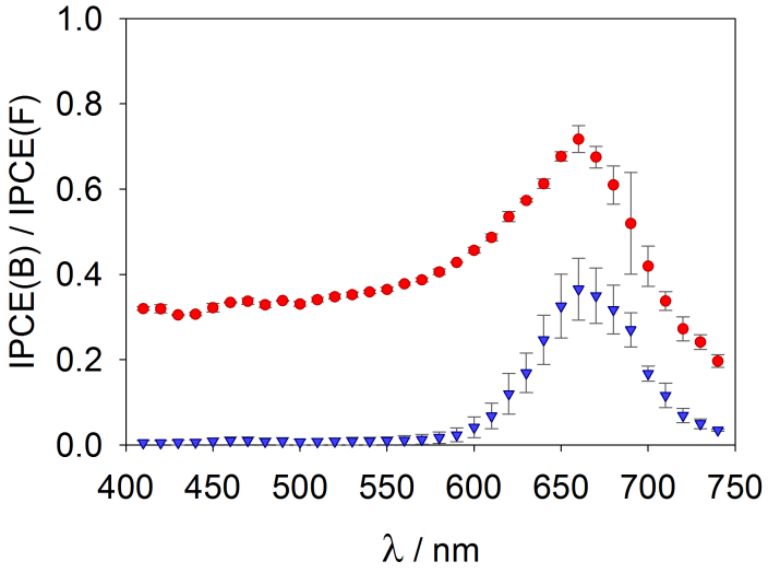

Figure 3.17 IPCE ratio of DSSCs containing the $[Co(bpy)_3]^{3+/2+}$ (red) and $[Co(ttcn)_2]^{3+/2+}$ (blue) redox shuttles, with a 7.1 µm TiO_2 film.

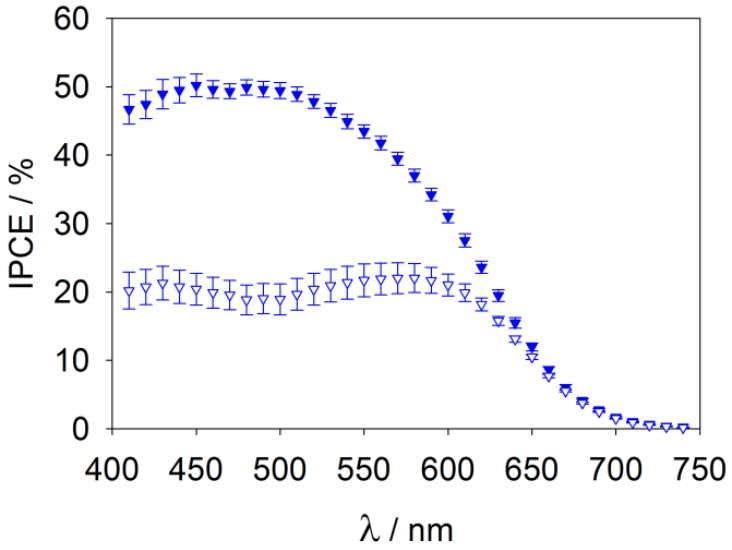

Figure 3.18 IPCE results of DSSCs using $[Co(ttcn)_2]^{3+/2+}$ redox shuttles, FS illumination (filled), BS illumination (hollow); 3.7µm film used here.

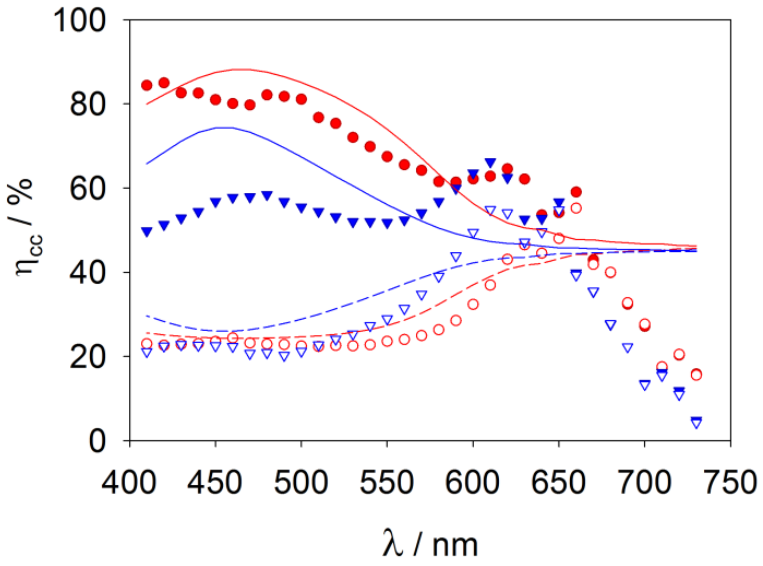

Figure 3.19 Charge collection efficiency (shape) and fit (line) results of DSSCs using $[Co(bpy)_3]^{3+/2+}$ (red) and $[Co(ttcn)_2]^{3+/2+}$ (blue) redox shuttles, FS illumination (filled), BS illumination (hollow); 3.7µm film for $[Co(ttcn)_2]^{3+/2+}$ ($\eta_{inj} \times \eta_{reg} \approx 1.00$), 7.1µm film for $[Co(bpy)_3]^{3+/2+}$($\eta_{inj} \times \eta_{reg} \approx 0.54$).

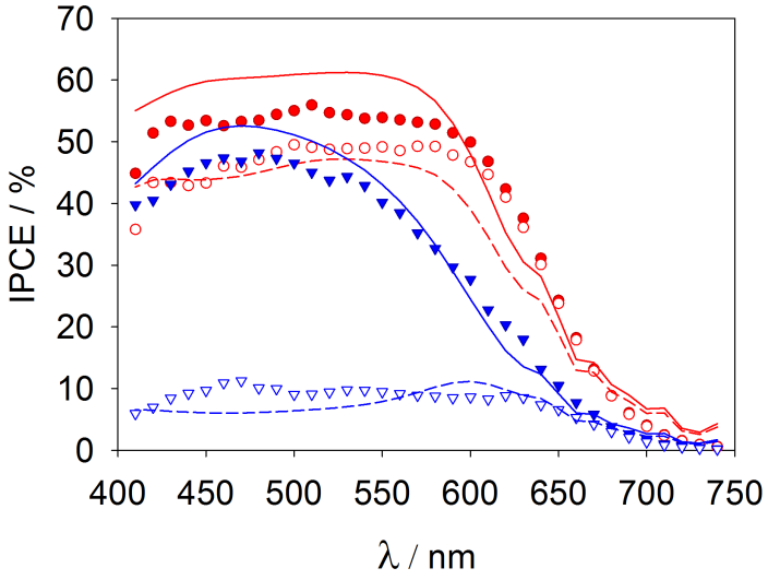

Figure 3.20 IPCE (shape) and fit (line) results of DSSCs with 1 ALD cycle Al_2O_3 coating using $[Co(bpy)_3]^{3+/2+}$ (red) and $[Co(ttcn)_2]^{3+/2+}$ (blue) redox shuttles, FS illumination (filled), BS illumination (hollow); 7.1µm film used here.

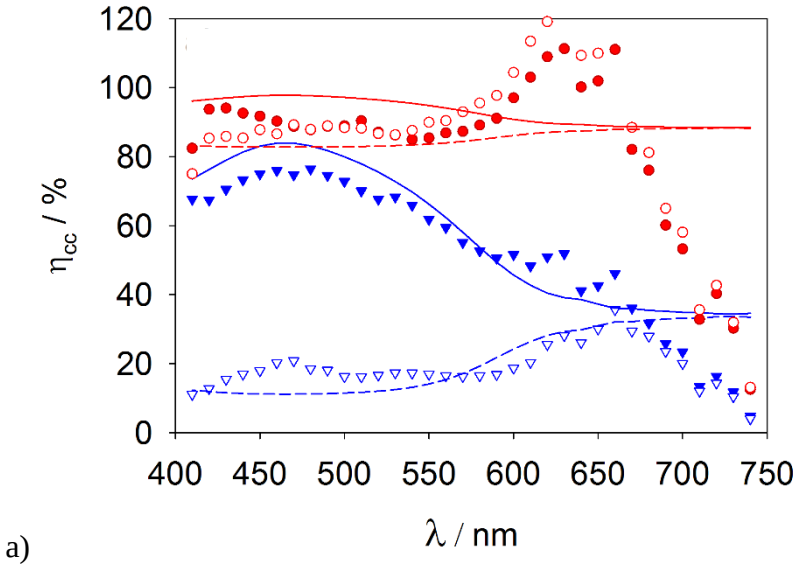

a)

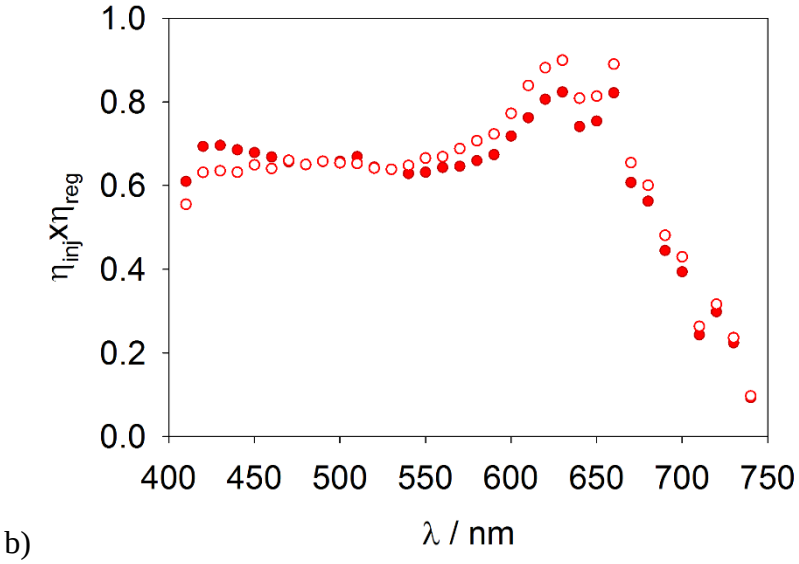

b)

Figure 3.21 Plot of a) charge collection efficiency, $\eta_{inj} \times \eta_{reg} \approx 0.74$ for $[Co(bpy)_3]^{3+/2+}$ & $\eta_{inj} \times \eta_{reg} \approx 0.72$ for $[Co(ttcn)_2]^{3+/2+}$; b) $\eta_{inj} \times \eta_{reg}$ determined by dividing the IPCE with LHE (taking charge collection efficiency as 100%) of DSSCs with 1 ALD cycle Al_2O_3 coating using $[Co(bpy)_3]^{3+/2+}$(red), $[Co(ttcn)_2]^{3+/2+}$ (blue) redox shuttles Front side illumination (filled), Back side illumination (hollow); 7.1µm film used here.

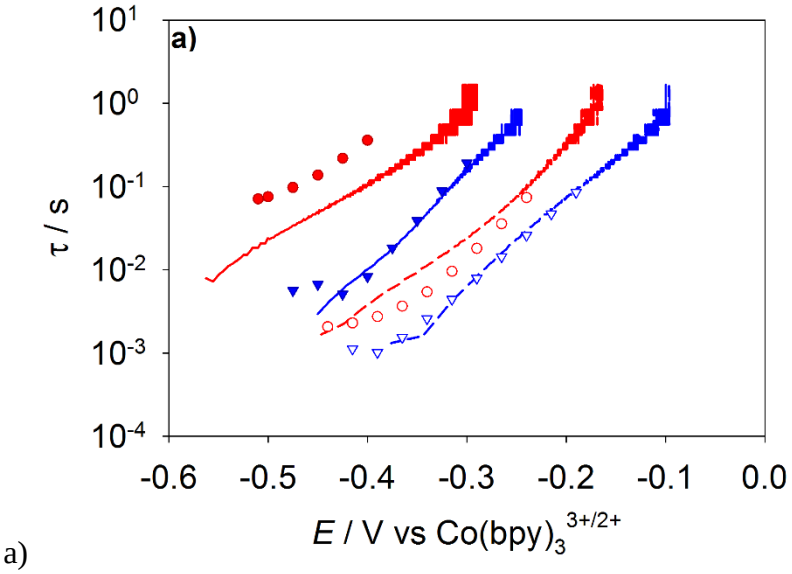

a)

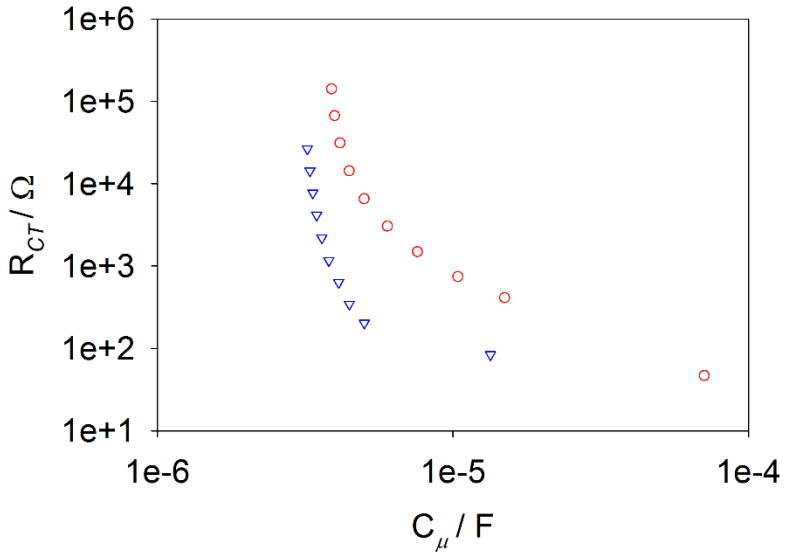

b)

Figure 3.22 a) Lifetimes plots and b) R_{CT} versus chemical capacitance C_μ from electrochemical impedance measurements for DSSCs using $[Co(bpy)_3]^{3+/2+}$ (red) and $[Co(ttcn)_2]^{3+/2+}$ (blue) redox shuttles, with 1 ALD cycle Al_2O_3 coating (filled), without Al_2O_3 coating (hollow). 7.1 μm films were used for all above cell conditions. Superimposed lines are lifetimes derived from open circuit voltage decay measurements.

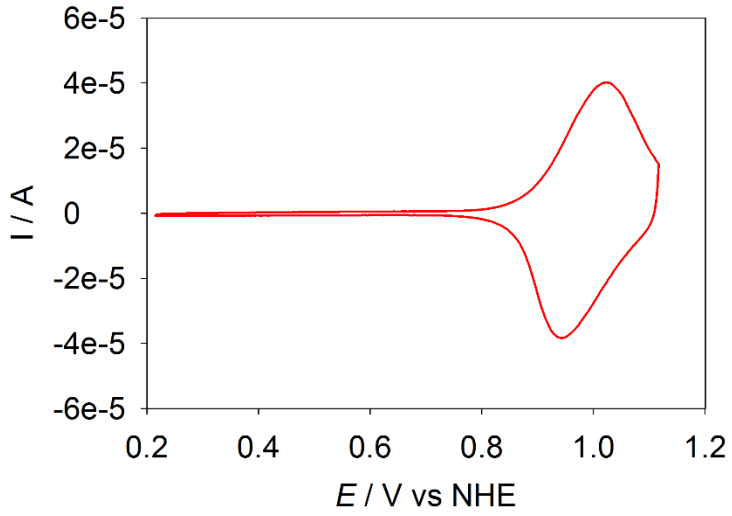

Figure 3.23 Cyclic voltammogram of D35cpdt sensitized ITO (Indium Tin Oxide) nanoparticle film (For better conductivity instead of TiO_2 film) with a 10 mV/s scan rate, using Pt mesh counter electrode and $Ag/AgNO_3$ (acetonitrile) reference electrode. Fc/Fc^+ was used to calibrate the reference electrode potential before and after measurements.

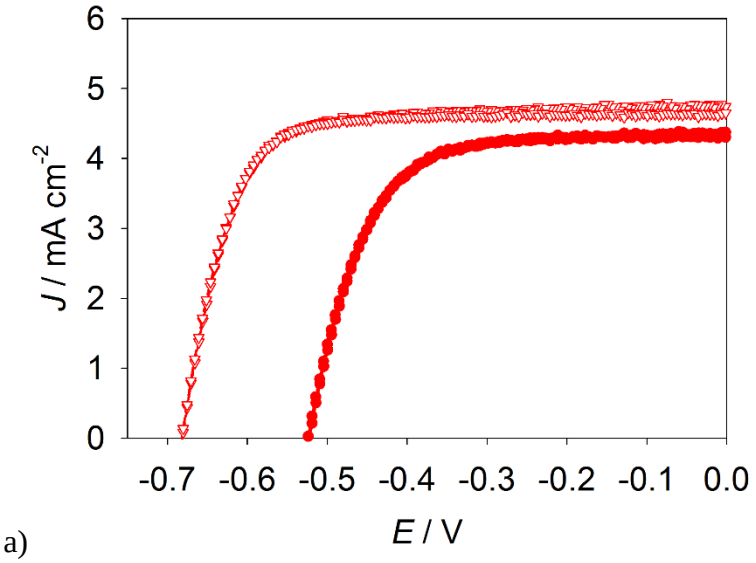

a)

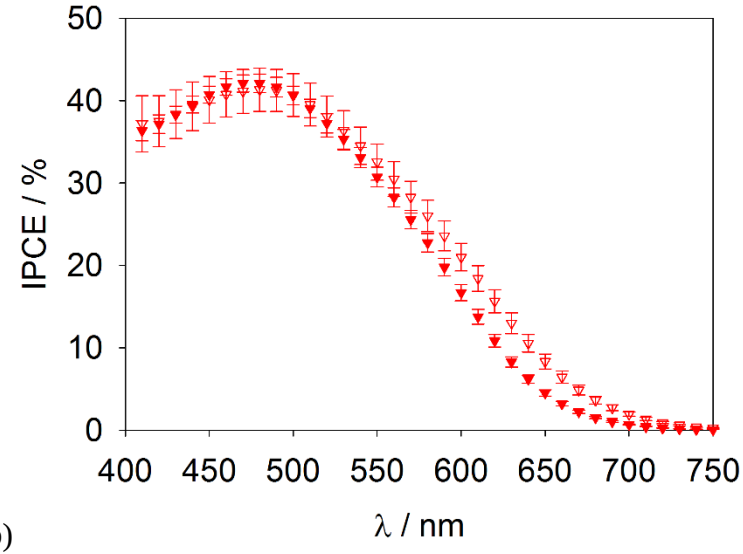

b)

Figure 3.24 Plots of representative a) J-V curves and b) IPCEs of DSSCs with the $[Co(bpy)_3]^{3+/2+}$ based electrolyte including (hollow) and excluding (solid) 4-tert butylpyridine. Electrolyte composition: 0.2 M $[Co(bpy)_3](TFSI)_2$, 0.05 M $[Co(bpy)_3](TFSI)_3$, 0.1 M LiTFSI, 0.2 M 4-tert butylpyridine (optional).

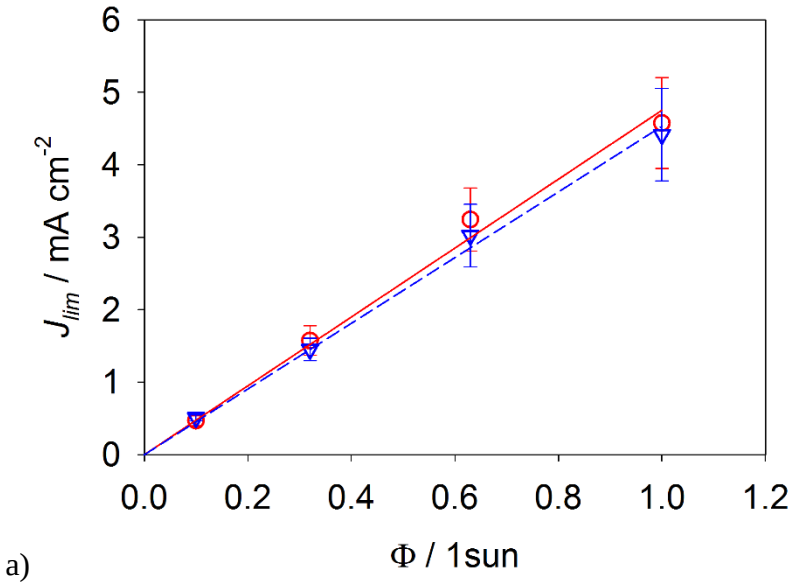

a)

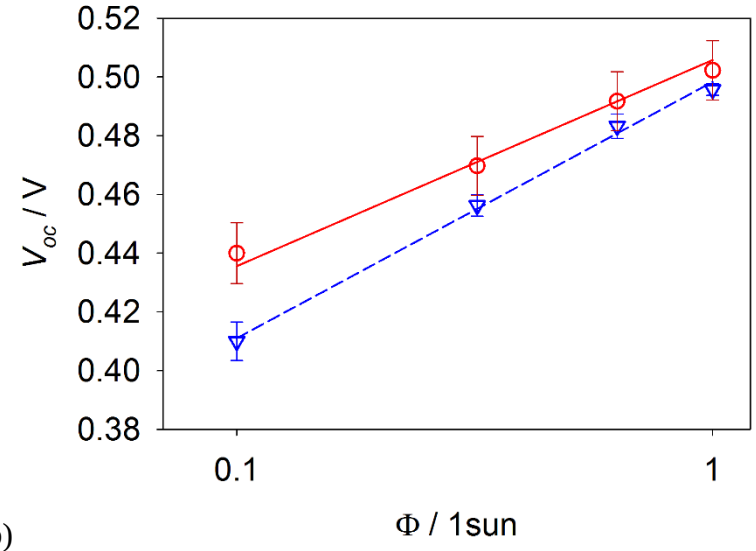

b)

Figure 3.25 Plots of intensity dependency of a) photocurrent Jlim and b) photovoltage Voc, employing redox shuttles $[Co(bpy)_3]^{3+/2+}$ (red circle) and $[Co(ttcn)_2]^{3+/2+}$ (blue triangle). Electrolyte composition: 0.2 M Co(II), 20mM Co(III), 0.1 M LiTFSI, 10mM Chenodeoxylcholic acid in acetonitrile.

REFERENCES

REFERENCES

(1) O'Regan, B.; Grätzel, M. *Nature*. **1991**, *353*, 737–740.

(2) Klahr, B. M.; Hamann, T. W. *J. Phys. Chem. C* **2009**, *113*, 14040–14045.

(3) Ondersma, J. W.; Hamann, T. W. *J. Am. Chem. Soc.* **2011**, *133*, 8264–8271.

(4) Li, T. C.; Spokoyny, A. M.; She, C.; Farha, O. K.; Mirkin, C. a; Marks, T. J.; Hupp, J. T. *J. Am. Chem. Soc.* **2010**, *132*, 4580–4582.

(5) Hattori, S.; Wada, Y.; Yanagida, S.; Fukuzumi, S. *J. Am. Chem. Soc.* **2005**, *127*, 9648–9654.

(6) Daeneke, T.; Mozer, A. J.; Uemura, Y.; Makuta, S.; Fekete, M.; Tachibana, Y.; Koumura, N.; Bach, U.; Spiccia, L. *J. Am. Chem. Soc.* **2012**, *134*, 16925–16928.

(7) Moser, J.; Zakeeruddin, S. M.; Nazeeruddin, M. K.; Gra, M. *J. Phys. Chem. B* **2001**, *105*, 10461–10464.

(8) Feldt, S. M.; Gibson, E. a; Gabrielsson, E.; Sun, L.; Boschloo, G.; Hagfeldt, A. *J. Am. Chem. Soc.* **2010**, *132*, 16714–16724.

(9) Mathew, S.; Yella, A.; Gao, P.; Humphry-Baker, R.; Curchod, B. F. E.; Ashari-Astani, N.; Tavernelli, I.; Rothlisberger, U.; Nazeeruddin, M. K.; Grätzel, M. *Nat. Chem.* **2014**, *6*, 242–247.

(10) Yella, A.; Lee, H.-W.; Tsao, H. N.; Yi, C.; Chandiran, A. K.; Nazeeruddin, M. K.; Diau, E. W.-G.; Yeh, C.-Y.; Zakeeruddin, S. M.; Grätzel, M. *Science* **2011**, *334*, 629–634.

(11) Feldt, S. M.; Lohse, P. W.; Kessler, F.; Nazeeruddin, M. K.; Grätzel, M.; Boschloo, G.; Hagfeldt, A. *Phys. Chem. Chem. Phys.* **2013**, *15*, 7087–7097.

(12) Marcus, R. A.; Sides, P. In *Mechanistic Aspects of Inorganic Reactions*; Rorabacher, D. B., Endicott, J. F., Eds.; American Chemical Society: Washington, D. C., 1982; p 235.

(13) Nelson, J. J.; Amick, T. J.; Elliott, C. M. *J. Phys. Chem. C* **2008**, *112*, 18255–18263.

(14) Marcus, R. A.; Sutin, N. *Biochim. Biophys. Acta - Rev. Bioenerg.* **1985**, *811*, 265–322.

(15) Brunschwig, B. S.; Creutz, C.; Sutin, N. *Chem. Soc. Rev.* **2002**, *31*, 168–184.

(16) Brunschwig, B. S.; Creutz, C.; Macartney, D. H.; Sham, T.-K.; Sutin, N.; May, R. *Faraday*

Discuss. Chem. Soc. **1982**, *74*, 113–127.

(17) Hamann, T. W.; Gstrein, F.; Brunschwig, B. S.; Lewis, N. S. *J. Am. Chem. Soc.* **2005**, *127*, 13949–13954.

(18) Xie, Y.; Hamann, T. W. *J. Phys. Chem. Lett.* **2013**, *4*, 328–332.

(19) Tachibana, Y.; Hara, K.; Sayama, K.; Arakawa, H. *Chem. Mater.* **2002**, *14*, 2527–2535.

(20) Klahr, B. M.; Martinson, A. B. F.; Hamann, T. W. *Langmuir* **2011**, *27*, 461–468.

(21) Haque, S. a; Palomares, E.; Cho, B. M.; Green, A. N. M.; Hirata, N.; Klug, D. R.; Durrant, J. R. *J. Am. Chem. Soc.* **2005**, *127*, 3456–3462.

(22) Peter, L. M. *J. Phys. Chem. C* **2007**, *6*, 555–565.

(23) Halme, J.; Boschloo, G.; Hagfeldt, A.; Lund, P. *J. Phys. Chem. C* **2008**, *14*, 5623–5637.

(24) Barnes, P. R. F.; Anderson, A. Y.; Koops, S. E.; Durrant, J. R.; O'Regan, B. C. *J. Phys. Chem. C* **2009**, *113*, 1126–1136.

(25) Barnes, P. R. F.; Liu, L.; Li, X.; Anderson, A. Y.; Kisserwan, H.; Ghaddar, T. H.; Durrant, J. R.; Regan, B. C. O. *Nano Lett.* **2009**, *9*, 3532–3538.

(26) Yang, W.; Vlachopoulos, N.; Hao, Y.; Hagfeldt, A.; Boschloo, G. *Phys. Chem. Chem. Phys.* **2015**, *17*, 15868–15875.

(27) Ondersma, J. W.; Hamann, T. W. *J. Phys. Chem. C* **2010**, *114*, 638–645.

(28) Soman, S.; Xie, Y.; Hamann, T. W. *Polyhedron* **2014**, *82*, 139–147.

(29) Zaban, A.; Greenshtein, M.; Bisquert, J. *ChemPhysChem* **2003**, *4*, 859–864.

(30) Hamann, T. W.; Ondersma, J. W. *Energy Environ. Sci.* **2011**, *4*, 370.

(31) Makinen K Hakkinen, H, V. H. *J. Phys. Chem. C* **2011**, *115*, 9259.

(32) Palomares, E.; Clifford, J. N.; Haque, S. a; Lutz, T.; Durrant, J. R. *J. Am. Chem. Soc.* **2003**, *125*, 475–482.

(33) Dryza, V.; Bieske, E. J. *J. Photochem. Photobiol. AChemistry* **2015**, *302*, 35–41.

(34) Ellis, H.; Eriksson, S. K.; Feldt, S. M.; Gabrielsson, E.; Lohse, P. W.; Lindblad, R.; Sun, L. *J. Phys. Chem. C* **2013**, *117*, 21029-21036.

(35) Gabrielsson, E.; Ellis, H.; Feldt, S.; Tian, H.; Boschloo, G.; Hagfeldt, A.; Sun, L. *Adv. Energy Mater.* **2013**, *3*, 1647–1656.

(36) Koops, S. E.; O'Regan, B. C.; Barnes, P. R. F.; Durrant, J. R. *J. Am. Chem. Soc.* **2009**, *131*, 4808–4818.

(37) Feldt, S. M.; Wang, G.; Boschloo, G.; Hagfeldt, A. *J. Phys. Chem. C* **2011**, *115*, 21500–21507.

(38) Barnes, P. R. F.; Anderson, A. Y.; Durrant, J. R.; O'Regan, B. C. *Phys. Chem. Chem. Phys.* **2011**, *13*, 5798–5816.

(39) Jennings, J. R.; Liu, Y.; Wang, Q. *J. Phys. Chem. C* **2011**, *115*, 15109–15120.

(40) Li, F.; Jennings, J. R.; Wang, Q. *ACS Nano* **2013**, *7*, 8233–8242.

(41) Royea, W. J.; Hamann, T. W.; Brunschwig, B. S.; Lewis, N. S. *J. Phys. Chem. B* **2006**, *110*, 19433–19442.

(42) Blomgren, G. E. In *Non-aqueous Electrochemistry*; Aurbach, D., Ed.; Marcel Dekker: New York, NY, 1999; pp 53–79.

(43) *CRC Handbook of Chemistry and Physics, 81st ed*, 81st ed.; Lide, D. R., Ed.; CRC Press: Boca Raton, FL, 2001.

(44) Enright, B.; Fitzmaurice, D. *J. Phys. Chem.* **1996**, *100*, 1027–1035.

(45) Rothenberger, G.; Fitzmaurice, D.; Gratzel, M. *J. Phys. Chem.* **1992**, *96*, 5983–5986.

Chapter 4 Spin controlled cobalt redox couples with fine-tuning structure

4.1 Abstract

Low spin cobalt redox shuttle, e.g. $[Co(ttcn)_2]^{3+/2+}$ have been an attractive alternative cobalt based outer-sphere redox shuttle owing to the distinct low spin d^7 to low spin d^6 electron transfer feature. Quantitative regeneration is achieved with low spin $[Co(ttcn)_2]^{2+}$ in conjunction with D35cpdt dye, however, short diffusion length is still a limitation. Here we introduce a new low spin cobalt(II) based redox shuttle, $[Co(PY5Me_2)(CN)]^{2+/+}$, where $PY5Me_2$ is the pentadentate ligand, 2,6-bis(1,1-bis(2-pyridyl)ethyl)pyridine. The spin state of Co(II) is successfully controlled by introducing strong field ligand –CN, also a redox potential of 0.230 V vs. NHE is obtained. In comparison to high spin $[Co(bpy)_3]^{2+}$, $[Co(PY5Me_2)(CN)]^{2+/+}$ presents better performances in absence of mass transport limitation, e.g. at low light intensity. Evaluation of recombination and regeneration employing Marcus theory indicated a quantitative regeneration and comparable charge collection in $[Co(PY5Me_2)(CN)]^{2+/+}$ compared to $[Co(bpy)_3]^{3+/2+}$, which is in good agreement with experimental findings.

4.2 Introduction

We have introduced a new motif for using low spin cobalt redox shuttles in chapter 2, and our study on the kinetics of regeneration and recombination in chapter 3 further proved that the dye regeneration process is quantitative by utilizing low spin cobalt(II) based redox shuttles $[Co(ttcn)_2]^{3+/2+}$ though there is a ~60mV less regeneration driving force compared to that of high spin cobalt(II) redox shuttles $[Co(bpy)_3]^{3+/2+}$. However, $[Co(ttcn)_2]^{3+/2+}$ suffers from fast recombination process which results in poor charge collection efficiency. Adding a thin insulting coating to the semiconductor by ALD is able to improve the charge collection to some extent, but decrease the dye injection efficiency. Thus, it would be advantageous to develop low spin cobalt

redox shuttles which can deliver quantitative regeneration as well as obtains efficient charge collection for efficient DSSCs prototype development in future. The idea is designing redox shuttles with more negative potential with controlled spin state.

Through fine-tuning the ligand structure, potentials can be easily manipulated, for example, the $[Co(bpy)_3]^{3+/2+}$ and $[Co(phen)_2]^{3+/2+}$ based series redox potential can be tuned by electron donating or withdrawing substituents on the bpy or phen ligand. However, quite different from the bpy and phen conjugated π systems in which the electron localization on N donor atoms can be affected by substituents, the thiacycloether ligand, such as ttcn = 1,4,7-trithiacyclononane, was coordinated to cobalt metal center through the electron lone pairs of the S atoms as σ donor. The carbons on the ligand ring are sp3 carbons thus no conjugated π systems exist in the ligand, adding substituents on the carbons and increasing the number of carbon atom on the ring system have no significant effect on the electron localization on S donor atoms.[1–3] Therefore, the potentials of the $[Co(ttcn)_2]^{3+/2+}$ based redox shuttles cannot be easily tuned to fulfill the aim of expanding the low spin cobalt redox shuttle family. Alternative ligand system need to be developed. Bach et al.[4] introduced a new approach to design redox shuttles for DSSCs that involves the application of $[Co(PY5Me_2)(MeCN)]^{2+/+}$ complexes, where $PY5Me_2$ is the pentadentate ligand, 2,6-bis(1,1-bis(2-pyridyl)ethyl)pyridine. The complex structure is highly tunable via introducing ligand with various donor abilities to the axial coordination site. Stack et al.[5] studied the spectroscopic and structural properties of a series ferrous complexes with 2,6-(bis-(bis-2-pyridyl)methoxymethane)pyridine (PY5) ligand, by changing the axial ligand, they were able to manipulate the spin state of these complexes, binding affinities of many anionic and neutral ligands were also investigated. Cynide ligand, -CN, due to its anionic ligand feature, provides strong donor ability to push the complex potential more negative, also offers a strong binding affinity to make

the complex stable. In addition, as a strong field ligand, it is capable of controlling the metal center spin state to low spin, as demonstrated in the complex, $[Fe(PY5)(CN)]^{+}$.[5]

Therefore, here we introduce a low spin cobalt redox shuttle, $[Co(PY5Me_2)(CN)]^{2+/+}$. Introduction of –CN to the axial coordination site successfully tuned the redox potential to a value of 0.23 V vs. NHE, which is ~ 400 mV more negative potential than that of low spin $[Co(ttcn)_2]^{3+/2+}$. The new redox shuttle is potentially interesting to overcome the drawback that $[Co(ttcn)_2]^{3+/2+}$ is limited by short electron diffusion length. If assuming similar reorganization energy as $[Co(ttcn)_2]^{3+/2+}$, there is a ~ 400 mV less driving force for electron recombination to $[Co(PY5Me_2)(CN)]^{2+}$ which might lead to a slower recombination and better charge collection. We have successfully synthesized and fully characterized the new low spin cobalt redox shuttles, $[Co(PY5Me_2)(CN)]^{2+/+}$. Theoretical calculation of reorganization energy using single X-ray diffraction data and force constants yield an inner-sphere reorganization energy of ~0.67 eV which gives a crude estimation of a fast self-exchange rate constant ranging from ~1.4×10^3 to 1.4×10^4 M^{-1} s^{-1}. The effect of driving force on regeneration and recombination was also discussed employing Marcus theory. Quantitative regeneration and comparable charge collection to $[Co(bpy)_3]^{3+/2+}$ may be obtained. These exciting results demonstrated the promise of tuning spin state and redox potential for cobalt based redox shuttles which offers advantage in reducing the energy loss and improving efficiency of DSSCs.

4.3 Experimental

4.3.1 Materials and methods

All general reagents and solvents were obtained from Sigma Aldrich and used as received unless stated otherwise. Solvents used are dried and stored in glovebox. The sensitizer D35cpdt was purchased from Dyenamo. Cobalt tris-bipyridyl redox shuttles are prepared as reported

previously.[6] UV-vis spectra were performed using a Perkin-Elmer Lambda 35 UV-vis spectrometer. High resolution mass spectra (HRMS) were obtained at the Michigan State University Mass Spectrometry Service Center using a Waters GCT Premier instrument run on electron ionization (EI) direct probe or a Waters QTOF Ultima instrument run on electrospray ionization (ESI+). Infrared spectroscopy was obtained at Michigan State University using an FT-IR Mattson spectrometer. NMR spectra were measured on an Agilent DirectDrive2 500 spectrometer and referenced to residual solvent signals. All coupling constants are apparent J values measured at the indicated field strengths in Hertz (s = singlet, d = doublet, t = triplet, q = quartet, dd = doublet of doublets, bs = broad singlet). All electrochemistry experiments were performed at 22 ^{o}C in a three electrode cell connected to a Autolab PGSTAT 128N potentiostat. The reference electrode was a homemade $Ag/AgNO_3$ non-aqueous (acetonitrile) electrode. $Fc^{+/0}$ was used as an internal reference.

4.3.2 Synthesis of the cobalt complexes

Unless otherwise noted, all synthesis procedures are performed under inert N_2 atmosphere using schlenk line or standard glovebox techniques. The ligand $PY5Me_2$ (2,6-bis(1,1-bis(2-pyridyl)ethyl)pyridine) was synthesized according to literature reported methods.[7] The synthesized ligand purity was confirmed with NMR and elemental analysis, included in the supporting information. The starting material $Co(OTf)_2$ (OTf = trifluromethanesulfonate) is made from anhydrous $CoCl_2$ and triflate acid following literature reported method.[8] The complex $[Co(PY5Me_2)(MeCN)](OTf)_2$ was synthesized using literature reported method, but the reaction time was reduced to 20 min and an ice/water bath was used to cool down the reaction.[9] The purity of the product was measured by elemental analysis, found (calcd) for $C_{33}H_{28}CoF_6N_6O_6S_2$: C,

45.33(47.09); H, 3.03(3.35); N, 8.56(9.98). The complexes lost the –MeCN ligand in the mass spectroscopy, and an intense peak of $Co(PY5Me_2)^{2+}$ is shown at 251.0886.

[Co(PY5Me$_2$)(CN)](OTf). This complex was obtained by addition of KCN (0.24 mmol, 15.6 mg) into a stirred solution of $[Co(PY5Me_2)(MeCN)](OTf)_2$ (0.2 mmol, 168 mg) in 10 mL aceton/water (9:1) mixture, at room temperature. Upon addition, the solution color turned from bright yellow/orange to dark red immediately. The solution was stirred for 1 hr at room temperature. Pink/Ruby colored precipitate formed after 15 min reaction time. After 1 hr stirring, the reaction mixture was filtered, then the filtrate was reduced to dryness by rotary evaporator at reduced pressure, yielding dark red powder. Further dissolution of the dark red powder in acetone yield brown solution. The brown solution is filtered through celite to remove residue amount of potassium salt. Further removal of the solvent in the filtrate yielded the pure product (~75% yield) which was then dried under vacuum overnight and stored in a N_2 glovebox. Crystals suitable for single crystal X-ray diffraction analysis were obtained by vapor diffusion of ether into a concentrated acetonitrile solution of $[Co(PY5Me_2)(CN)](OTf)$ at room temperature. An intense peak for $[Co(PY5Me_2)(CN)]^+$ at 528.2 was observed on mass spectroscopy (M+), spectra shown in the appendix. Elemental analysis: found (calcd) for $C_{31}H_{25}CoF_3N_6O_3S$: C, 54.47(54.95); H, 3.71(3.72); N, 11.90(12.40). The effective magnetic moment of the complex is 2.43 μ_B, measured with Evans balance.

[Co(PY5Me$_2$)(CN)](OTf)$_2$. The complex is synthesized by adding equivalent amount of oxidant AgOTf to $[Co(PY5Me_2)(CN)](OTf)$ solution in acetonitrile. The reaction was stirred in dark for 1 hr, yielding black silver precipitation and yellow solution. Ag precipitation was removed by filtration through celite for three times. The filtrate was then concentrated at room temperature, slowly addition of diethyl ether to the concentrated solution yielded a light orange color precipitate

as the product. Crystal of the complex suitable for single crystal X-ray diffraction measurement was obtained by vapor diffusion of diethyl ether to concentrated solution of the complex in acetonitrile at room temperature. Elemental analysis: Found (Calcd) for $C_{32}H_{25}CoF_6N_6O_6S$: C, 45.67(46.5); H, 3.17(3.05); N, 9.59(10.17). An intense peak for $[Co(PY5Me_2)(CN)]^{2+}$ at 264.1 was observed on mass spectroscopy (M+). H^1NMR (500 MHz, acetone-d_6, 22 ^{0}C): δ (ppm) 3.12 (s, 6H), 7.88-7.90 (td, 4H), 8.31-8.33 (td, 4H), 8.37-8.39 (dd, 4H), 8.67-9.69 (m, 3H), 10.25-10.26 (dd, 4H). Mass spectra and H^1NMR is shown in the appendix.

4.3.3 Single crystal X-ray diffraction measurements

Crystals were mounted on a nylon loop with paratone oil on a Bruker APEX-II CCD diffractometer. The crystal was kept at T = 173(2) K during data collection. Using Olex2 (Dolomanov et al., 2009), the structure was solved with the ShelXS (Sheldrick, 2008) structure solution program, using the Direct Methods solution method. The model was refined with version 2014/6 of XL (Sheldrick, 2008) using Least Squares minimization. All non-hydrogen atoms were refined anisotropically. Hydrogen atom positions were calculated geometrically and refined using the riding model. There are two independent molecules in the asymmetric unit. Structure and refinement data are summarized in Table 4.1 for $[Co(PY5Me_2)(CN)](OTf)$ and $[Co(PY5Me_2)(CN)](OTf)_2$.

4.3.4 DSSCs fabrication

TiO_2 photoanodes were prepared and sandwiched in a similar manner as described in chapter 2.3.1. using Solaronix T/SP (average particle size ~20nm) TiO_2 paste deposited on FTO substrate with ~15nm TiO_2 blocking layer (1000 cycle ALD). D35cpdt dye solution consisting of 0.2 mM D35cpdt and 5 mM chenodeoxycholic acid in ethanol was used for dye soaking process. Electrolyte consisting of 0.2 M Co(II), 20 mM Co(III), 0.1 M LiOTf in anhydrous propylene

carbonate/acetonitrile (2:3 ratios by volume) solvent mixture. Pt counter electrodes were prepared by drop casting 5 mM H_2PtCl_6 in isopropyl alcohol on FTO following by heating in air at 380 ^{0}C for 20 min. The graphene nanoplatelet counter electrodes were prepared following literature reported method,[10] 50 mg Graphene nanoplatelets, grade 3 (GNP) (Cheap Tubes, Inc. ,USA) were dispersed in isopropyl alcohol by sonication (ca. 10min) and the solution were left overnight to allow big particles sediment. The supernatant dispersion layer was then used for drop casting on FTO followed by annealing in Ar atmosphere at 500 ^{0}C for 1 hr.

4.3.5 Current voltage and IPCE measurements

Current-Voltage and IPCE measurements are taken following method described in chapter 3.

4.3.6 Electrochemical impedance measurements

Electrochemical impedance spectroscopy, EIS, measurements were performed in the dark using a FRA2 integrated with the PGSTAT 128N. The impedance spectra were recorded at applied potentials from -0.3 to -0.55 V, stepped in 25 mV increments, with a 10 mV alternating potential superimposed on the direct bias, each impedance measurement consisted of frequency sweeps from 5×10^{-2} to 1×10^5 Hz in equally spaced logarithmic steps. Rate constant measurement via EIS was carried at open circuit, V= 0 V, while other conditions are kept unchanged.4.3.

4.3.7 Magnetic susceptibility measurement

Magnetic susceptibility of powdered sample was measured with Evan's balance. Magnetic susceptibility of paramagnetic species in acetonitrile were also determined using Evans method by NMR according to literature reported procedure[11,12]at variant temperature ranging from -40 to 45 ^{0}C. Regular NMR tube with a capillary inserts was used for the solution magnetic susceptibility measurement where the capillary inserts is filled with solution of diamagnetic standards $O(SiMe_3)_2$

in acetonitrile-D6 (20μL $O(SiMe_3)_2$ in 1mL acetonitrile-D6), and the NMR tube is filled with solution of interested paramagnetic sample and diamagnetic standards in acetonitrile-D6.

4.4 Results and discussions

4.4.1 Crystallography

Single crystal structures and selected bond length/angle of $[Co^{II}(PY5Me_2)(CN)]^+$ is presented in figure 4.1 and table 4.2, packing diagrams $[Co^{II}(PY5Me_2)(CN)]^+$ and $[Co^{III}(PY5Me_2)(CN)]^{2+}$ are shown in appendix. Both complexes showed a distorted octahedral structure because the cis N-Co-N bond angles on the equatorial plane are deviated from 90° by ~5° to 9°. In $[Co^{II}(PY5Me_2)(CN)]^+$,the average Co-N bond length is 2.079 Å (ranging from 1.977 to 2.138 Å) , Co-C bond length is 1.913 Å. In $[Co^{III}(PY5Me_2)(CN)]^{2+}$, the average Co-N bond length is 1.981 Å , Co-C bond length is 1.888 Å. The Co-N average bond length change from Co(II) to Co(III) is ~ 0.113 Å. This is a result of $\{[4(0.126)^2 + (0.015)^2]/5\}^{1/2}$, where 0.126 Å is the average Co-N bond length change on the equatorial plane, and 0.015 Å is for the axial Co-N bond length change in order to take into account the uneven bond length change due to Jahn-Teller distortion effect in d^7 electronic configuration. A previously reported complexes with similar structure, $Co^{II/III}(PY5Me_2)(NMBI)$, where NMBI is *N*-methylbenzimidazole,[4] there is an average Co-N bond length change of 0.150 Å (from Co^{II}-N 2.135 Å to Co^{III}-N 1.985 Å). The average Co-N bond length of $[Co^{II}(PY5Me_2)(NMBI)]^{2+}$ is also much longer than that of $[Co^{II}(PY5Me_2)(CN)]^+$. The bond length feature is close related to the spin state of Co metal center in the complexes. $[Co^{II}(PY5Me_2)(NMBI)]^{2+}$ is a high spin Co(II) according to literature, while $[Co^{II}(PY5Me_2)(CN)]^+$ is a low spin Co(II) which is indicated by an effective magnetic moment of ~1.8 μ_B from magnetic susceptibility measurements. In a high spin Co(II) ($t_{2g}^5e_g^2$) complexes, there is a significant lengthening of the Co-N bond due to that the electron population of e_g^* antibonding orbitals as

compared to a low spin cobalt Co(III) ($t_{2g}^6e_g^0$). Same effects have been observed in other high spin Co(II) complexes such as $Co(bpy)_3$ and $Co(phen)_2$, where there a ~0.19 Å bond length change is observed.[3,13,14] Therefore the much smaller bond length change from Co(II) to Co(III) in $Co(PY5Me_2)(CN)$ complexes can be attributed to the low spin Co(II) (($t_{2g}^6e_g^1$) to low spin Co(III) ($t_{2g}^6e_g^0$) owing to a much smaller electron transfer barrier compared to that of high spin Co(II) complexes. The small average bond length changes also indicated a possible fast electron transfer mechanism for $Co^{II/III}(PY5Me_2)(CN)$ result from smaller inner-sphere reorganization energy. More detailed discussion of the structural effects on reorganization energy are given in another section below.

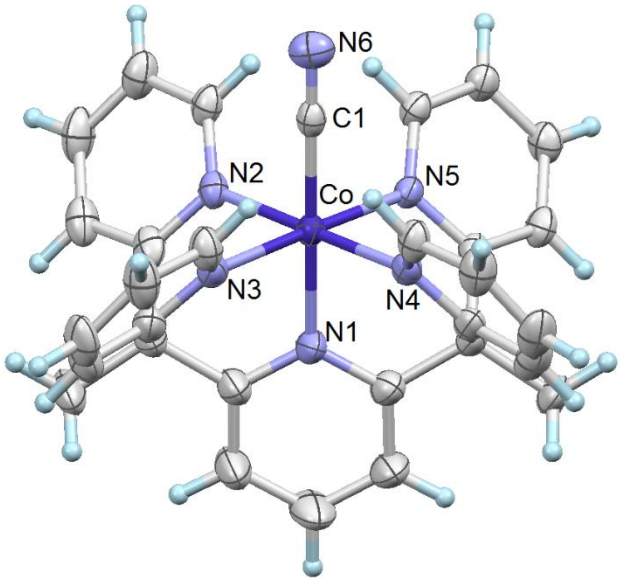

Figure 4.1 Crystal structures of the octahedral complex $Co^{III}(PY5Me_2)(CN)]^{2+}$. $[Co^{II}(PY5Me_2)(CN)]^+$ structure is similar thus not displayed here. Dark blue, light grey and pale purple spheres representing Co, C, N, respectively. Ellipsoids are depicted at the 50% probability level.

Table 4.1 Crystallographic data for [Co(PY5Me$_2$)(CN)](OTf) and [Co(PY5Me$_2$)(CN)](OTf)$_2$.

Formula	$C_{33}H_{28}CoF_3N_7O_3S$	$C_{35}H_{31.5}CoF_6N_{6.5}O_{6.5}S_2$
Formula Weight	718.61	884.22
Crystal System	triclinic	triclinic
Space Group	P-1	P-1
a/Å	14.2538(2)	10.3672(2)
b/Å	15.6315(2)	11.2824(2)
c/Å	17.2705(3)	16.1555(3)
α/°	73.2243(9)	73.7610(10)
β/°	68.4389(9)	83.3770(10)
γ/°	63.4098(9)	88.0000(10)
V/Å^3	3164.38(9)	1802.15(6)
Z	4	2
$\rho_{calc.}$/ g cm^{-3}	1.508	1.629
μ/mm^{-1}	5.432	5.615
Crystal size/mm^3	0.28×0.27×0.05	0.25×0.15×0.07
2Θ range/°	2.782 to 72.212	2.866 to 72.075
Measured Refl.	43158	28673
Independent Refl.	11856	6784
Reflections Used	8910	5648
R_{int}	0.0639	0.0636
Parameters	871	555
Restraints	0	50
Largest Peak	0.838	0.475
Deepest Hole	-0.563	-0.475
Goodness of Fit	1.024	1.048
wR_2 (all data)	0.1374	0.1280
wR_2 (I>2σI)	0.1219	0.1210
R_1 (all data)	0.0773	0.0598
R_1 (I>2σI)	0.0514	0.0475

4.4.2 UV-vis and IR spectroscopy

The UV-vis spectra of complexes $[Co^{II}(PY5Me_2)(CN)]^+$ and $[Co^{III}(PY5Me_2)(CN)]^{2+}$ are shown in figure 4.2. For both Co(II) and Co(III) complexes, the broad absorption below 350 nm are likely originated from metal independent $\pi \rightarrow \pi^*$ transitions within the $PY5Me_2$ ligand (UV of $PY5Me_2$ is shown in the appendix). The other broad absorption band with maximum at 350 nm for Co(II) and 450nm for Co(III) complexes are assigned to the metal to ligand charge transfers (MLCT).

IR measurements were taken to monitor the C ≡ N stretching, and the spectra of $[Co^{II}(PY5Me_2)(CN)](OTf)$ and $[Co^{III}(PY5Me_2)(CN)](OTf)_2$ are shown in figure 4.3. There is a sharp peak for C ≡ N vibrational at 2107 cm^{-1} and 2253 cm^{-1} for Co(II) and Co(III) complexes, respectively. Interestingly, the C ≡ N bond length from crystal structure indicates elongation of the bond from Co(II) to Co(III) complex which is counter-intuitive to general statement that longer bond length would result in low stretch frequency at same bond order. It was investigated in literature [15] that the C ≡ N stretch frequency increase from Co(II) to Co(III) is due to the force constant increase of the bond. This effect is quite common for cyano groups where back-donation from an electron rich acceptor is not possible. Because the coordination through the C lone pair made the N lone pair more Lewis basic, there is an increased electron donation from the N lone pair, adding more σ character to the bond upon oxidation of Co(II). Therefore, the force constant increases due to that the increased σ bond arises dominantly from donor s orbital. The other weak broad peak at 2300 cm^{-1} shown in figure 4.3b is from the CO_2 in the IR instrument and decreases with increasing N_2 purging time in the instrument chamber.

Table 4.2 Selected bond distances (Å) and angles (deg) for $[Co^{II}(PY5Me_2)(CN)]^{+}$ and $[Co^{III}(PY5Me_2)(CN)]^{2+}$.

Bond/Angle	Co(II)	Co(III)
Co-N1	1.977(2)	1.992(3)
Co-N2	2.138(3)	1.980(3)
Co-N3	2.088(3)	1.973(3)
Co-N4	2.127(3)	1.981(3)
Co-N5	2.066(3)	1.981(3)
Co-C1	1.913(3)	1.891(3)
C1-N6	1.128(1)	1.151(1)
N1-Co-C1	178.38(13)	179.68(14)
N2-Co-N4	175.10(11)	178.92(12)
N3-Co-N5	176.37(11)	178.66(11)
N2-Co-N3	84.21(10)	83.99(10)
N3-Co-N4	99.27(10)	96.65(11)
N4-Co-N5	81.58(11)	83.63(11)
N5-Co-N2	94.74(10)	95.76(11)
N1-Co-N2	88.00(10)	90.55(12)
N1-Co-N3	87.12(10)	89.30(11)
N1-Co-N4	88.73(10)	90.34(11)
N1-Co-N5	89.37(11)	89.38(11)

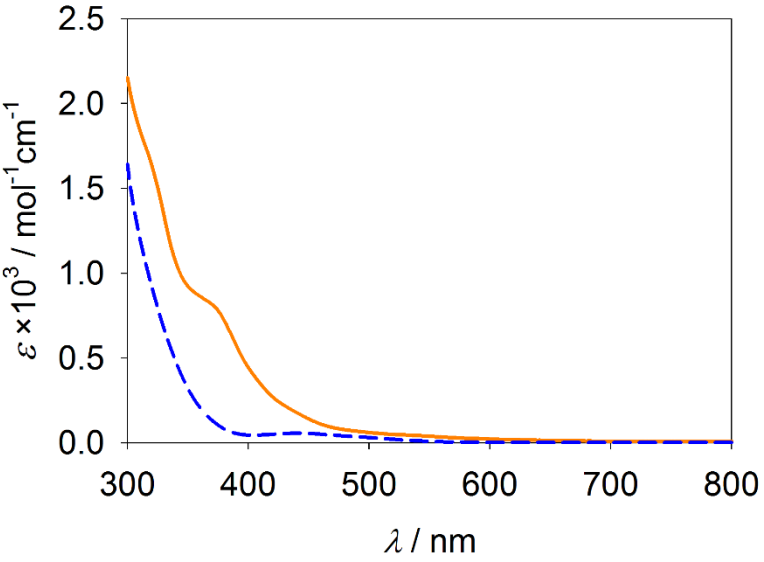

Figure 4.2 UV-vis spectra for complexes $[Co^{II}(PY5Me_2)(CN)]^{+}$ (orange solid) and $[Co^{III}(PY5Me_2)(CN)]^{2+}$(blue dash) in acetonitrile.

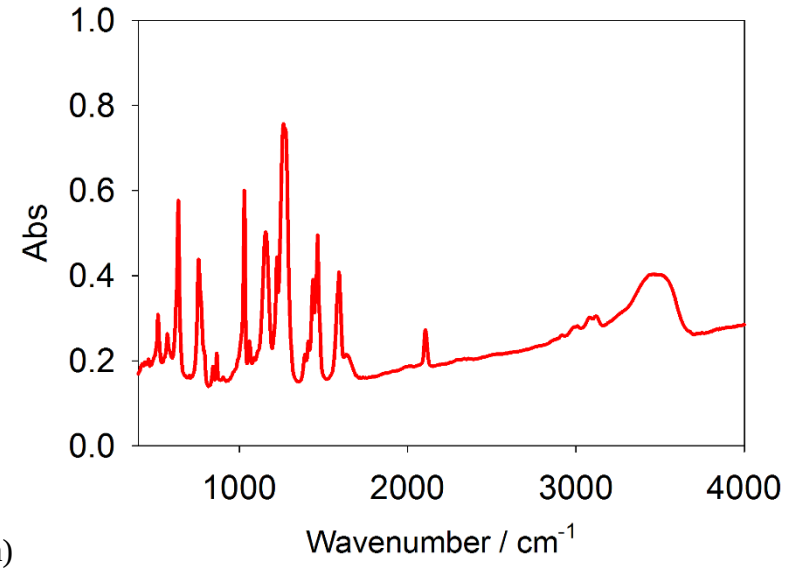

a)

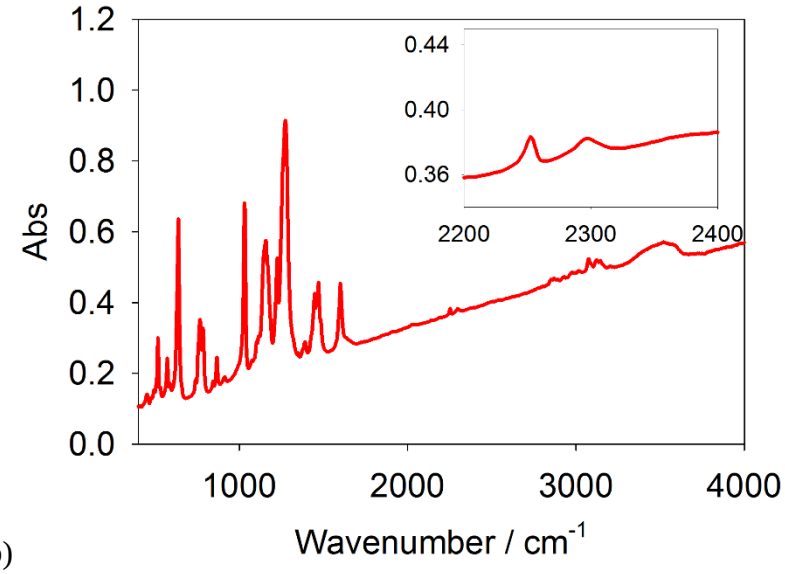

b)

Figure 4.3 Infrared spectrum of a) $[Co^{II}(PY5Me_2)(CN)]^{+}$ and b) $Co^{III}(PY5Me_2)(CN)]^{2+}$, KBr was used in sample preparation.

4.4.3 Spin state and reorganization energy

The magnetic susceptibility and spin state of the Co(II), $[Co(PY5Me_2)(CN)]^{+}$, was determined using Evans method by NMR in acetonitrile-D6. An effective magnetic moment value of ~1.8 μ_B

was obtained. A slightly higher value of ~2.4 μ_B for powdered sample was obtained using Evans balance. The results indicated a low spin state for the Co(II) in $[Co(PY5Me_2)(CN)]^+$. As mentioned in the discussions of crystal structures (4.4.1), the spin change from high spin Co(II) to low spin Co(III) would result significantly larger inner-sphere reorganization energy which is then represented as slower electron transfer rate as compared to low spin Co(II)/(III).[16] Reorganization energy and self-exchange rate constant was estimated using the information given by the crystal structures of $[Co(PY5Me_2)(CN)]^{2+/+}$, following literature reported method. [17–19]

The inner-sphere reorganization energy, λ_{in}, is the sum of the reorganization parameters of the individual reactants and can be described by the expression below.

$$\lambda_{in} = \frac{1}{2}\sum f_i (d_2^0 - d_3^0)_i^2$$

Where f_i is a reduced force constant for the *i*th inner-sphere vibration defined in terms of the normal-mode force constants of the two oxidation state, and $f_i = 2f_2f_3/(f_2+f_3)$, f_2 and f_3 are the breathing force constants of the two reactants ($f_i = 4\pi^2c^2\bar{\nu}_i^2\mu$, $\bar{\nu}_i$ is the stretching frequency in cm^{-1} and μ is the reduced mass in kg, c is the velocity of light in cm/s). $(d_2^0 - d_3^0)_i = \Delta d_0$ is the bond length change in the two oxidation states. The breathing frequency of Co-N bonds in Co(II) and Co(III) of the new redox shuttle, $[Co(PY5Me_2)(CN)]^{2+/+}$, were taken as 266 cm^{-1} and 378 cm^{-1} and a force constant of 170 N m^{-1} was used for Co-N bond.[19,20] Co-N force constant was assumed to be similar to cobalt tris-bipyridyl complexes here, though $Co(PY5Me_2)(CN)$ complexes had distorted octahedral structure, they had quite similar geometry as cobalt tris-bipyridyl complexes. The Co-N bond order is assumed to have little change between $PY5Me_2$ and bipyridyl ligand because even though the electron donor ability increased in $PY5Me_2$ owing to the -Me substituents, the multidentate feature could also leads to a slightly misalignment of orbital overlap between the

ligand and metal center. The average bond length change, Δd_0, for Co-N bonds is 0.113 Å. The Co-C bond force constant is 230 N m^{-1} which is adapted from $[Co(CN)_6]^{3-}$,[21] Δd_0(Co-C) is 0.022 Å. An inner-sphere reorganization of 0.67 eV is calculated using the values outlined above.

The outer-sphere reorganization energy in acetonitrile can be obtained from the dielectric continuum theory,[22]

$$\lambda_o = \frac{(\Delta z q)^2}{4\pi\varepsilon_0}\left(\frac{1}{a}-\frac{1}{R_e}\right)\left(\frac{1}{n_{sol}^2}-\frac{1}{\varepsilon_{sol}}\right)$$

where Δz is the change in charge of the cobalt complex after electron transfer, q is the charge of an electron, ε_o is the permittivity of free space, ε_{sol} is the static dielectric of acetonitrile (36) [23], n_{sol} is the refractive index of acetonitrile (1.3442)[24], a is the radius of the reactant, and R_e is the reactant center-to-center separation distance ($R_e = 2a$). The radii of $[Co(PY5Me_2)(CN)]^{2+/+}$ is 6 Å. An outer-sphere reorganization of 0.632 eV is thus calculated.

It is noted that the inner-sphere reorganization energy, λ_{in}, estimated for $[Co(PY5Me_2)(CN)]^{2+/+}$ is quite close to the outer-sphere reorganization energy, λ_o. An inner-sphere reorganization energy of 2.3 eV and outer-sphere reorganization energy of 0.610 eV for $[Co(bpy)_3]^{3+/2+}$ was also calculated in the same manner, which is in excellent agreement with literature reported value (λ_{in} =2.63 eV, λ_o = 0.58 eV). [25] In comparision, $[Co(bpy)_3]^{3+/2+}$ has a much larger inner-sphere reorganization energy than its outer-sphere reorganization energy. The decreased inner-sphere reorganization energy is apparently dominated by the smaller barrier of low spin ($t_{2g}^6e_g^1$) to low spin ($t_{2g}^6e_g^0$) electron transfer in $[Co(PY5Me_2)(CN)]^{2+/+}$, which resembles to low spin $[Co(ttcn)_2]^{3+/2+}$. It is already determined in literature that $[Co(ttcn)_2]^{3+/2+}$ has a self-exchange rate of ~ 9.1×10^3 M^{-1} s^{-1}, namely ~ 30000 times faster than $[Co(bpy)_3]^{3+/2+}$ in acetonitrile at 25 ^{0}C. A similar faster self-exchange rate constant as $[Co(ttcn)_2]^{3+/2+}$ could be a reasonable assumption for

$[Co(PY5Me_2)(CN)]^{2+/+}$. Since the self-exchange rate constant for outer-sphere electron transfer reactions can be effectively predicted using Marcus Theory, self-exchange rate constant of $[Co(PY5Me_2)(CN)]^{2+/+}$ is calculated using the expression below:[17,19,22,26]

$$k_{ex} = K_A \kappa_{el} \nu_n \Gamma e^{-\lambda_{se}/4k_B T}$$

where K_A is the equilibrium constant for the formation of the precursor complex of the reactants, κ_{el} and ν_n is electronic transmission coefficient and effective nuclear frequency respectively. Γ is the inner-sphere nuclear tunneling factor. λ_{se} ($\lambda_{se} = \lambda_{in} + \lambda_o$)is the total reorganization energy.

The value of K_A can be calculated from expression:

$$K_A = \frac{4\pi N_A r^2 \delta r}{1000} e^{(-w(r)/k_B T)}$$

where δ_r is typically equal to 0.8 Å[27] and *w(r)* is the work to bring the reactants to separation distance. A detailed calculation of work term has already been discussed in the appendix of chapter 3. The frequency factor ν_n is assumed to be 10^{12} s^{-1}, because $\nu_n \approx 10^{11}$ in the case of outer-sphere reorganization dominated electron transfer and $\nu_n \approx 10^{13}$ when inner-sphere dominated.[28] Assuming $\kappa_{el} \approx 1$(for adiabatic reactions) and $\Gamma \approx 1$(no significant tunneling contribution).[3,28]A value of 0.05 M^{-1} is calculated for K_A (at I = 0.2 M ionic strength) and a self-exchange rate of ~ 1.4×10^5 M^{-1} s^{-1} was calculated. Because the low spin $[Co(PY5Me_2)(CN)]^+$ complex is equatorially compressed ~ 0.13 Å and axially compressed ~0.04 Å compared to $[Co(PY5Me_2)(CN)]^{2+}$ complex due to Jahn-Teller distortion in d^7 electronic configuration. The estimation of inner-reorganization energy using the average bond length is therefore a crude estimation, and the λ_{se} may be higher than calculated which would lead to slower self-exchange

rate than calculated value, this fact holds true for $[Co(ttcn)_2]^{3+/2+}$. [3] It is noted in literature that the self-exchange rate constant calculated are found to be larger than that derived from Marcus cross relation experimentally.[29] Low spin $[Co(ttcn)_2]^{3+/2+}$ showed a self-exchange rate constant measured using Marcus cross relation via stop-flow technique to be about 2-3 order slower than values calculated as well as values determined from ^{59}Co NMR in aqueous medium.[3] Therefore, a self-exchange rate constant in acetonitrile ranging from ~1.4×10^3 to 1.4×10^4 M^{-1} s^{-1} for $[Co(PY5Me_2)(CN)]^{2+/+}$ is likely assuming a similar 2-3 order lower number from the calculated value, observed in aqueous medium. The estimated self-exchange rate constant of $[Co(PY5Me_2)(CN)]^{2+/+}$ is thus similar to the observed value for $[Co(ttcn)_2]^{3+/2+}$, which is about 3-4 order of magnitude faster compared to high spin cobalt redox shuttle, e.g. $[Co(bpy)_3]^{3+/2+}$.[25]

4.4.4 Electrochemistry

The complexes are characterized with electrochemical methods cyclic voltammetry, shown in figure 4.4. There is a reversible wave corresponding to Co(II)/Co(III) at $E_{1/2}$ = 0.230 V vs NHE ($E_{1/2}$ = 0.630 V vs NHE for ferrocene), which indicated a redox potential of 400 mV negative of $[Co(ttcn)_2]^{3+/2+}$ and 340 mV negative of $[Co(bpy)_3]^{3+/2+}$. As compared to the parent complex $[Co(PY5Me_2)(MeCN)]^{3+/2+}$ which has a redox potential of 0.803 V vs NHE,[4] the large negative shift of redox potential can be explained by the introduction of the anionic strong field ligand, -CN group, to the six coordination site. The effect was discussed in literature[5] that by changing the X ligand of a series complexes $[Fe(PY5)(X)]^{n+}$ (PY5=2,6-(bis(bis-2-pyridyl)-methoxymethan)pyridine), where X represented a series of exogenous mondentate ligands with different field strength, the potential of $[Fe(PY5)(X)]^{n+}$ complexes was tuned over a wide range from 0.74V to 1.36 V vs ferrocene. A reference potential shift was observed when CVs were taken with different sample mixtures, see figure 4.20 in the appendix. However, the redox potential of

$[Co(PY5Me_2)(CN)]^{2+/+}$ vs. ferrocene stay constant after correcting the mid potential of ferrocene, regardless of different sample mixtures. Therefore, the reference was dipped in a secondary container with glass frit. Supporting electrolyte solution was added to the secondary container. The reference is protected and no potential shift was observed in later measurements.

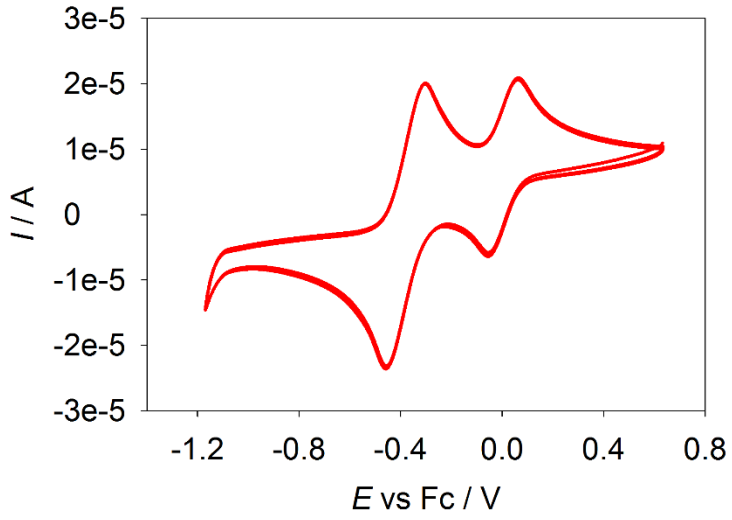

Figure 4.4 Cyclic voltammetry of $[Co(PY5Me_2)(CN)]^{2+/+}$ in acetonitrile. The measurements were performed with a glassy carbon disk electrode, Pt mesh counter electrode, Ag/AgNO3 reference electrode and 0.1 M $TBAPF_6$ (tetrabutylammonium=TBA) supporting electrolyte at a scan rate of 100 mV/s. Ferrocene was used as an internal standard, the redox wave at 0V is from ferrocene.

4.4.5 Photovoltaic performance

DSSCs are assembled using redox shuttles $[Co(PY5Me_2)(CN)]^{2+/+}$ and $[Co(bpy)_3]^{3+/2+}$. The *J* – *V* curves taken at 0.1 sun intensity and IPCEs are show in figure 4.5. The average short circuit photocurrent density (J_{sc}), open circuit photovoltage (V_{oc}) and fill factors (*ff*) derived from the *J*-*V* curves taken at both AM 1.5 illumination (100 mW cm^{-2}, 1 sun) and 0.1 sun of 8 cells are given in table 4.3. Under 1sun intensity, J_{sc}'s and V_{oc}'s of the $[Co(bpy)_3]^{3+/2+}$ cells are slightly higher than $[Co(PY5Me_2)(CN)]^{2+/+}$ cells. *ff* is quite close for both redox shuttles. Overall, the $[Co(bpy)_3]^{3+/2+}$ cells delivered better power conversion efficiencies than $[Co(PY5Me_2)(CN)]^{2+/+}$ cells at 1 sun

intensity. Current transients taken at 1 sun intensity later showed that the photocurrent for both redox shuttles are mass transport limited, see figure 4.8 in the appendix. The mass transport limitation can be attributed to the solvent choice made here. A mixture of 60% acetonitrile and 40% propylene carbonate was used as the electrolyte solvent. Propylene carbonate was added instead of using pure acetonitrile to increase the solubility of the $[Co(PY5Me_2)(CN)]^{2+/+}$ redox shuttle. However, propylene carbonate (viscosity σ = 1.9 mS cm^{-1}) is more viscous than acetonitrile (σ = 5.9 mS cm^{-1}), literature value showed that the diffusion coefficient of $[Co(bpy)_3]^{3+/2+}$ in propylene carbonate is an order of magnitude smaller than in acetonitrile.[30] Therefore, we attribute the more pronounced mass transport limitation to the electrolyte solvent we used here. Unlike the performance at 1sun intensity, the $[Co(PY5Me_2)(CN)]^{2+/+}$ cells showed 25% increase in J_{sc}'s to $[Co(bpy)_3]^{3+/2+}$ cells. The IPCE maximum at ~470 nm showed an increase from 28% ($[Co(bpy)_3]^{3+/2+}$) to 35% ($[Co(PY5Me_2)(CN)]^{2+/+}$), exhibiting the same trend as J_{sc} obtained at low light intensity, 0.1 sun.

Table 4.3 Average *J-V* characteristics of 8 DSSCs under simulated AM 1.5G illumination (100 mW cm^{-2}) and 0.1 sun (10 mW cm^{-2}). Pt counter electrodes are used here.

Redox	$[Co(bpy)_3]^{3+/2+}$	$[Co(PY5Me_2)(CN)]^{2+/+}$
	1sun	
η (%)	0.84 ± 0.23	0.70 ± 0.09
J_{sc} (mA cm^{-2})	2.66 ± 0.38	2.43 ± 0.45
V_{oc} (V)	0.51 ± 0.02	0.45 ± 0.01
FF	0.60 ± 0.08	0.65 ± 0.05
	0.1 Sun	
η (%)	0.83 ± 0.36	1.02 ± 0.05
J_{sc} (mA cm^{-2})	0.32 ± 0.06	0.39 ± 0.02
V_{oc} (V)	0.41 ± 0.06	0.39 ± 0.01
FF	0.60 ± 0.11	0.67 ± 0.01

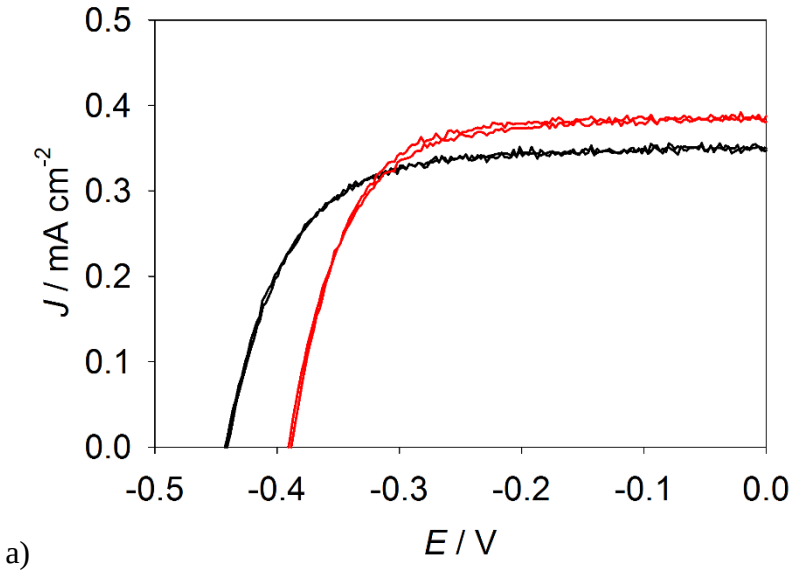

a)

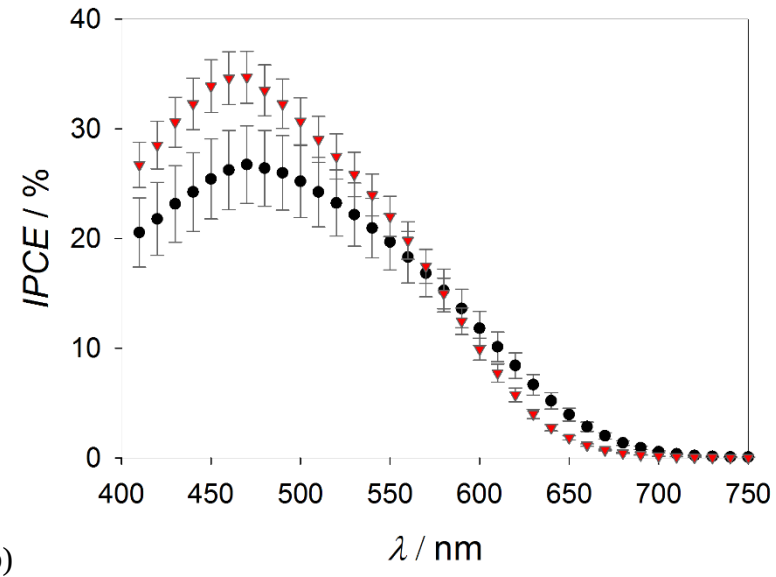

b)

Figure 4.5 a) Plots of representative *J* – *V* curves at 0.1 sun intensity and of DSSCs employing redox shuttles $[Co(PY5Me_2)(CN)]^{2+/+}$ (red) and $[Co(bpy)_3]^{3+/2+}$ (black). b) IPCEs curves of DSSCs with redox shuttles $[Co(PY5Me_2)(CN)]^{2+/+}$ (red triangle) and $[Co(bpy)_3]^{3+/2+}$ (black circle).The error bars are shown as the standard deviation of 8 cells in each condition. Pt counter electrodes are used here.

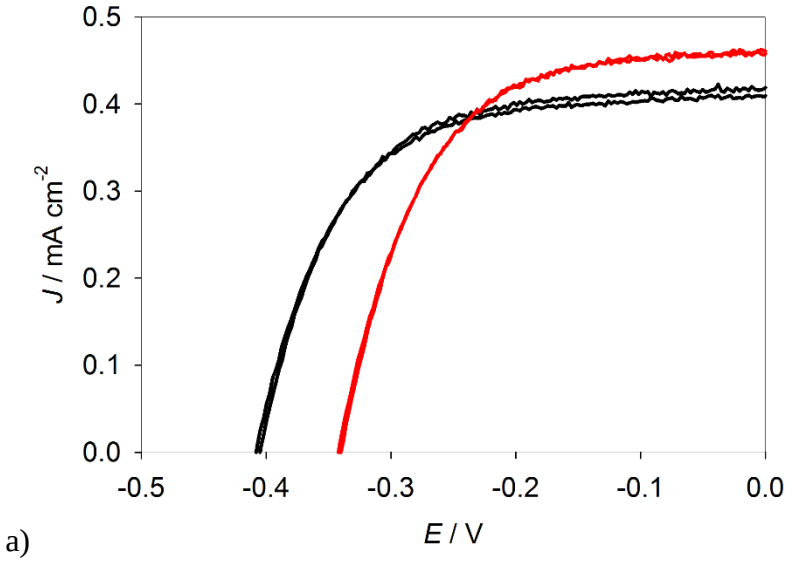

a)

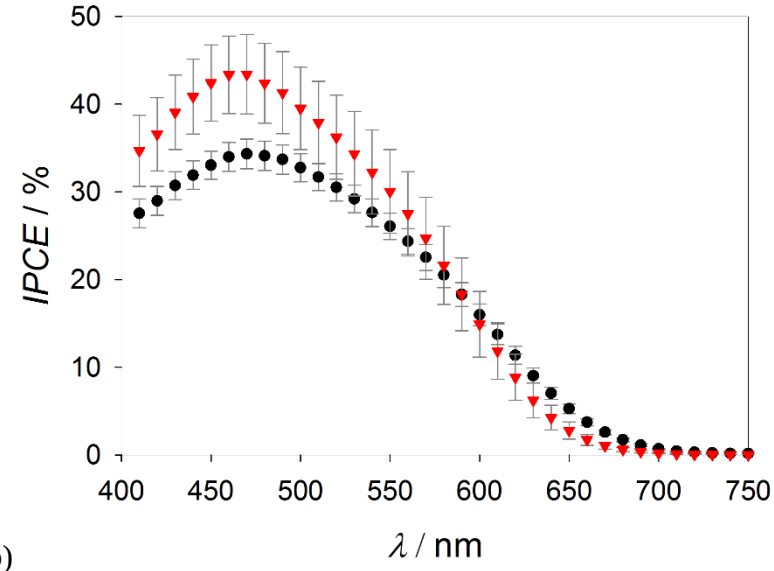

b)

Figure 4.6 a) Plots of representative *J* – *V* curves at 0.1 sun intensity and of DSSCs employing redox shuttles $[Co(PY5Me_2)(CN)]^{2+/+}$ (red) and $[Co(bpy)_3]^{3+/2+}$ (black). b) IPCEs curves of DSSCs with redox shuttles $[Co(PY5Me_2)(CN)]^{2+/+}$ (red triangle) and $[Co(bpy)_3]^{3+/2+}$ (black circle).The error bars are shown as the standard deviation of 8 cells in each condition. Graphene counter electrodes are used here.

Table 4.4 Average *J-V* characteristics of 8 DSSCs under simulated AM 1.5G illumination (100 mW cm^{-2}) and 0.1 sun (10 mW cm^{-2}). Graphene counter electrodes are used here.

Redox	$[Co(bpy)_3]^{3+/2+}$	$[Co(PY5Me_2)(CN)]^{2+/+}$
	1sun	
η (%)	0.95 ± 0.12	0.88 ± 0.13
J_{sc} (mA cm^{-2})	3.06 ± 0.08	3.27 ± 0.39
V_{oc} (V)	0.51 ± 0.02	0.44 ± 0.02
FF	0.61 ± 0.06	0.62 ± 0.06
	0.1 Sun	
η (%)	1.18 ± 0.13	1.05 ± 0.14
J_{sc} (mA cm^{-2})	0.41 ± 0.01	0.48 ± 0.04
V_{oc} (V)	0.43 ± 0.03	0.36 ± 0.02
FF	0.66 ± 0.03	0.61 ± 0.02

To further explore the effects of changing counter electrode, electrochemical impedance measurement of thin layer symmetric cell assembled using two same counter electrodes are taken to determine the electron transfer rate and diffusion coefficient of the two redox shuttles at both graphene and Pt counter electrodes, following literature reported methods. [31] The impedance plots and summary of parameters from EIS measurements are shown in the appendix, figure 4.10 and table 4.5 respectively. For both redox shuttles, $[Co(PY5Me_2)(CN)]^{2+/+}$ and $[Co(bpy)_3]^{3+/2+}$, they gave a similar diffusion coefficient of the Co(III) species at approximately 1.6×10^{-5} ~1.8×10^{-5} cm^2 s^{-1}, which can be attributed to similar molecule size and structures for both redox couples, 6 and 6.5 Å respectively. For $Co(PY5Me_2)(CN)]^{2+/+}$. the charge transfer resistance decreased slightly at graphene counter electrode, 2.3 Ω cm^2, compared to a value of 3.6 Ω cm^2at Pt counter electrode, , when using. However, R_{ct} increased from 0.6 to 2.5 Ω cm^2 when using $[Co(bpy)_3]^{3+/2+}$. The heterogeneous electron transfer rate constant can be deduced according to equation $k^0 = \frac{RT}{nFR_{ct}}(F \times C_{ox}^{\beta} \times C_{red}^{1-\beta})^{-1}$.[32] The rate constant deduced from R_{ct} again showed the same trend

as R_{ct} for both redox shuttles. The smaller charge transfer resistance and slightly faster heterogeneous electron transfer rate at graphene electrode indicated that graphene can be a better counter electrode for $[Co(PY5Me_2)(CN)]^{2+/+}$. Previous study on using graphene and nanoplatelets as electrocatalyst in $[Co(bpy)_3]^{3+/2+}$ mediated cells[33] showed that graphene nanoplatelets outperforms platinum at high solar intensities and gave comparable efficiencies at lower intensities due to an decrease on charge transfer resistance. Our result of photovoltaic improvement is in good agreement with literature, however, the discrepancy here on charge transfer resistance behavior for $[Co(bpy)_3]^{3+/2+}$ on graphene may be attributed to the thickness of the graphene layer deposited on FTO. Since the loading of graphene nanoplatelets is usually quantified by the optical transmission of the graphene layer at 550 nm. We found that the transmittance measured at 550 nm for the graphene electrode used here is ~ 92 %, see figure 4.9 in the appendix. However, the minimum transmittance value required is ~85 % for graphene counter electrode to outperform Pt counter electrode, which was investigated in literature.[10,33] Furthermore, earlier investigation of electrochemistry of polypyridine complexes of Co(II/III) in DSSCs by Sapp and Elliott also showed that the redox peak separation of $[Co(bpy)_3]^{3+/2+}$ is slightly larger on glassy carbon electrode than on platinum, owing to slightly slower electron transfer kinetics on glassy carbon, presumably on other carbon based materials as well.[34] Cyclic voltammetry study on various electrode materials (glassy carbon, Pt, gold) for the two redox couples was measured and the plots are shown in figure 4.11 in the appendix. $[Co(PY5Me_2)(CN)]^{2+/+}$ presented little dependence on the working electrode materials, whereas $[Co(bpy)_3]^{3+/2+}$ showed same result as literature[34] that electron transfer kinetic are less favored on glassy carbon than Pt and gold. These results demonstrated the advantages that cheap carbon based counter electrode materials can be utilized for $[Co(PY5Me_2)(CN)]^{2+/+}$. The DSSCs performance can be improved for $[Co(PY5Me_2)(CN)]^{2+/+}$

by using graphene counter electrode. Furthermore, more understanding on regeneration and recombination is needed to illustrate the better performance observed for $[Co(PY5Me_2)(CN)]^{2+/+}$ in comparison to $[Co(bpy)_3]^{3+/2+}$. Detailed discussions on the effect of reorganization energy and electron transfer rate on regeneration and recombination are included in below sections.

Table 4.5 Summary of charge transfer resistance R_{ct}, standard heterogeneous electron transfer rate constant deduced from R_{ct} and Co(III) diffusion coefficient at 0V from EIS for $[Co(PY5Me_2)(CN)]^{2+/+}$ and $[Co(bpy)_3]^{3+/2+}$at graphene and pt counter electrode. Raw Nyquist plots from EIS are included in the appendix, figure 4.9.

Redox shuttle	Graphene			Pt		
	R_{ct} (Ω cm^2)	k_0 (cm s^{-1})	D_0 (cm^2 s^{-1})	R_{ct} (Ω cm^2)	k_0 (cm s^{-1})	D_0 (cm^2 s^{-1})
$[Co(bpy)_3]^{3+/2+}$	2.5	2.4×10^{-3}	1.7×10^{-5}	0.6	0.010	1.6×10^{-5}
$[Co(PY5Me_2)(CN)]^{2+/+}$	2.3	2.8×10^{-3}	1.8×10^{-5}	3.6	1.6×10^{-3}	1.8×10^{-5}

4.4.6 Recombination and charge collection

The lifetimes plots of $[Co(PY5Me_2)(CN)]^{2+/+}$ and $[Co(bpy)_3]^{3+/2+}$ are shown in figure 4.7. Electrochemical impedance spectroscopy measurements were also taken which gives similar values of lifetime, τ_n, see figure 4.19 in the appendix. The lifetime of $[Co(PY5Me_2)(CN)]^{2+/+}$ is approximately ~100 times longer than $[Co(bpy)_3]^{3+/2+}$ at same applied potential. It was previously determined that the rate constant for recombination to $[Co(ttcn)_2]^{3+}$ is 10 times larger than $[Co(bpy)_3]^{3+}$.[25] The lifetime of $[Co(PY5Me_2)(CN)]^{2+/+}$ would be ~1000 time longer than $[Co(ttcn)_2]^{3+/2+}$. Because electrons generated near the back contact need to travel shorter distance compared to electrons generated far from the back contact to be collected, the IPCE ratio of different illumination direction can indicate the charge collection length qualitatively. Larger IPCE ratio indicates longer diffusion length and better charge collection. The near identical IPCE ratio at different illumination direction implies that $[Co(PY5Me_2)(CN)]^{2+/+}$ and $[Co(bpy)_3]^{3+/2+}$ may

have similar charge collection efficiency at short circuit, see figure 4.12 in the appendix. The charge collection efficiency of $[Co(PY5Me_2)(CN)]^{2+/+}$ would improve compared to $[Co(ttcn)_2]^{3+/2+}$ here.

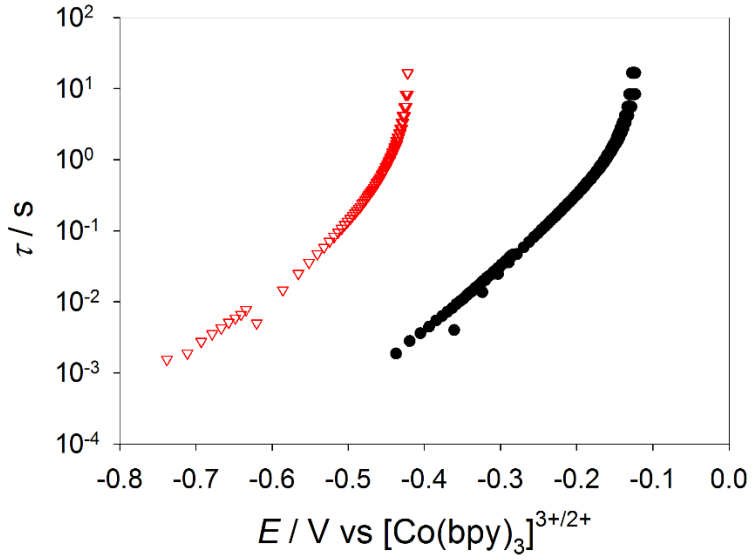

Figure 4.7 Plots of lifetimes vs potential for $[Co(PY5Me_2)(CN)]^{2+/+}$ (red triangles) and $[Co(bpy)_3]^{3+/2+}$ (black circles) redox shuttles from open circuit voltage decay measurements.

Since the charge collection is a function of diffusion length and electron lifetime, and the electron lifetime can be described as the ratio of surface electron concentration to the recombination rate, *U*. Therefore, analysis of electron recombination rate allows us the elucidate the charge collection in DSSCs. Assuming recombination is dominated by electron transfer from conduction band to the oxidized form of the redox shuttle, Co(III). The recombination rate can be expressed as equation, $U = [Co(III)] n_s k_{et}$, Where k_{et} is the recombination rate constant, which can be described with Marcus theory using equation:

$$k_{et} = k_{et,\max} e^{-\left(\Delta G^0 + \lambda_{et}\right)^2 / 4\lambda_{et} k_B T}$$

where $-\Delta G^0$ is the driving force of the electron transfer and λ_{et} is the reorganization energy associated with the electron transfer, $\lambda_{et} = \lambda_{in}/2 + \lambda_{o,sc}$ ($\lambda_{o,sc}$, is the reorganization energy semiconductor-liquid interface). The prefactor, $k_{et,max}$, is the rate constant at optimal exoergicity, obtained when $-\Delta G^0 = \lambda_{et}$. In addition, $k_{et,max}$ has a weak dependence on the reorganization energy ($k_{et,max} \propto \lambda_{et}^{-1/2}$). The driving force is the difference between the conduction band energy, E_{cb}, and the formal potential of the redox shuttle. The recombination rate constant of low spin $[Co(ttcn)_2]^{3+/2+}$ and high spin $[Co(bpy)_3]^{3+/2+}$ was previously determined to be about 6×10^{-17} and 6×10^{-18} cm^4 s^{-1} respectively.[25] The one order of magnitude faster recombination rate of low spin $[Co(ttcn)_2]^{3+/2+}$ than high spin $[Co(bpy)_3]^{3+/2+}$ is resulted from a smaller inner-sphere reorganization energy and a larger recombination driving force. Fast recombination and poor charge collection limited the cell performance of $[Co(ttcn)_2]^{3+/2+}$.[25] In comparison, the low spin redox shuttle $[Co(PY5Me_2)(CN)]^{2+/+}$ has a ~ 0.4 eV less recombination driving force. A ~ 6 times smaller recombination rate constant (~1×10^{-17} cm^4 s^{-1}) of $[Co(PY5Me_2)(CN)]^{2+/+}$ than $[Co(ttcn)_2]^{3+/2+}$ was estimated according to the above equation assuming a similar reorganization energy as $[Co(ttcn)_2]^{3+/2+}$. If compared to $[Co(bpy)_3]^{3+}$, there is ~1.5 times smaller rate constant for electron recombination to $[Co(PY5Me_2)(CN)]^{2+}$. A comparable diffusion length and recombination rate at open circuit condition (where IPCEs are taken) can be reasonably assumed between $[Co(PY5Me_2)(CN)]^{2+/+}$ and $[Co(bpy)_3]^{3+/2+}$, provided that same Co(III) concentration is used in the electrolyte. This is in general good agreement with the observed similar IPCE ratio for both $[Co(PY5Me_2)(CN)]^{2+/+}$ and $[Co(bpy)_3]^{3+/2+}$.

However, an inner-sphere reorganization energy, $\lambda_{in,}$ value of 0.67 eV is calculated using bond length changes from single crystal X-ray diffraction data and force constants for $[Co(PY5Me_2)(CN)]^{2+/+}$ in section *4.4.3*. The calculated λ_{in} value is much smaller compared to a

measured λ_{in} value of 1.38 eV for $[Co(ttcn)_2]^{3+/2+}$. The outer-sphere reorganization energy at TiO_2 surface, $\lambda_{o,sc}$, value, can be calculated using equation (15) from literature.[35] The calculation gave a value of 0.417 eV for $[Co(PY5Me_2)(CN)]^{2+/+}$ which is slightly smaller than a calculated of 0.543 eV for $[Co(ttcn)_2]^{3+/2+}$ owing to slightly larger molecule diameter. If the above theoretically calculated value of λ_{in} = 0.67 eV for $[Co(PY5Me_2)(CN)]^{2+/+}$ and $\lambda_{o,sc}$ = 0.417 eV were used for calculating recombination rate constant, k_{et}, a recombination rate of 8×10^{-17} cm^4 s^{-1} was obtained. In comparison to $[Co(ttcn)_2]^{3+/2+}$, the recombination rate constant increases which is on contrary to the previously estimated smaller value of ~1×10^{-17} cm^4 s^{-1} assuming $[Co(PY5Me_2)(CN)]^{2+/+}$ would have a similar reorganization energy of λ_{et} = 0.75 eV as $[Co(ttcn)_2]^{3+/2+}$. Noted that the driving force of electron recombination to $[Co(PY5Me_2)(CN)]^{2+}$ is ΔG^0 = 0.77eV which is slightly larger than the total reorganization energy calculated here at TiO_2, λ_{et} = 0.75 eV, this is still in the Marcus normal region. As mentioned above, it is also a crude estimation of λ_{in} using average bond length change because the strong Jahn-Teller distortion effect induced uneven bond length change in the complex. The estimated λ_{in} = 0.67 eV maybe an underestimation for $[Co(PY5Me_2)(CN)]^{2+/+}$. Measuring rate constant experimentally using Marcus cross relation would allow a more accurate determination of reorganization energy and further elucidate whether the electron recombination to $[Co(PY5Me_2)(CN)]^{2+}$ falls into the inverted region or not which might account for the longer electron lifetime observed. Control experiments using redox shuttle $[Co(ttcn)_2]^{3+/2+}$ could also produce a more direct analysis of the dependence of interfacial electron transfer rate constants on the reorganization energy and driving force which are originated from fine-tuned structure in $[Co(PY5Me_2)(CN)]^{2+/+}$.

4.4.7 Regeneration

The regeneration efficiency is determined by the branching ratio of dye regeneration and recombination as given by:

$$\eta_{reg} \cong \frac{[R]k_{reg}}{[R]k_{reg} + n_s k_{rec}} \tag{13}$$

where [*R*] is the concentration of the reduced form of the redox shuttle, n_s is the surface electron concentration in TiO_2, k_{reg} is the dye regeneration rate constant and k_{rec} is a rate constant reflecting recombination from TiO_2 to the oxidized dye.[36] We assume that n_s is constant at low light intensity, and k_{rec} is same when same dye, D35cpdt, is used for both redox shuttles, $[Co(PY5Me_2)(CN)]^{2+/+}$ and $[Co(bpy)_3]^{3+/2+}$. Since the redox shuttles investigated herein are one-electron outer-sphere redox couples, the rate constant for dye regeneration can be described using the Marcus cross relation, thus the relative rates of regeneration can be simplified by taking the ratio of the redox shuttle self-exchange rate constants and equilibrium constants as described in previous reports:[22,25]

$$\frac{k_{reg,cn} = \sqrt{k_{33}K_{D/cn}}}{k_{reg,bpy} = \sqrt{k_{22}K_{D/bpy}}}$$

where $K_{D/cn}$ and $K_{D/bpy}$ are the equilibrium constants for the dye (*D*) regeneration reactions with $[Co(PY5Me_2)(CN)]^{2+/+}$ and $[Co(bpy)_3]^{3+/2+}$, respectively. The equilibrium constants are determined from the potential difference of the dye and redox shuttles according to equation $nF\Delta E = RT \ln K_{D/redox}$, where *n* is the number of electrons transferred (*n* = 1), *F* is Faraday's constant, ΔE is the formal potential difference between the oxidant and reductant in solution, *R* is the gas constant and *T* is the temperature. The regeneration driving force is 0.506 eV and 0.846 eV for $[Co(bpy)_3]^{3+/2+}$ and $[Co(PY5Me_2)(CN)]^{2+/+}$ respectively. Based on estimation of self-exchange rate constants of $[Co(PY5Me_2)(CN)]^{2+/+}$ (~1.4×10^3 to 1.4×10^4 M^{-1} s^{-1}) and measured self-exchange rate as well as calculated equilibrium constants, the regeneration rate constant with $[Co(PY5Me_2)(CN)]^{+}$ is therefore expected to be ~5×10^4 to 2×10^5 times larger than $[Co(bpy)_3]^{2+}$.

It is reported that the regeneration efficiency for DSSCs using $[Co(bpy)_3]^{3+/2+}$ is ~0.54 in the same condition investigated here. Thus an increase in regeneration efficiency to unity can be expected in cells using $[Co(PY5Me_2)(CN)]^{2+/+}$. Since IPCE can be expressed as:

$$IPCE(\lambda) = \eta_{LH}(\lambda)\eta_{cc}(\lambda)\eta_{Inj}(\lambda)\eta_{reg}(\lambda)$$

where η_{LH} is the light harvesting efficiency, η_{inj} is the electron injection efficiency, and η_{cc} is the charge collection efficiency, a relative 85% (equal to (1-0.54)/0.54) increase in IPCE may be expected in $[Co(PY5Me_2)(CN)]^{2+/+}$ with respect to $[Co(bpy)_3]^{3+/2+}$. However, as shown in figure 4.6, there is only ~28% (equal to (45-35)/35) relative increase in IPCE at maximum from $[Co(bpy)_3]^{3+/2+}$ (~35%) to $Co(PY5Me_2)(CN)]^{2+/+}$ (~45%). We also found that the performance of $[Co(PY5Me_2)(CN)]^{2+/+}$ cells degrades after aging overnight while the cell performance commonly improves for most electrolyte to date including $[Co(bpy)_3]^{3+/2+}$. The UV-vis spectrum of fresh and aged electrolyte containing $[Co(PY5Me_2)(CN)]^{2+/+}$ shows a bleach at absorption bands corresponded to MLCT of $[Co(PY5Me_2)(CN)]^{+}$ at 350-450 nm, see figure 4.13 in the appendix. No significant change after aging was observed for electrolyte containing $[Co(bpy)_3]^{3+/2+}$. We therefore attribute the lower than expected IPCE to the loss of reduced form in cells using $[Co(PY5Me_2)(CN)]^{2+/+}$ which may be associated with the stability of $[Co(PY5Me_2)(CN)]^{+}$ as a result of disassociation of –CN group. Further study on the stability of $[Co(PY5Me_2)(CN)]^{+}$ and direct measurement of self-exchange rate constant is needed for a more detailed explanation such as aging electrolyte in an inert atmosphere and avoid contact of oxygen and moisture during cell assembly. Though the performance of $[Co(PY5Me_2)(CN)]^{2+/+}$ is affected by stability issue of the reduced form which experimentally decreases regeneration efficiency, a 28% relative increase in IPCE is stilled observed. In addition to improved charge collection, these results further demonstrated the promise in producing efficient DSSCs using $[Co(PY5Me_2)(CN)]^{2+/+}$ via

quantitative regeneration if consideration are taken to overcome the possible stability issue of the reduced form. Adding electrolyte additives would also be beneficial for increasing the overall performance.

4.5 Conclusions

We have demonstrated a way to effectively control the spin state and redox potential of cobalt redox shuttles via introducing strong field ligand with high donor ability. Reorganization energy estimated for the complexes here indicated a small energy barrier can be expected for the self-exchange, yielding a reasonable guess of rate constant ~1.4×10^3 to 1.4×10^4 M^{-1} s^{-1} for $[Co(PY5Me_2)(CN)]^{2+/+}$. Better photovoltaic performance in DSSCs was obtained for $[Co(PY5Me_2)(CN)]^{2+/+}$ compared to high spin cobalt redox shuttle, $[Co(bpy)_3]^{3+/2+}$, in conjunction with D35cpdt dye. Electrochemistry analysis on the counter material also revealed that the new complex $[Co(PY5Me_2)(CN)]^{2+/+}$ is favored to cheap abundant carbon based material, e.g. graphene. Further discussion on regeneration and recombination rate using Marcus theory also suggested that quantitative regeneration was achieved for $[Co(PY5Me_2)(CN)]^{2+/+}$ in addition to improved charge collection. These findings are important that it opens up choices of better energy match between the redox shuttle and dyes with quite negative ground state potentials, such as osmium based sensitizers (~0.7 V vs NHE) which also absorbs to the near IR. There is about ~0.4 eV dye regeneration driving force to the osmium based sensitizers by utilizing $[Co(PY5Me_2)(CN)]^{2+/+}$, quantitative regeneration may also be expected due to the fast self-exchange rate and potentially enough driving force. In addition, a plethora of the anionic or neutral strong field ligand can be introduced to the axial coordination site in the complex to control the spin state and redox potential. Moreover, adding electron withdrawing or donating substitutes to the PY5 ligand is also feasible

to tune the redox potential.[5,37] Therefore, a wide range of regeneration driving force can be obtained for efficient DSSCs design.

APPENDIX

APPENDIX

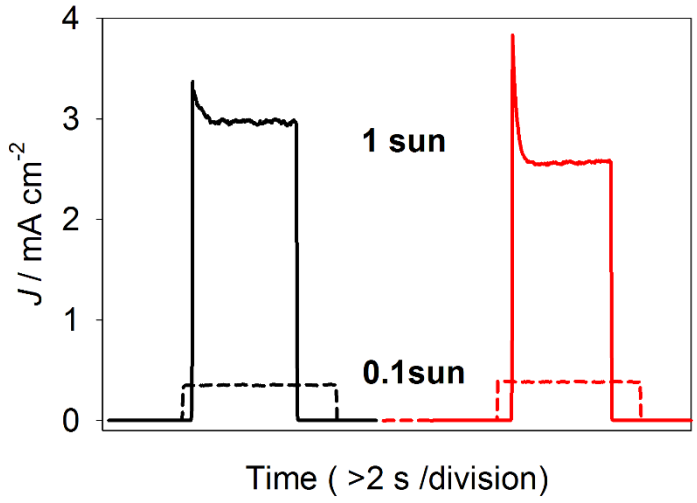

Figure 4.8 Current transients for DSSCs using $[Co(bpy)_3]^{3+/2+}$ (black) and $[Co(PY5Me_2)(CN)]^{2+/+}$.

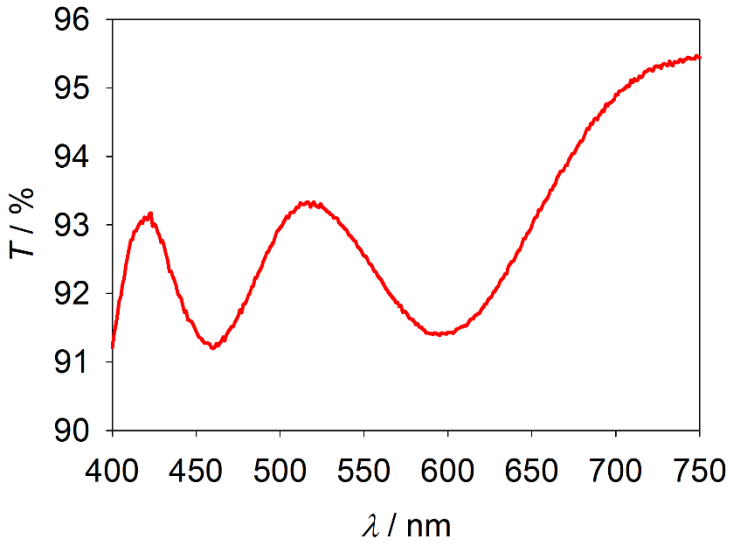

Figure 4.9 Transmittance of graphene naonplatelet layer deposited on FTO substrate.

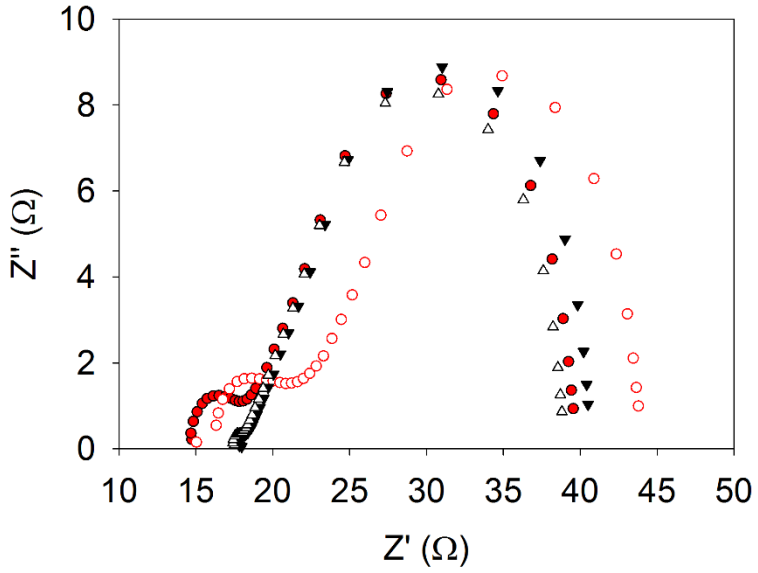

.a)

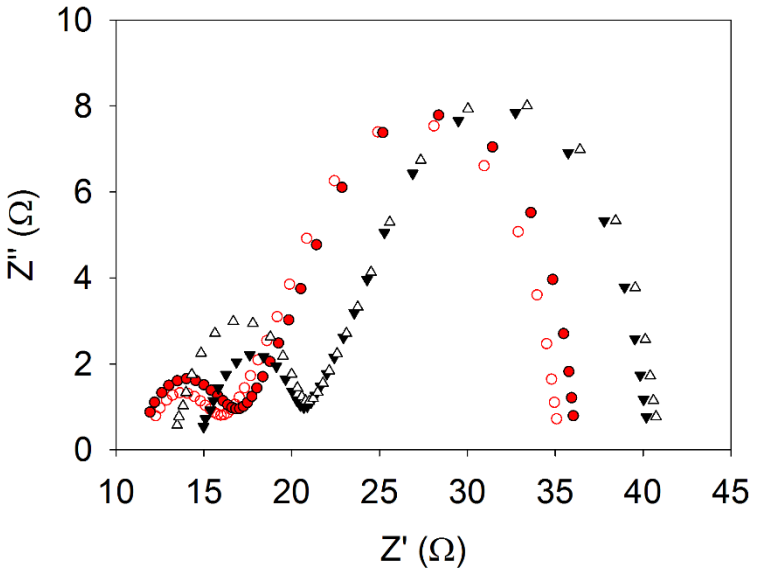

b)

Figure 4.10 Electrochemical impedance plots measured from symmetric thin layer cells using of a) $[Co(bpy)_3]^{3+/2+}$ and b) $[Co(PY5Me_2)(CN)]^{2+/+}$, the red circles and black triangles represent graphene and Pt based cells respectively, solid and hollow symbols are plots from parallel cells.

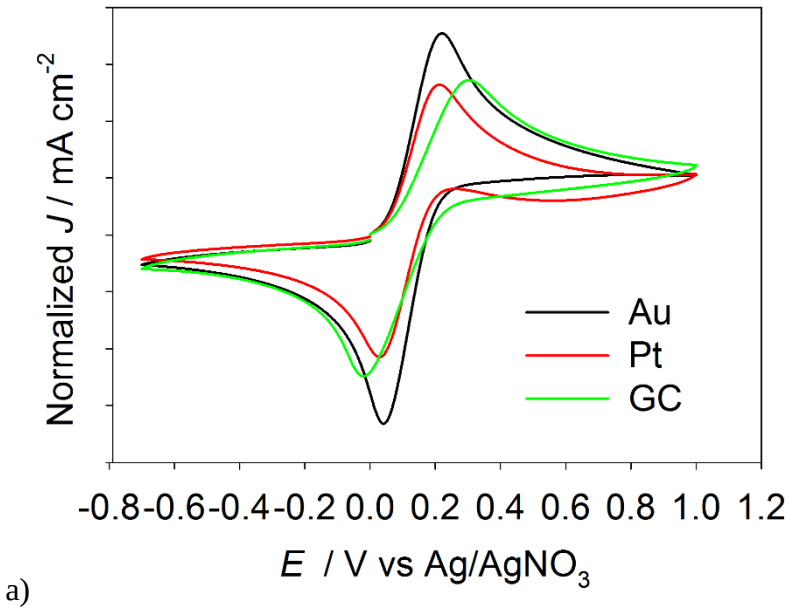

a)

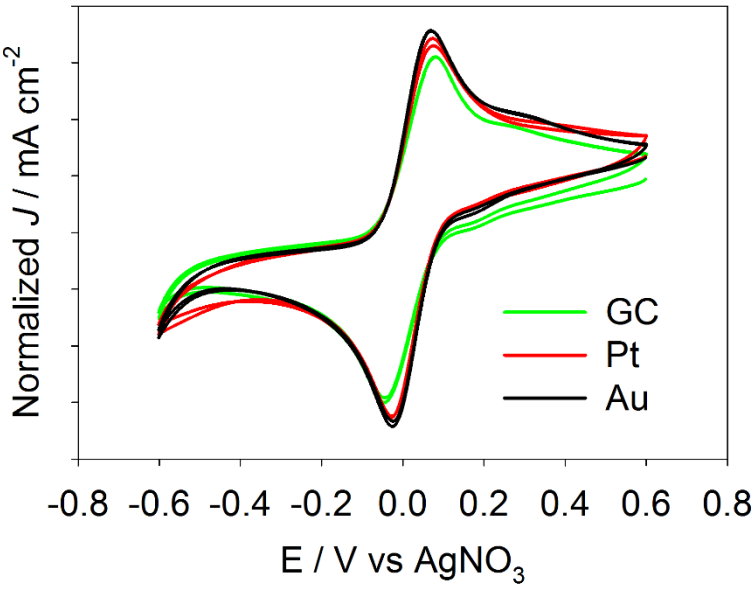

b)

Figure 4.11 Cyclic voltammogram of a) $[Co(bpy)_3]^{3+/2+}$ and b) $[Co(PY5Me_2)(CN)]^{2+/+}$ at various working electrode surface. Glassy carbon (Green), Pt (red), gold (black).

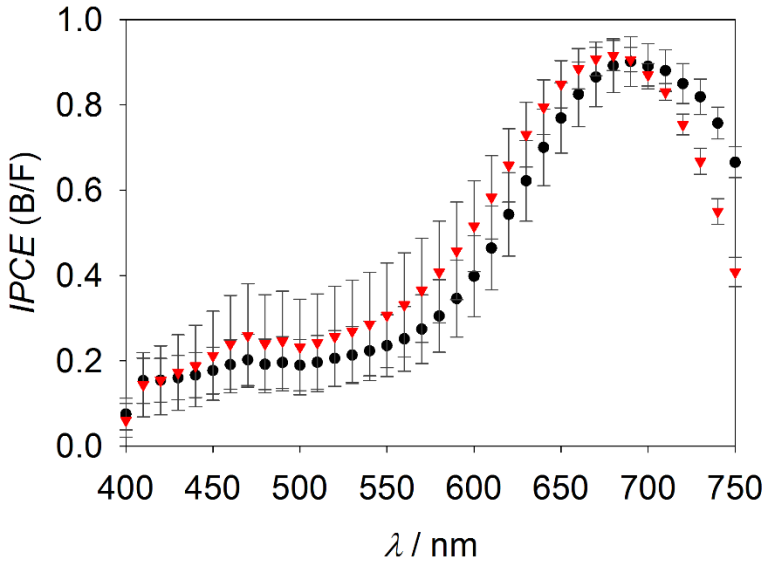

Figure 4.12 Plots of IPCE ratio at back side illumination and front side illumination for $[Co(PY5Me_2)(CN)]^{2+/+}$ (red triangle) and $[Co(bpy)_3]^{3+/2+}$ (black circle) redox shuttles.

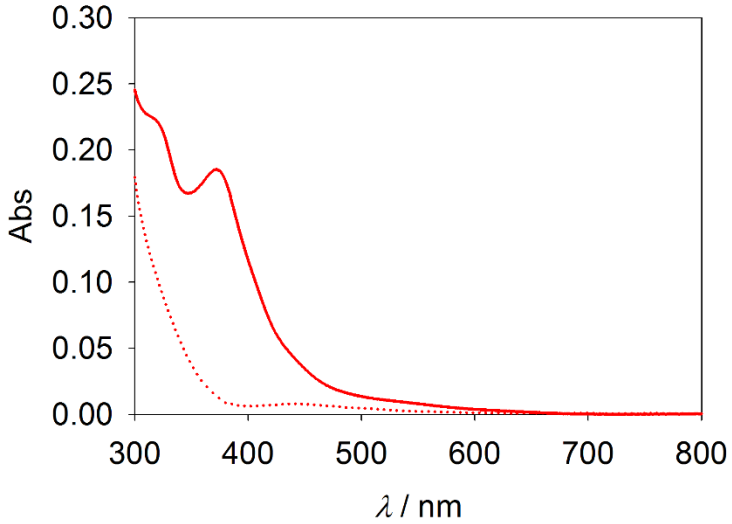

Figure 4.13 UV-vis spectra for fresh (solid) and aged (dashed) $[Co^{II}(PY5Me_2)(CN)]^{2+/+}$ containing electrolyte.

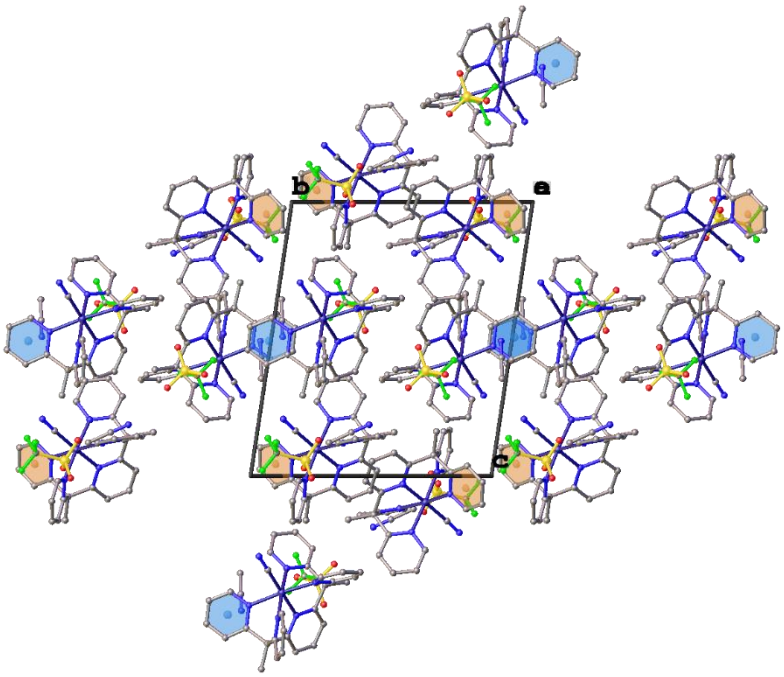

a)

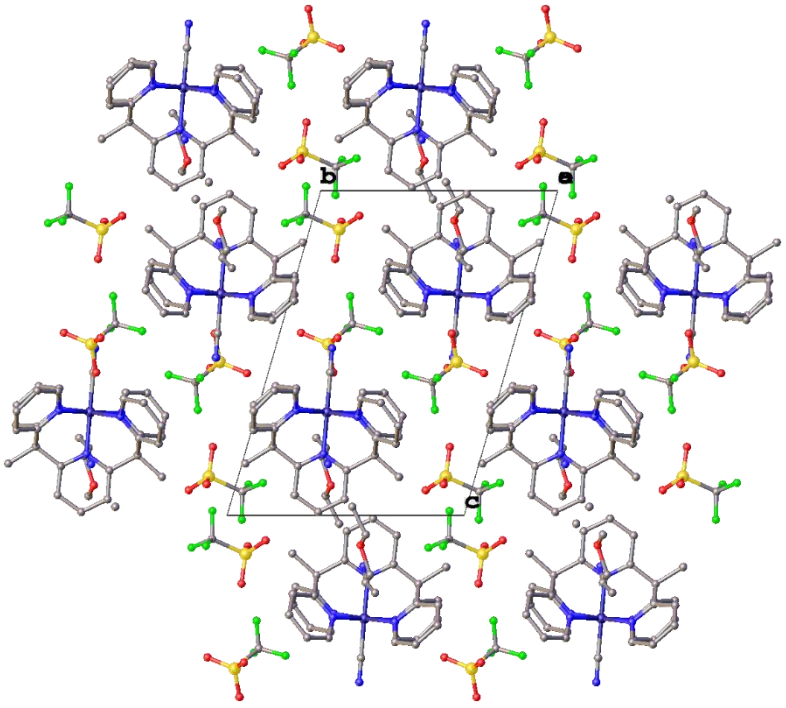

b)

Figure 4.14 Packing diagram of a)$[Co(PY5Me_2)(CN)]^+$ b)$[Co(PY5Me_2)(CN)]^{2+}$. There are two complex molecules in a unit cell, a molecule radius of 6 Å was estimated from the volume of the unit cell considering interested molecule as sphere spatially.

Table 4.6 Average *J-V* characteristics of 8 DSSCs under simulated AM 1.5G illumination (100 mW cm^{-2}) and 0.1 sun (10 mW cm^{-2}). Pt counter electrodes and chenodeoxylcholilc acid electrolyte additive are used here.

Redox	**$[Co(bpy)_3]^{3+/2+}$**	**$[Co(PY5Me_2)(CN)]^{2+/+}$**
	1sun	
η (%)	0.35 ± 0.12	0.56 ± 0.10
J_{sc} (mA cm^{-2})	1.32 ± 0.08	2.20 ± 0.25
V_{oc} (V)	0.44 ± 0.02	0.41 ± 0.01
FF	0.61 ± 0.06	0.62 ± 0.03
	0.1 Sun	
η (%)	0.99 ± 0.18	1.58 ± 0.11
J_{sc} (mA cm^{-2})	0.41 ± 0.01	0.67 ± 0.02
V_{oc} (V)	0.39 ± 0.01	0.36 ± 0.01
FF	0.61 ± 0.09	0.65 ± 0.01

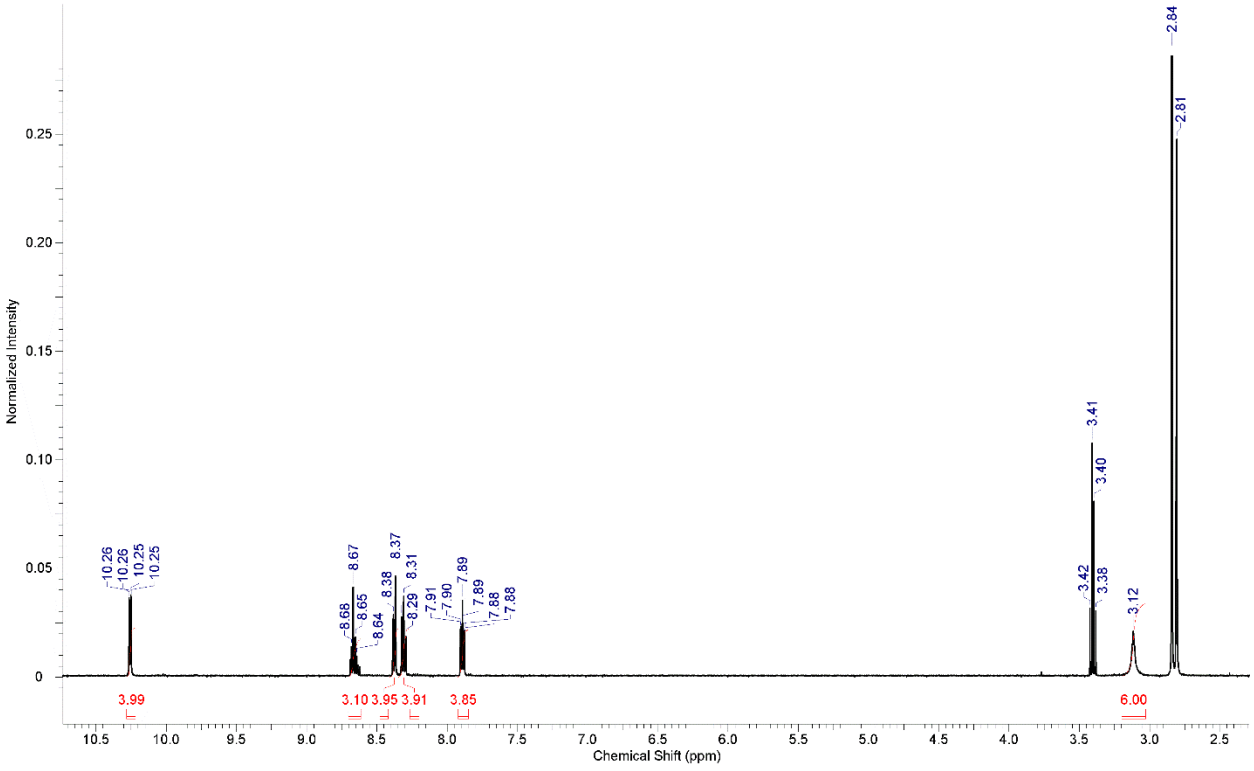

Figure 4.15 H^1NMR of $[Co(PY5Me_2)(CN)](OTf)_2$ in aceton-D6.

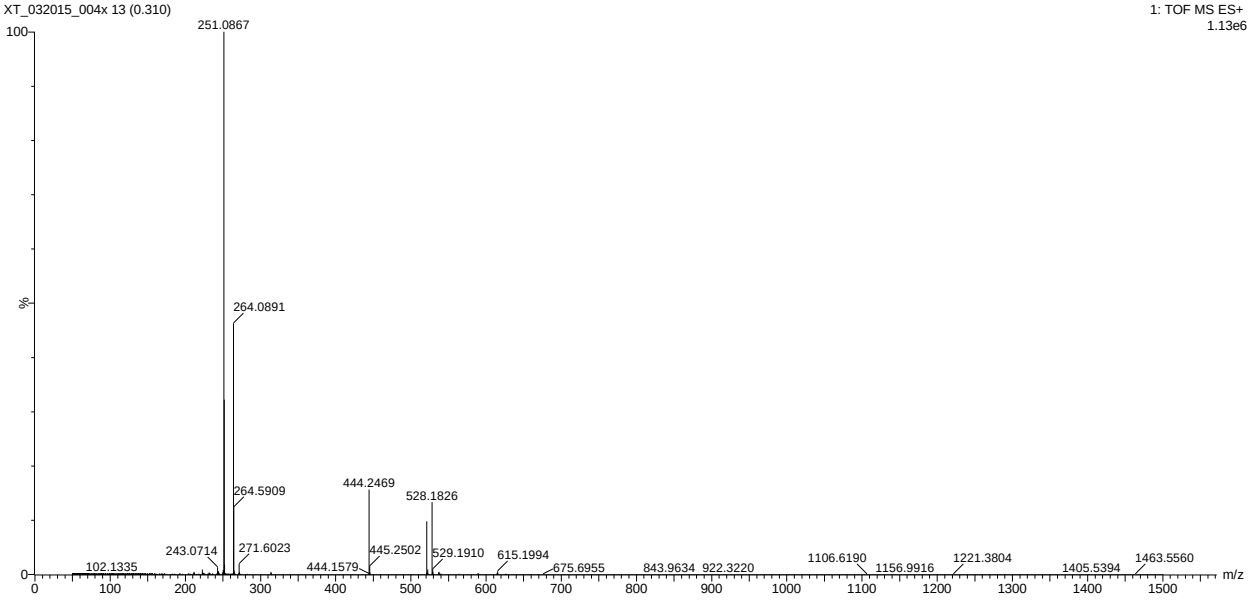

Figure 4.16 Mass spectra of [Co(PY5Me$_2$)(MeCN)](OTf)$_2$.

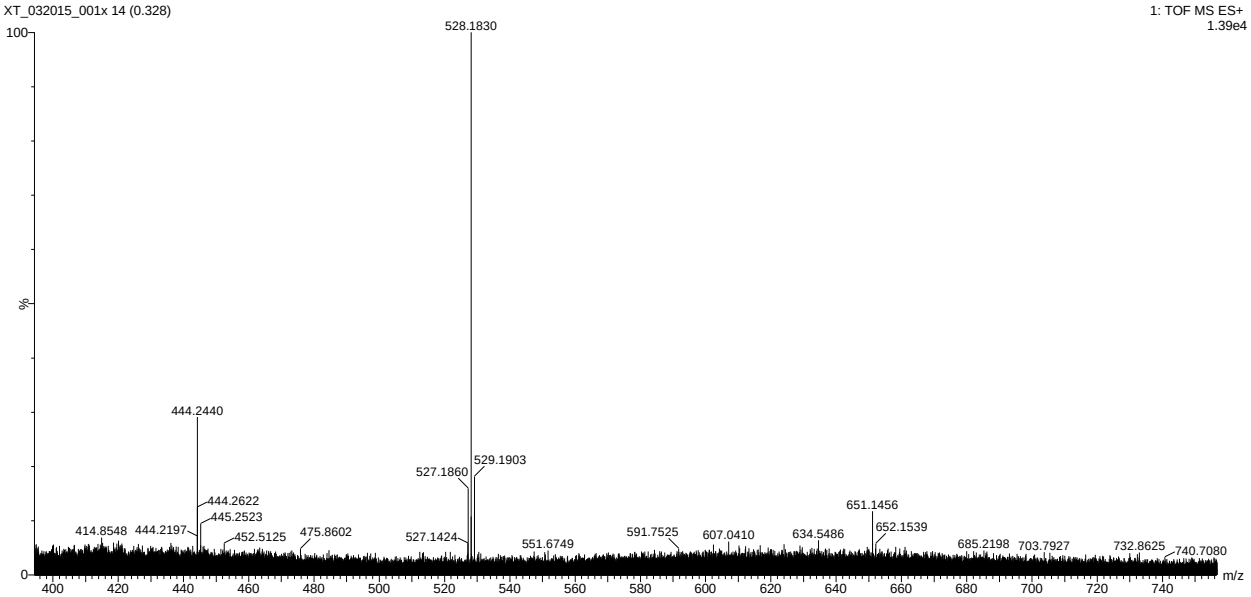

Figure 4.17 Mass spectra of [Co(PY5Me$_2$)(CN)](OTf).

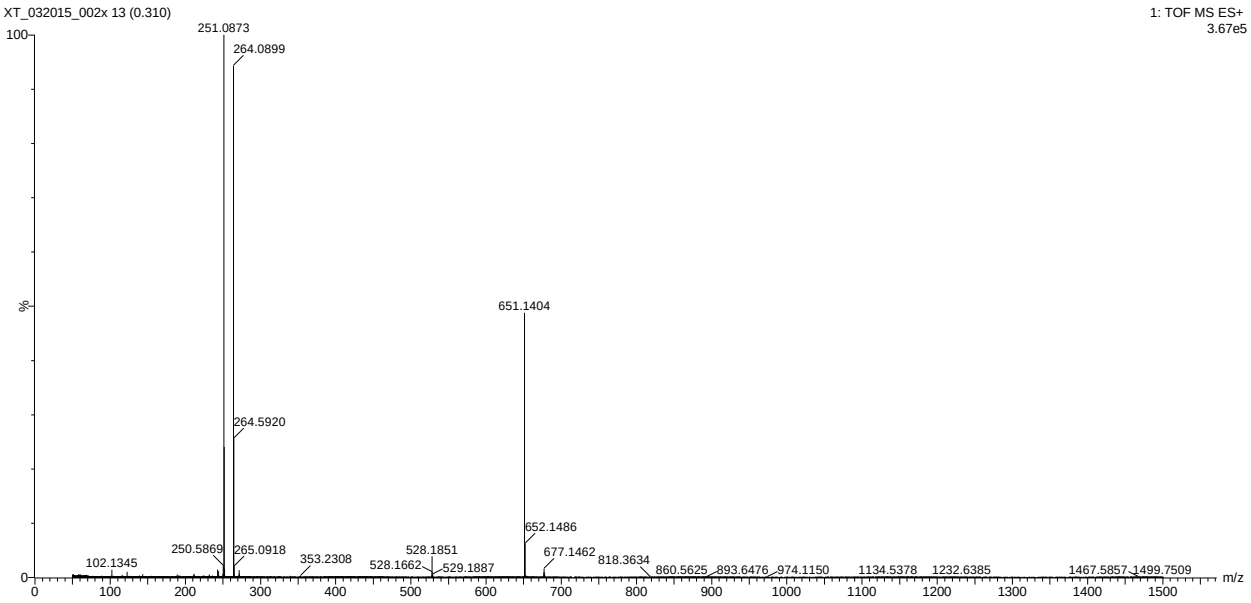

Figure 4.18 Mass spectra of $[Co(PY5Me_2)(CN)](OTf)_2$.

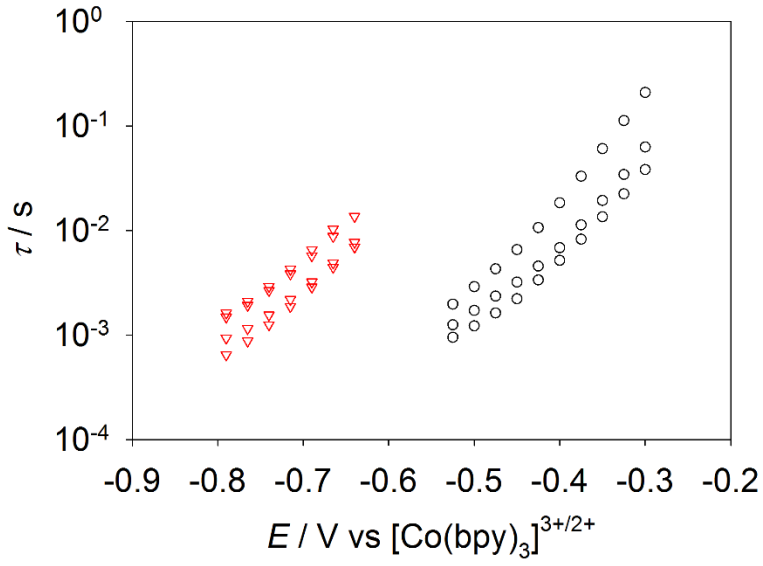

Figure 4.19 Plots of lifetimes vs potential for $[Co(PY5Me_2)(CN)]^{2+/+}$ (red triangles) and $[Co(bpy)_3]^{3+/2+}$ (black circles) redox shuttles from electrochemical impedance measurements.

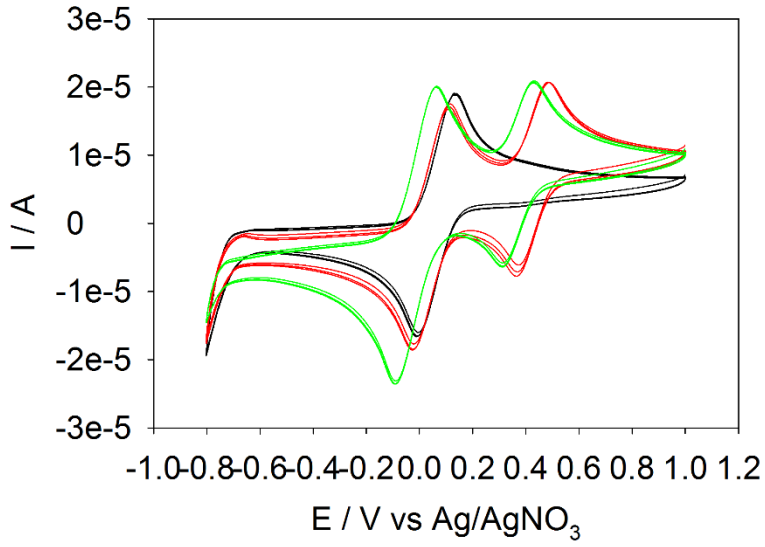

Figure 4.20 Cyclic voltammetry of [Co(PY5Me$_2$)(CN)](OTf) (black), [Co(PY5Me$_2$)(CN)](OTf) + ferrocene mixture (red), [Co(PY5Me$_2$)(CN)](OTf) + [Co(PY5Me$_2$)(CN)](OTf)$_2$ + ferrocene mixture (green) in acetonitrile. The measurements were performed with a glassy carbon disk electrode, pt mesh counter electrode, Ag/AgNO3 reference electrode and 0.1 M TBAPF$_6$ (tetrabutylammonium=TBA) supporting electrolyte at a scan rate of 100 mV/s.

REFERENCES

REFRENCES

(1) Chandrasekhar, S. .; McAuley, A. *Inorg. Chem.* **1992**, *31*, 480–487.

(2) Osvath, P.; Sargeson, A. M.; Skeltonb, B. W.; Whiteb, A. H. *J. Chem. Soc., Chem. Commun.* **1991**, 1036–1038.

(3) Kuppers, H.; Neves, A.; Pomp, I. C.; Ventur, D.; Wieghardt, I. K. *Inorg. Chem.* **1986**, *6*, 2400–2408.

(4) Kashif, M. K.; Axelson, J. C.; Du, N. W.; Forsyth, C. M.; Chang, C. J.; Long, R.; Spiccia, L.; Bach, U. *J. Am. Chem. Soc.* **2012**, *134*, 16646–16653.

(5) Goldsmith, C. R.; Jonas, R. T.; Cole, A. P.; Stack, T. D. P. *Inorg. Chem.* **2002**, *41*, 4642–4652.

(6) Xie, Y.; Hamann, T. W. *J. Phys. Chem. Lett.* **2013**, *4*, 328–332.

(7) Ünal, E. A.; Wiedemann, D.; Seiffert, J.; Boyd, J. P.; Grohmann, A. *Tetrahedron Lett.* **2012**, *53*, 54–55.

(8) Dixon, N. E.; Lawrance, G. a; Lay, P. a; Sargeson, A. M. *Inorg. Synth.* **2006**, *28*, 70–76.

(9) King, A. E.; Surendranath, Y.; Piro, N. a.; Bigi, J. P.; Long, J. R.; Chang, C. J. *Chem. Sci.* **2013**, *4*, 1578–1587.

(10) Kavan, L.; Yum, Jun, H.; Nazeeruddin, Nohammad, K.; Grätzel, M. *ACS Nano* **2011**, *5*, 9171–9178.

(11) Evans, D. F. *J. Chem. Soc.* **1959**, 2003–2005.

(12) Schubert, E. M. *J. Chem. Educ.* **1992**, *69*, 62.

(13) Yao, C.; Yao, J. *Z. Krist. Cryst.Struct.* **2005**, *220*, 483–484.

(14) Du, M.; Zhao, X.; Cai, H. *Z. Krist. Cryst.Struct.* **2004**, *219*, 463–465.

(15) Shifts, V. F. *J. Am. Chem. Soc.* **1966**, *667*, 247–250.

(16) Weaver, M. J.; Yee, E. L. *Inorg. Chem.* **1980**, *19*, 1936–1945.

(17) Brunschwig, B. S.; Sutin, N. *Coord. Chem. Rev.* **1999**, *18*, 233–254.

(18) Brunschwig, B. S.; Logan, J.; Newton, M. D.; Sutin, N. *J. Am. Chem. Soc.* **1980**, *102*, 5798–5809.

(19) Brunschwig, B. S.; Creutz, C.; Macartney, D. H.; Sham, T.-K.; Sutin, N.; May, R. *Faraday Discuss. Chem. Soc.* **1982**, *74*, 113–127.

(20) Szalda, D. J.; Creutz, C.; Mahajan, D.; Sutin, N. *Inorg. Chem.* **1983**, *22*, 2372–2379.

(21) Nakagawa, I. *Bull. Chem. Soc. Jpn.* **1973**, *46*, 3690–3693.

(22) Marcus, R. A.; Sutin, N. *Biochim. Biophys. Acta - Rev. Bioenerg.* **1985**, *811*, 265–322.

(23) Blomgren, G. E. In *Non-aqueous Electrochemistry*; Aurbach, D., Ed.; Marcel Dekker: New York, NY, 1999; pp 53–79.

(24) *CRC Handbook of Chemistry and Physics, 81st ed*, 81st ed.; Lide, D. R., Ed.; CRC Press: Boca Raton, FL, 2001.

(25) Xie, Y.; Baillargeon, J.; Hamann, T. W. *J. Phys. Chem. C* **2015**, *119*, 28155-28166.

(26) Marcus, R. A. *J. Phy. Chem.* **1990**, *94*, 1050–1055.

(27) Sutin, N. *Acc. Chem. Res.* **1982**, *15*, 275–282.

(28) Hamann, T. W.; Gstrein, F.; Brunschwig, B. S.; Lewis, N. S. *J. Am. Chem. Soc.* **2005**, *127*, 13949–13954.

(29) Chou, M.; Creutz, C.; Sutin, N. *J. Am. Chem. Soc.* **1977**, *99*, 5615–5623.

(30) Cabral, D.; Howlett, P. C.; Pringle, J. M.; Zhang, X.; MacFarlane, D. *Electrochim. Acta* **2015**, *180*, 419–426.

(31) Liberatore, M.; Petrocco, a.; Caprioli, F.; La Mesa, C.; Decker, F.; Bignozzi, C. a. *Electrochim. Acta* **2010**, *55*, 4025–4029.

(32) Bard, A. J.; Faulkner, L. R. *Electrochemical Methods: Fundamentals and Applications*, 2nd ed.; John Wiley & Sons, Inc., 2001.

(33) Kavan, L.; Yum, J.-H.; Grätzel, M. *Nano Lett.* **2011**, *11*, 5501–5506.

(34) Sapp, S. a; Elliott, C. M.; Contado, C.; Caramori, S.; Bignozzi, C. a. *J. Am. Chem. Soc.* **2002**, *127*, 11215–11222.

(35) Ondersma, J. W.; Hamann, T. W. *J. Am. Chem. Soc.* **2011**, *133*, 8264–8271.

(36) Hamann, T. W.; Ondersma, J. W. *Energy Environ. Sci.* **2011**, *4*, 370-381.

(37) Sun, Y.; Bigi, J. P.; Piro, N. a.; Tang, M. L.; Long, J. R.; Chang, C. J. *J. Am. Chem. Soc.* **2011**, *133*, 9212–9215.

Chapter 5 Regeneration and recombination in cyclometalated ruthenium dyes sensitized solar cells employing cobalt redox shuttles

* Dr. Suraj Somen is acknowledged for synthesis and characterization of the cyclometalated Ruthenium dyes.

5.1 Abstract

A series of cyclometalated ruthenium dyes, [Ru(dnbpy)(dcbpy)(ppy)](PF_6) (ss-14) and [Ru(dnbpy)(dcbpy)(dFppy)](PF_6) (ss-22) (dnbpy = 4,4'-dinonyl-2,2'-bipyridine; dcbpy = 2,2'-bipyridine-4,4'-dicarboxylic acid; ppy = 2-phenylpyridine; dFppy = 2-(2,4-difluorophenyl)pyridine), synthesized and characterized in our lab was incorporated with cobalt-based redox shuttles, $[Co(dmbpy)_3]^{3+/2+}$, for application in DSSCs. The DSSCs performance demonstrate that introduction of a blocking nonyl group can increase the lifetime however also inhibits regeneration caused by the ground state negative shift. Further addition of fluorine group in the phenylpyridine ligand improved the efficiency gained from increased dye regeneration driving force. Adding an ALD coating of alumina layer between the TiO_2 electrode and the sensitizers suppressed recombination process and improved the overall cell performance for all sensitizers studied. Here we established an approach to produce high efficiencies through systematic dye design, combined with electrode modification.

5.2 Introduction

Dye sensitized solar cells, DSSCs, first invented by O'Regan and Grätzel in 1991,[1] is one of the most promising second generation photovoltaics in harnessing solar energy for its great potential in cost-effective production for future applications. A typical DSSCs is composed of a platinum counter electrode and a photoanode, which consists of a dye sensitized thin mesoporous nanoparticle film of a wide band gap semiconductor deposited on a transparent conductive oxide

(TCO) substrate, surrounded by an electrolyte containing redox shuttles and additives. The electron transfer processes in DSSCs are illustrated in figure 5.1, upon photo-excitation of the dye molecules absorbed on semiconductor surface, one electron is injected into the conductor band followed by electron diffusion through the nanoparticle framework to the back contact at TCO, the oxidized dye was further regenerated by the reduced form of redox shuttles. Diffusion of the oxidized form of the redox shuttle to be reduced at the counter electrode thus completes the circuit. These processes compete with several unfavorable processes that reduce DSSCs efficiency including decay of the dye excited state as well as electron recombination to the oxidized dye or the oxidized form of the redox shuttle. The overall kinetic of a DSSC is complex that varying any component would involve several processes which can affect the overall DSSCs performances. [2] Photosensitizer, plays a key role contributing to the overall external quantum efficiency through efficient light harvest, electron injection and suitable energy level match with redox shuttles for efficient regeneration – which are determined by the kinetic pathways displayed in figure 5.1. In the champion DSSCs, the kinetics have been optimized to produce near quantitative injection, regeneration and charge collection. One path to improve the efficiency is therefore to utilize redox mediators with more positive potentials that are capable of improving the open circuit photovoltage, V_{OC}. It was such a strategy that lead to the recent record DSSC efficiencies which employed a cobalt tris-bipyridine, $[Co(bpy)_3]^{3+/2+}$, redox mediator and exhibited $V_{OC} > 1$ V.[3] Effective utilization of outersphere redox mediators, however, require the concomitant use of sensitizers designed to block recombination to the oxidized form of the mediator while maintaining good dye regeneration efficiencies. For example, a zinc porphyrin sensitizer was used with $[Co(bpy)_3]^{3+/2+}$ in order to achieve the recent record efficiency.[4]

Despite the excellent performance, porphyrin sensitizers are tedious to make with typical yields below 25 % and it is difficult to tune the ground and excited state energetics to match alternative redox mediators. The vast majority of other champion dyes reported in literature are derivatives of the paradigmatic N3 dye, $[Ru(dcbpy)_2(NCS)_2]$, where dcbpy = 2,2'-bipyridine-4,4'-dicarboxylic acid.[5] However, the parent compound, N3, is limited by both regeneration and recombination while incorporated with cobalt-based redox shuttles, we have demonstrated that the derivative Z907, $[Ru(dcbpy)(dnbpy)(NCS)_2]$, where dnbpy = 4,4'-dinonyl-2,2'-bipyridine, is compatible with fast redox shuttles due to the steric hindered nonyl groups on bpy in reducing recombination acting as a barrier between redox shuttles and semiconductor surface.[6,7] For Z907, the HOMO energy level is partially delocalized over the NCS^- ligands, however, which limits the ability to tune the ground state potential. Since alternative redox shuttles may have a wide variety of formal potentials, which should be matched to a given sensitizer to produce quantitative regeneration with a minimal wasted driving force, it is desirable to have a methodology to systematically control the HOMO energy as well as the sterics. In addition, the loss of labile NCS^- ligands has been implicated in long-term degradation of cells.[8] One way to introduce tunability in Z907 type sensitizers is to substitute cyclometalated chelating bidentate ligands in place of the monodentate NCS^- ligands.[9,10,11,12] Such cyclometalated ruthenium dyes have their highest occupied molecular orbit (HOMO) extended over the metal and anionic phenyl ring thus enabling its modulation through judicious installation of substituents on the phenyl ring.[13] However, the studies on the regeneration and recombination kinetics of cyclometalated Ru sensitized DSSCs using cobalt based redox shuttles are limited. Here we studied the DSSCs performances of a series cyclometalated analogs of Z907: $[Ru(ppy)(dnbpy)(dcbpy)](PF_6)$ (ss-14) and $[Ru(dFppy)(dnbpy)(dcbpy)](PF_6)$ (ss-22), dFppy = 2-(2,4-difluorophenyl)pyridine employing redox shuttles, $[Co(dmbpy)_3]^{2+/3+}$, where dmbpy is 4,4'-

dimethyl-2,2'-bipyridine, allowing us to elucidate the blocking effect of the nonyl chain on reducing recombination and providing slightly positive dye ground state potential, also the effect of adding fluorine atom on ppy in providing more dye regeneration driving force for better understanding the regeneration and recombination processes incorporating cobalt redox shuttles and cyclometalated sensitizers.

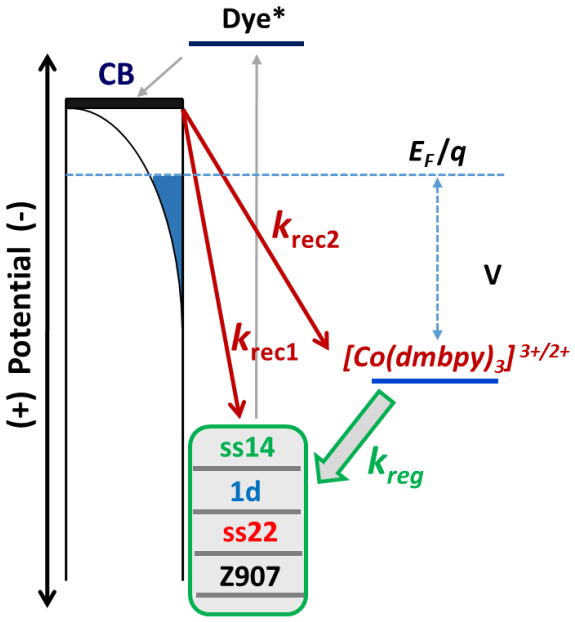

Figure 5.1 Energy diagram of a DSSC which shows the relevant kinetic processes involving redox shuttles, $[Co(dmbpy)_3]^{3+/2+}$, and series of cyclometalated Ruthenium dyes. dye regeneration (k_{reg}), recombination to the oxidized dye (k_{rec1}) and recombination to the Co(III) redox species (k_{rec2}).

5.3 Experimental

All reagents and Z907 dye were purchased from Sigma Aldrich and used as received unless stated otherwise. Photoelectrodes were prepared following the same procedure described in chapter 2.3. Briefly, a transparent TiO_2 nanoparticle layer was prepared by doctor blading a paste of ~15-20 nm TiO_2 nanoparticles (Ti-Nanoxide T/SP, Solaronix). A scattering TiO_2 nanoparticle

layer was prepared by doctor blading a paste of > 100 nm TiO_2 nanoparticles (Ti-Nanoxide D/SP, Solaronix) on top of the transparent film. The resulting electrodes were annealed at 325 ^oC for 5 min, 375 ^oC for 5 min, 450 ^oC for 5 min, 500 °C for 15 min in air. The resultant TiO_2 film thickness, *d*, was measured using a Dektak3 Surface Profiler to be ~10 μm. In some cases, as noted in the text, alumina was deposited immediately following removal from the oven by ALD using trimethylaluminum (TMA, Aldrich) and water as precursors. The TiO_2 electrodes were heated to 500 ^oC for 30 min, cooled to 100 ^oC, and immersed in dye solution (0.3 mM solution of dyes and 3mM chenodeoxycholic acid in ethanol). After 20-24 hours, the electrodes were rinsed with acetonitrile. A ~25 μm thick Surlyn frame (Solaronix) was sandwiched between the TiO_2 nanoparticle electrode and a platinized FTO electrode, and light pressure was applied at 150 ^oC to seal the cell. Electrolyte was filled by capillary force through the two pre-drilled holes on the platinum counter electrode, and sealed with microglass and Surlyn film. The electrolyte composition applied in all DSSCs contained 0.2M $Co(dmbpy)_3(TFSI)_2$, 20mM $Co(dmbpy)_3(TFSI)_3$, 0.1 M LiTFSI and 10mM cheno in acetonitrile.

Photoelectrochemical measurements were performed with an Autolab PGSTAT potentiostat interfaced with a Xe Arc Lamp. An AM 1.5 solar filter was used to simulate sunlight at 100 mW cm^{-2}. An additional 400 nm long-pass filter was used to prevent direct excitation of the TiO_2 in all light measurements. A Horiba Jobin Yyon MicroHR was used for monchromatic light for IPCE measurements.

5.4 Results and discussion

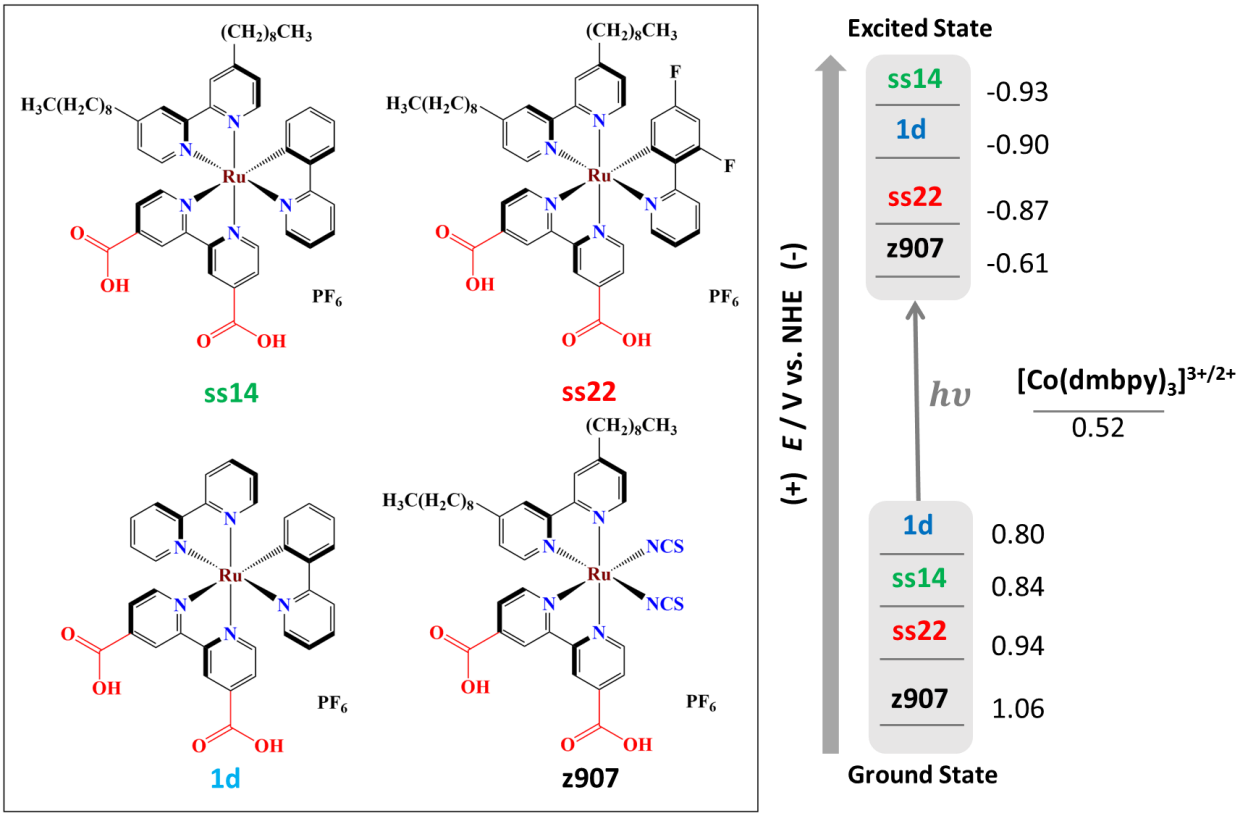

Figure 5.2 Structures and ground state, excited state energy levels of cyclometalated ruthenium dyes discussed in the chapter.

Figure 5.2 illustrates the ground state energy level of the dyes examined herein with respect to the $[Co(dmbpy)_3]^{3+/2+}$ redox potential, which is 0.52 V vs. NHE. Thus the friving force for dye regeneration ranges from 270 to 540 mV for this dye series. The performance of DSSCs sensitized with dye 1d, ss-14, ss-22 and z907 using $[Co(dmbpy)_3]^{2+/3+}$ based electrolyte containing 0.2M reduced redox shuttle, 0.02M oxidized redox shuttle, 0.1M LiTFSI, 10mM Chenodeoxycholic acid ($TFSI^-$: bis(trifluoromethane)sulfonamide anion) was studied under AM 1.5G sun illumination condition. Batches of three cells for each dye were prepared and measured on five different days, thus providing a sample set of 15 cells each. While there were variations of the performance from day-to-day which we attribute to variations of the TiO_2 nanoparticle electrode which were prepared

from different batches of TiO_2 with somewhat different film thicknesses, etc., the trends of the dye in a given batch were very consistent. However, the following results are taken from a representative batch of cells. Figure. 5.3 shows plots of current density, *J*, versus applied voltage, V_{app}, curves averaged for 3 cells as well as representative electron lifetime plots. The ss-14 sensitized cells produce a similar (within error) short circuit photocurrent density (J_{sc}) and open circuit photovoltage (V_{oc}) as the 1d sensitized cell. It is surprising that the addition of nonyl-groups (ss-14) has essentially no effect on the photovoltaic performance compared to 1d, despite the somewhat longer electron lifetime due to the increased steric hindrance, and hence diffusion length. This can be offset by a lower dye regeneration yield, however, since the ground state potential of ss-14 is slightly more negative than 1d. The cells sensitized with ss-22, which has the same steric advantage of ss-14, but with a 140 mV larger regeneration driving force, produced twice the photocurrent compared to ss-14 and 1d, as well as a ~40mV larger Voc. While there was a slight increase in electron lifetime for ss-22compared to ss-14, the cause of which is not clear since they are so structurally similar, we attribute the primary cause of the increased performance of ss-22 to a better dye regeneration yield. The performance of the Z907 sensitized cells an even higher photocurrent than ss-22 (by ~40%) which is also consistent with further improved dye regeneration yield as Z907 has an additional 100 mV of driving force for this reaction. These combined results are con- sistent with the report by Feldt et al. [14] where they measured regeneration yields for a series of cobalt bipyridine and phenanthroline complexes with similar reorganization energies but different redox potentials in combination with an organic sensitizer. They showed that >0.5 eV driving force is needed to produce efficient dye regeneration, which is only true for the Z907 system here (See Table 5.1).

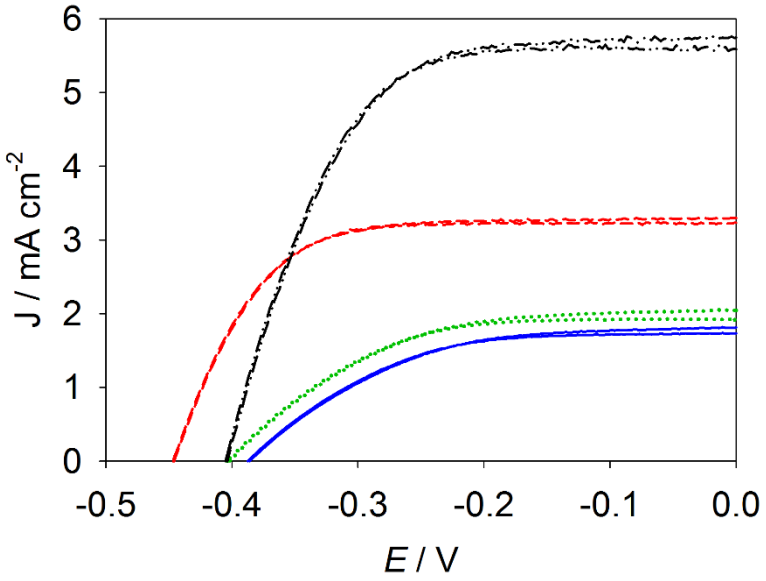

a)

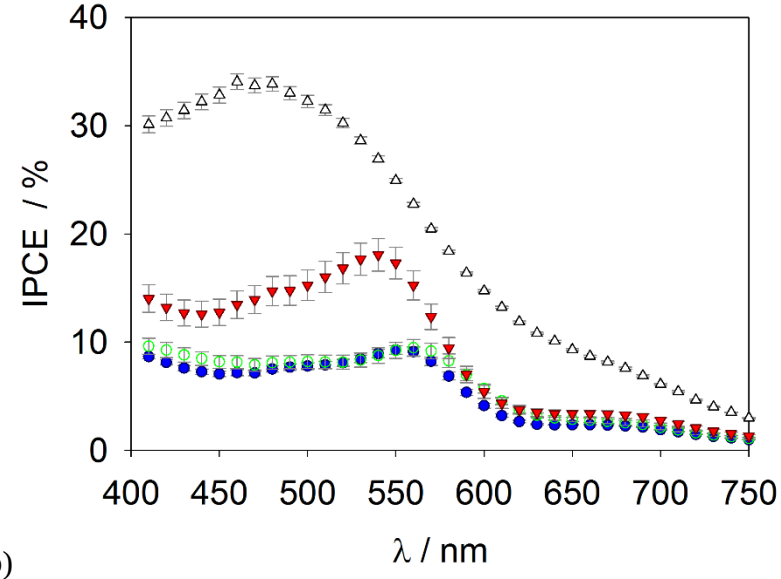

b)

Figure 5.3 a) J-V characteristics, b) spectra of incident photon-to-current conversion efficiency (IPCE) and c) electron lifetime as a function of measured under simulated AM 1.5 G full sun illumination (100mV cm^{-2}) for DSCs based on 1d, ss-14, ss-22 and z907 dyes employing $[Co(dmbpy)_3]^{2+/3+}$ based electrolyte.

Figure 5.3 (cont'd)

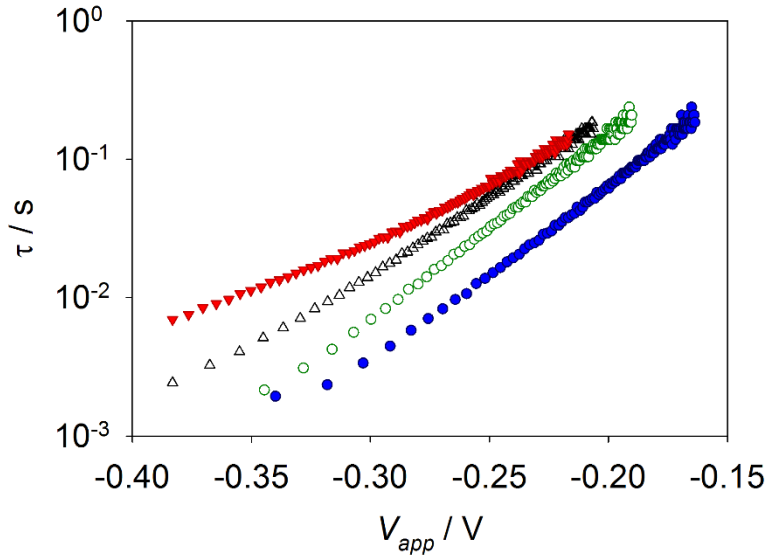

c)

Table 5.1 Current-Voltage characteristics of DSCs employing dyes 1d, ss-14, ss-22 and z907 under simulated AM 1.5 G illumination (100 mW cm^{-2}).

No Alumina	1d	ss-14	ss-22	z907
η (%)	0.38 ± 0.08	0.45 ± 0.11	0.98 ± 0.06	1.33 ± 0.08
J_{sc} (mA cm^{-2})	1.75 ± 0.14	1.96 ± 0.22	3.26 ± 0.17	4.86 ± 0.91
V_{oc} (V)	0.38 ± 0.00	0.39 ± 0.01	0.44 ± 0.01	0.40 ± 0.00
FF	0.55 ± 0.06	0.58 ± 0.07	0.68 ± 0.01	0.72 ± 0.17

We have previously demonstrated that even when recombination blocking nonyl groups are present on sensitizers, recombination to the oxidized redox shuttle can still limit the electron diffusion length and hence the performance. This is clear from comparisons of the magnitude of the lifetimes plotted in Figure. 5.2, which are approximately an order of magnitude too short for efficient charge collection. [15] We therefore also compared the behavior of cells with the different sensitizers in cells where the TiO_2 substrate was coated with an ultra thin coating of alumina via atomic layer deposition (ALD) prior to dye loading. This procedure has been demonstrated to

reduce recombination and thereby improve the efficiency of DSSCs employing alternative redox shuttles. [16] We note that the presence of an alumina layer should also reduce recombination to the oxidized dye. When dye regeneration is efficient such as in optimized DSSCs with an iodide electrolyte – a reduction in dye recombination would not affect the device efficiency. Since dye regeneration is a rate limiting step in the photocurrent production in the systems investigated herein, however, an even larger improvement in efficiency is expected upon the addition of an alumina layer. Figure. 5.2 shows the averaged J–V curves averaged for 3 cells as well as representative electron lifetime plots. Surprisingly, the ss-14 sensitized cells exhibit the same performance as the 1d sensitized cells, even with the addition of alumina. The performances of both cells improve dramatically, however, with an alumina layer, with a 3-fold increase in J_{sc} and a 4-fold increase in efficiency. The same trend of ss-22 outperforming ss-14 and 1d is maintained, and Z907 still is the best performing dye of this series of measurements. The performance of both ss-22 and Z907 improve upon the addition of an alumina layer, but to a lesser extent than ss-13 and 1d, with a 2-fold increase in J_{sc} and a 3-fold increase in efficiency. The smaller improvement for these dyes compared to ss-14 and 1d can be understood by the fact that their performance was less limited by dye regeneration, thus a smaller improvement is possible. Table 5.2 shows the parameters extracted from the measured J–V curves of cells with alumina layer.

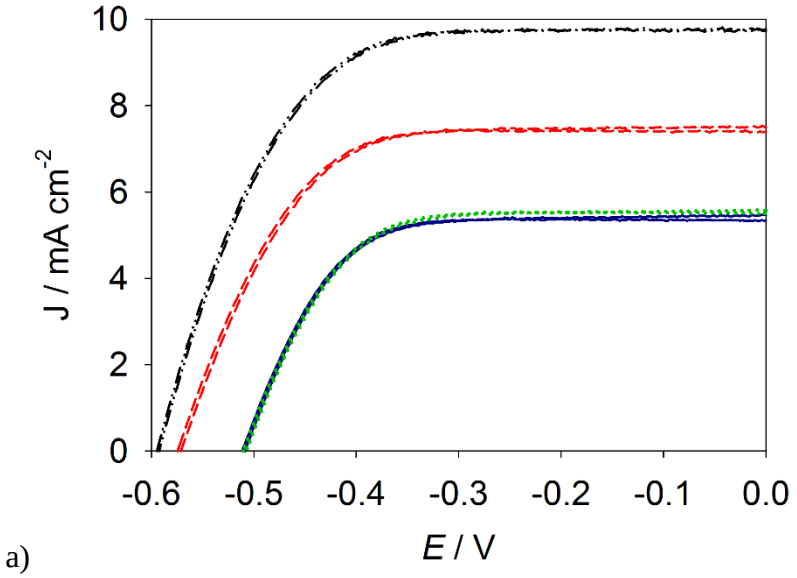

a)

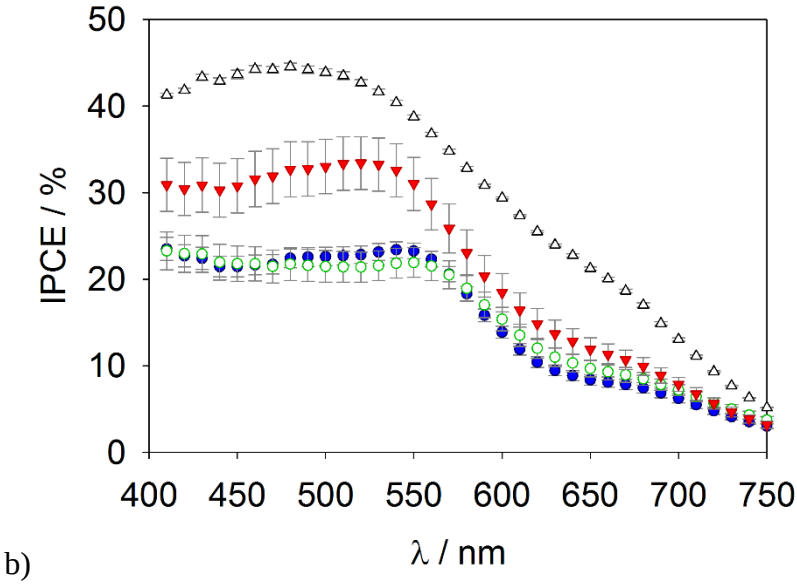

b)

Figure 5.4 a) J-V characteristics, b) spectra of incident photon-to-current conversion efficiency (IPCE) and c) electron lifetime as a function of measured under simulated AM 1.5 G full sun illumination (100mV cm^{-2}) for DSCs based on 1d, ss-14, ss-22 and z907 dyes employing $[Co(dmbpy)_3]^{2+/3+}$ based electrolyte, additional 1 ALD cycle alumina layer was deposited to nanostructured TiO_2 film before dye loading step.

Figure 5.4 (cont'd)

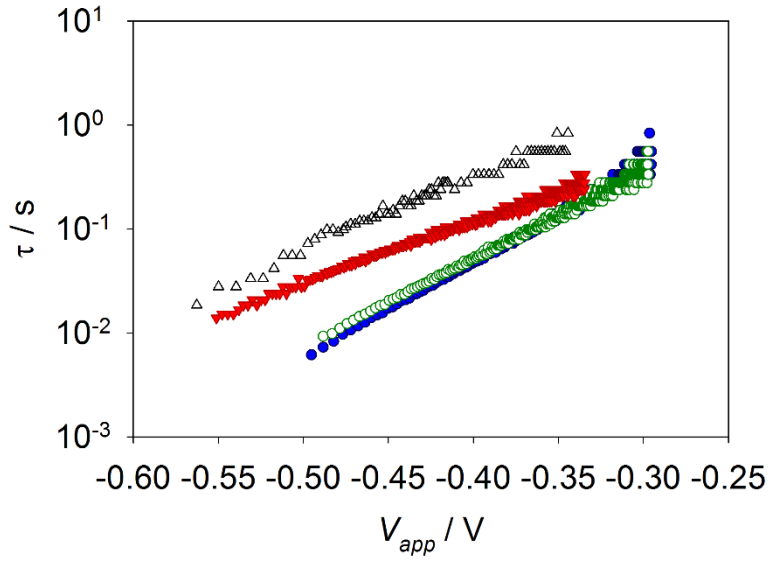

c)

Table 5.2 Current-Voltage characteristics of DSCs employing dyes 1d, ss-14, ss-22 and z907 with additional 1 ALD cycle alumina layer under simulated AM 1.5 G illumination (100 mW cm^{-2})**.**

With Alumina	1d	ss-14	ss-22	z907
η (%)	1.91 ± 0.04	1.94 ± 0.06	2.86 ± 0.20	3.76 ± 0.10
J_{sc} (mA cm^{-2})	5.33 ± 0.15	5.53 ± 0.46	7.44 ± 0.80	9.73 ± 0.08
V_{oc} (V)	0.51 ± 0.00	0.51 ± 0.01	0.57 ± 0.00	0.59 ± 0.02
FF	0.71 ± 0.01	0.69 ± 0.02	0.68 ± 0.02	0.65 ± 0.01

5.5 Conclusions

We successfully synthesized and characterized a relatively simple series of cyclometalated ruthenium dyes with nonyl groups introduced on a bipyridyl ligand to block recombination to outersphere redox shuttles. The goal was to demonstrate that through systematic tuning of the dye properties – the steric bulk in addition to the ground and excited state potentials – the kinetics can be effectively balanced to produce an efficient cell with a given redox shuttle. We were able to show that the introduction of a blocking nonyl group did increase the electron lifetime compared

to a control dye without the nonyl groups, however the ground state potential was also shifted negatively which inhibits regeneration. The poor regeneration was partially overcome by also incorporating fluorine groups on the phenylpyridine ligand which pulled the ground state down by 140 mV, and thus improving the efficiency substantially compared to either the dyes without the electron withdrawing fluorines or nonyl blocking groups. Finally, the performance of cells employing all dyes with the cobalt redox shuttle was still limited by recombination to the oxidized redox shuttle which was further controlled through the introduction of a thin alumina film between the TiO_2 electrode and the sensitizers. Thus, the approach to produce high efficiencies through systematic dye design, combined with electrode modification, was established.

Some surprising results were also observed which warrant further investigations. Despite being structurally very similar, the three dyes with nonyl groups displayed different electron lifetimes. Thus, there are more subtle variables controlling recombination with these dyes than the driving force, which was constant and steric hindrance, which was also essentially constant. One possibility is the dyes have different tunneling barrier heights which Jennings and co-workers showed could modulate recombination to $[Co(bpy)_3]^{3+}$.[17] Alternatively, the different dyes may have different effects on the surface states which can participate in recombination.[18] In any case, the Z907 dye still produced some- what improved performance compared to the best cyclometalated sensitizer investigated here, ss-22, which is likely due to the larger driving force for regeneration. Further modification of the dye molecule, or use of a different redox shuttle which has superior dye regeneration properties, such as $[Co(ttcn)_2]^{2+/3+}$,[6] should allow for further kinetic optimization of a sensitizer-redox system and produce even higher efficiencies, which is a topic of continued investigation in our lab.

REFERENCES

REFERENCES

(1) O'Regan, B.; Grätzel, M. *Nature*. **1991**, *353*, 737–740.

(2) Hamann, T. W.; Ondersma, J. W. *Energy Environ. Sci.* **2011**, *4*, 370.

(3) Yella, A.; Lee, H.-W.; Tsao, H. N.; Yi, C.; Chandiran, A. K.; Nazeeruddin, M. K.; Diau, E. W.-G.; Yeh, C.-Y.; Zakeeruddin, S. M.; Grätzel, M. *Science* **2011**, *334*, 629–634.

(4) Mathew, S.; Yella, A.; Gao, P.; Humphry-Baker, R.; Curchod, B. F. E.; Ashari-Astani, N.; Tavernelli, I.; Rothlisberger, U.; Nazeeruddin, M. K.; Grätzel, M. *Nat. Chem.* **2014**, *6*, 242–247.

(5) Hagfeldt, A.; Boschloo, G.; Sun, L.; Kloo, L.; Pettersson, H. *Chem. Rev.* **2010**, *110*, 6595–6663.

(6) Xie, Y.; Hamann, T. W. *J. Phys. Chem. Lett.* **2013**, *4*, 328–332.

(7) Li, T. C.; Spokoyny, A. M.; She, C.; Farha, O. K.; Mirkin, C. a; Marks, T. J.; Hupp, J. T. *J. Am. Chem. Soc.* **2010**, *132*, 4580–4582.

(8) Tuyet Nguyen, P.; Degn, R.; Thai Nguyen, H.; Lund, T. *Sol. Energy Mater. Sol. Cells* **2009**, *93*, 1939–1945.

(9) Bomben, P. G.; Gordon, T. J.; Schott, E.; Berlinguette, C. P. *Angew. Chem. Int. Ed.* **2011**, *50*, 10682–10685.

(10) Bomben, P. G.; Robson, K. C. D.; Sedach, P. a; Berlinguette, C. P. *Inorg. Chem.* **2009**, *48*, 9631–9643.

(11) Bessho, T.; Yoneda, E.; Yum, J.-H.; Guglielmi, M.; Tavernelli, I.; Imai, H.; Rothlisberger, U.; Nazeeruddin, M. K.; Grätzel, M. *J. Am. Chem. Soc.* **2009**, *131*, 5930–5934.

(12) Chou, C.-C.; Wu, K.-L.; Chi, Y.; Hu, W.-P.; Yu, S. J.; Lee, G.-H.; Lin, C.-L.; Chou, P.-T. *Angew. Chem. Int. Ed. Engl.* **2011**, *50*, 2054–2058.

(13) Bomben, P. G.; Koivisto, B. D.; Berlinguette, C. P. *Inorg. Chem.* **2010**, *49* , 4960–4971.

(14) Feldt, S. M.; Wang, G.; Boschloo, G.; Hagfeldt, A. *J. Phys. Chem. C* **2011**, *115*, 21500–21507.

(15) Ondersma, J. W.; Hamann, T. W. *J. Phys. Chem. C* **2010**, *114*, 638–645.

(16) Klahr, B. M.; Hamann, T. W. *J. Phys. Chem. C* **2009**, *113*, 14040–14045.

(17) Liu, Y. R.; Jennings, J. R.; Zakeeruddin, S. M.; Gratzel, M.; Wang, Q. *J. Am. Chem. Soc.* **2013**, *135*, 3939–3952.

(18) Ondersma, J. W.; Hamann, T. W. *J.* Am. *Chem. Soc.* **2011**, *133*, 8264–8271.

Chapter 6 Future directions for DSSCs

6.1 Introduction

Redox shuttle plays a very important role in determining the performance of DSSCs. Utilizing outer-sphere redox shuttle systems, e.g. cobalt based redox shuttles, allows extensive research to identify the key efficiency limitations in DSSCs, especially regeneration and recombination. Therefore, innovative design concepts can be developed for advancing high efficiency of DSSCs.

Because the power conversion efficiency of a solar cell, η, is the ratio of the maximum electrical power output, P_{max}, to the incident light power, P_{in}. The maximum electrical power output is the product of the photocurrent density and the voltage at the power point, which can be described as:[1]

$$\eta = \frac{P_{\max}}{P_{in}} = \frac{J_{sc} \times V_{oc} \times ff}{P_{in}}$$

where J_{sc} is the short circuit photocurrent density, V_{oc} is the open-circuit photovoltage, and ff is the fill factor. Changing the redox shuttle will have different effects on each parameter. J_{sc} is proportional to IPCE which is a function of light harvest efficiency, η_{LHE}, dye injection, η_{inj}, and regeneration efficiency, η_{reg}, as well as charge collection efficiency. In previous chapters, the key important parameter, η_{reg}, in IPCE has been discussed extensively. Quantitative regeneration efficiency can be achieved employing low spin cobalt redox shuttles, thus increasing IPCE which ultimately represented as improved photocurrent, J_{sc}. Open circuit voltage is related to the difference between the Nernstian potential of the electrolyte solution, E_{redox}, and the quasi-Fermi level in the semiconductor, E_F. Higher voltage can be potentially achievable by using redox shuttles with more positive potentials,[2] however, more offset of photocurrent might be introduced owing to increased recombination. Therefore, in order to maximize the overall power conversion

efficiency, one interesting DSSCs design strategy would be using redox shuttle potential which can offer quantitative regeneration but avoid fast recombination coherently despite of more positive redox potential.

6.2 Redox shuttles for high open circuit voltage

Ondersma and Hamann observed surface state dominated electron recombination in DSSCs using Redox shuttle, $[Ru(bpy)_2(MeIm)_2](PF_6)_2$ (bpy = 2,2'-bipyridine, MeIM= bis(2,20-bipyridyl)-bis(N-methylimidozole)).[3] The redox shuttle has a potential of 0.89 V vs AgCl. Slow electron recombination from conduction band due to Marcus inverted behavior is noted by using redox shuttle with such positive potential. If the challenges of surface mediated recombination can be suppressed, developing alternative fast outer-sphere redox shuttles with very positive potential can be another attractive route to high efficiency DSSCs. Later in 2015, Jiang and Zhou used redox shuttles $[Ru(bpy)_2(MeIm)_2]^{3+/2+}$ and $[Ru(bpy)_2(SCN)_2]^{+/0}$ to pair with sensitizers $Ru(bpy)_2(dcbpy)$ (dcbpy = 4,4-dicarboxy-2,2-bipyridine) and $Ru(dcbpy)_2(NCS)_2$ (N3 dye), respectively. A short circuit current of 4 mA cm^{-2} and an open circuit voltage of 0.9 V were achieved using $[Ru(bpy)_2(MeIm)_2]^{3+/2+}$ at small dye regeneration driving force of 0.07 eV. These results are promising though the performance is yet limited by the solubility of the redox shuttles and semiconductor material preparation. In other words, there is still plenty of room to optimize the system. Complexes $[Co(9S_2O)_2]^{3+/2+}$ is reported to be low spin Co(II)/(III) redox shuttle,[4] owing to the structural similarity to low spin $[Co(ttcn)_2]^{3+/2+}$, a similar total reorganization energy, λ, at semiconductor/liquid interface of ~1.234 eV can be expected. The redox potential of the redox shuttle is 0.574 V vs Ferrocene, thus producing a driving force, $-\Delta G$, of -1.734 eV for electron recombination from conduction band if at condition where the conduction band energy ~0.8V vs AgCl.[5] Therefore, an inverted region can be reached for the redox shuttle because $-\Delta G > \lambda$. In

addition, the advantages of low spin cobalt redox shuttles have been discussed in detail in chapter 2-3 (fast electron transfer enables quantitative regeneration.) and in chapter 4 (other design routes to overcome charge collection limitations and tune the redox potential is offered.). $[Co(9S_2O)_2]^{3+/2+}$ enjoys the advantages of low spin $[Co(ttcn)_2]^{3+/2+}$, meanwhile, low charge collection which limits the performance of $[Co(ttcn)_2]^{3+/2+}$ might be eliminated provided that recombination is not conduction band electron recombination dominated owing to the inverted region effect. The synthesis of $[Co(9S_2O)_2]^{3+/2+}$ is easy and solubility of the complex can be tuned via varying counter ion species. Unlike $[Ru(bpy)_2(MeIm)_2]^{3+/2+}$ which shows competitive light absorption to sensitizers, $[Co(9S_2O)_2]^{3+/2+}$ displays less competitive light absorption with absorption at about 500 nm ($\varepsilon < 200\ M^{-1}cm^{-1}$).[4] $[Co(9S_2O)_2]^{3+/2+}$ hence can be a great alternative redox shuttle in producing high voltage and efficient photocurrent generation as well as expanding the low spin redox shuttle family to a wider range of potentials.

6.3 Tandem redox systems

Currently, most DSSCs relies on a single redox system where only one pair of redox shuttles is used in the electrolyte. High spin cobalt based redox shuttles, e.g. $[Co(bpy)_3]^{3+/2+}$ used in champion DSSCs,[6] has many advantages such as good stability, minimal competitively absorption, highly tunable structures et al. One of the most important feature is the relatively slow recombination result from slow electron transfer induced by large inner-sphere reorganization energies. However, this feature gives a contrary effect on regeneration by reducing the regeneration rate. Low spin cobalt redox shuttles can address the slow regeneration issue that refrained the performance of cobalt redox shuttle from being optimal. Nevertheless, fast recombination becomes an associated issue of fast electron transfer though regeneration can be improved.[7,8] It would be advantageous to integrate the advantages of high spin and low spin redox

shuttles into one system, avoiding the drawbacks of the two systems meanwhile. In summary, the idea is to build a tandem redox system. Cong and Kloo[9] reported a tandem redox systems based on TEMPO-Co redox shuttles, where TEMPO is 2,2,6,6-tetra-methyl-1-piperidinyloxy and Co represents $[Co(bpy)_3]^{3+/2+}$. The tandem redox shuttles outperform the single cobalt redox shuttle system. High J_{sc}, V_{oc} and η are observed, and transient measurements indicated an increased regeneration rate in the tandem redox system. An electron transfer process was proposed in the tandem redox system as bellow:

$$TEMPO + D^{+} \rightarrow TEMPO^{+} + D$$

$$TEMPO^{+} + Co^{2+} \rightarrow Co^{3+} + TEMPO$$

$$Co^{3+} + e^{-} \rightarrow Co^{2+}$$

The proposed regeneration mechanism is beneficial in improving the regeneration rate for efficient regeneration. Additionally, absence of acceptor form of TEMPO diminishes fast recombination in single TEMPO redox system. Therefore, improvements to high spin cobalt systems should also be expected by substituting TEMPO with other fast redox shuttle, such as low spin cobalt redox shuttles. Besides low spin Co(II)/(III) based redox shuttles, Co(III)/(IV) is also quite attractive. Both Co(III) and Co(IV) complexes are low spin, removal of an electron from the t_{2g} orbital in Co(III) results in little structural change on the electron-transfer to Co(IV). Fukuzumi, *et al*[10] studied the electron self-exchange rates between $(DH)_2Co^{III}(Me)(Py)$ and $[(DH)_2Co^{IV}(Me)(Py)]^{+}$(DH^{-} = the anion of dimethylglyoxime, Py, pyridine, Me, methyl), their result showed that the rate constant of the electron self-exchange reaction is $8.4\times10^{8}\ M^{-1}\ s^{-1}$. The fast self-exchange rate constant of Co(III)/(IV) is resulted from small inner-reorganization energy, thus demonstrates great potential application as a fast redox shuttle. However, the complex

structure reported by Fukuzumi cannot be easily tuned. There are other choices of Co(III) complexes with more tunable structure. $Co(ppy)_3$ (ppy = phenylpyridine) reported by Thomspon[11] has a redox potential of 0.82 V vs NHE. Owing to the cyclometalated structure feature, the redox potential can also be controlled by varying the substitute on the ligand. Considering about 8 orders of magnitude faster self-exchange rate constant of Co(III)/(IV) as compared to high spin Co(II)/(III) redox systems. The dye regeneration rate can be estimated to be >300 times faster using Marcus cross relation despite a ~0.3 eV less driving force. Therefore, combining the Co(III) complex with high spin cobalt redox shuttles as tandem redox system is a promising strategy in redox system design for DSSCs.

6.4 Experimental

6.4.1 Synthesis of cobalt complexes

[*fac*-$Co^{III}(ptpy)_3$] (ptpy = 2-(p-tolyl)-pyridinato-*N*, C^2). The compound was synthesized in a similar manner as reported in literature.[11] Firstly, 12mL mesitylene magnesium bromide solution was cooled to -30 ^oC, and a solution of $CoBr_2$ (0.92 g, 4.20 mmol) in THF (9 mL) was then added slowly. Throughout the addition the color of the reaction mixture changed from clear yellow to opaque ochre and finally to yellow and black. The cooling bath was removed, and the mixture was stirred for 1h. 2-(p-tolyl)-pyridine (2.39 g, 14.1 mmol) was then added, and the reaction was brought to a gentle reflux at 120^o C for 8h. The reaction mixture was added to aqueous NH_4Cl (10 g/L, 75 mL) and CH_2Cl_2 (75 mL) mix. The resulting thick emulsion was filtered and transferred to a separatory funnel. The organic layer was isolated, and the aqueous layer was extracted twice with CH_2Cl_2. All organic portions were combined, dried over anhydrous $CaSO_4$ for 30min, filtered, and concentrated under reduced pressure. Addition of hexanes to the brown concentrate precipitated a dark yellow solid. ^1H NMR spectroscopy indicated that the crude sample was a

mixture of facial and meridional isomer. Pure facial isomer was obtained by column chromatography in silica gel using CH_2Cl_2 as eluent followed by vacuum sublimation. ^{1}HNMR (500 MHz, CDCl3): δ 7.81 (d, 1H, J = 5.0 Hz), 7.61 - 7.59 (t, 1H, J = 5.0 Hz), 7.55 (d, 1H, J = 5.0 Hz), 7.20 (d, 1H, J = 5.0 Hz), 6.80 - 6.78 (t, 1H, J = 5.0 Hz), 6.73 (d, 1H, J = 5.0 Hz), 6.35 (s, 1H), 2.09 (s, 3H). MS: m/ e 563 (M^+). Elemental analysis for $CoC_{36}H_{30}N_3$: Calculated: C, 76.72; H, 5.36; N, 7.46; Found: C, 76.67; H, 5.44; N, 7.49.

$[Co^{II}(9S_2O)_2](BF_4)_2$ ($9S_2O$ = 1-oxa-4,7-dithiacyclononane). This complex was synthesized following literature reported method.[4] The ^{1}HNMR spectrum of the ligand is also included in the appendix, see figure 6.6. Elemental analysis for $CoC_{12}H_{24}S_4O_2B_2F_8$: Calculated: C, 25.69; H, 4.31; N, 0; Found: C, 24.96; H, 4.30; N, 0.03.

$[Co^{III}(9S_2O)_2](BF4)_3$. The complex was synthesized by adding equivalent amount oxidant $NOBF_4$ to stirring solution of $[Co(9S_2O)_2]$ $(BF_4)_2$ in nitromethane. After 1.5 hour, the solution was concentrated using rotvap, futher addition of ether to the concentrate yield pink precipitate. Elemental analysis for $CoC_{12}H_{24}S_4O_2B_3F_{12}$: Calculated: C, 22.24; H, 3.73; N, 0; Found: C, 21.87; H, 3.61; N, 0.13.

6.4.1 Electrochemistry

The redox shuttle, $[Co(9S_2O)_2]$ $(BF_4)_2$, was successfully synthesized. The cyclic voltammetry of the redox shuttle gives a redox potential of -0.611 V vs Fc which is in excellent agreement with literature reported values as shown in figure 6.1. Scan rate dependency study indicated a quasi-reversible electron transfer at gold electrode surface for the redox shuttle indicated by a slightly smaller ratio of anodic (oxidation) and cathodic (reduction) current, shown in figure 6.2.

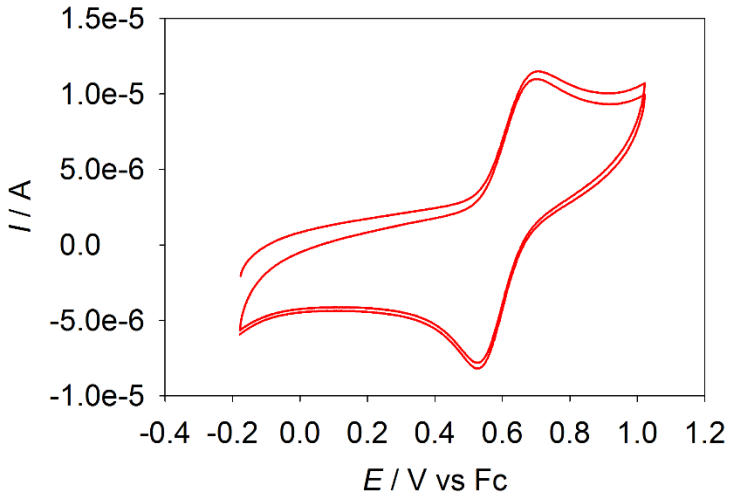

Figure 6.1 Cyclic voltammogram of $[Co(9S_2O)_2]$ $(BF_4)_2$ in nitromethane. Working electrode: gold disk, Counter Electrode: Pt mesh, RE: commercial no-leak AgCl, supporting electrolyte: 0.1 M LiTFSI, ferrocene was used as an internal standard.

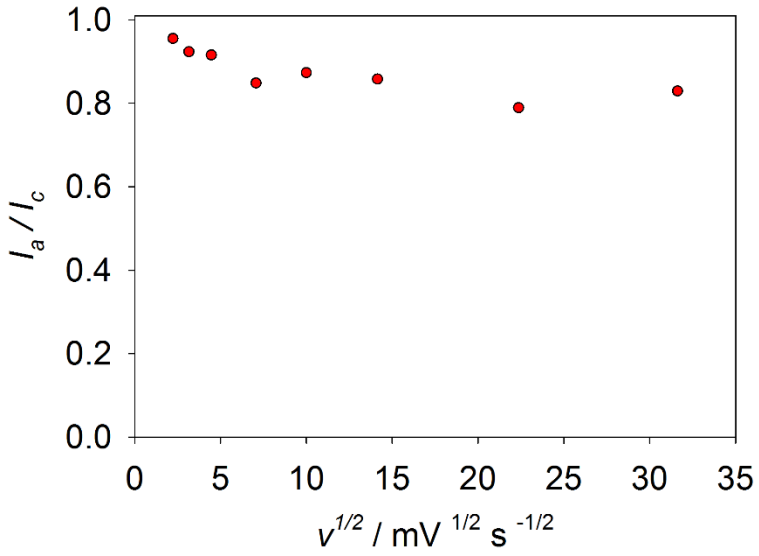

Figure 6.2 Plot of anodic/cathodic (I_a / I_c) peak current ratio of $[Co(9S_2O)_2](BF_4)_2$ in nitromethane.

The Co(III) complex $Co(ptpy)_3$ (ptpy = 2-(p-tolyl)-pyridine), was successfully synthesized and NMR spectrum is included in the appendix, see figure 6.5. The cyclic voltammetry of the redox shuttle gives a redox potential of 0.144 V vs Fc which is slightly negative to literature reported

values of 0.190 V vs Fc for $Co(ppy)_3$, see figure 6.3. The result suggests the redox potential of the Co(III)/(IV) tris-phenylpyridine complex can be tuned in a similar manner as the well-known high spin Co(II)/(III) cyclometalated complexes, e.g. $[Co(bpy)_3]^{3+/2+}$. Scan rate dependency study indicated a reversible electron transfer at gold electrode surface for the redox shuttle indicated by a ratio of anodic (oxidation) and cathodic (reduction) current close to 1, shown in figure 6.4.

In summary, these preliminary results on the complexes opens up more choices of outer-sphere redox shuttles which has great potential via structure design and various tandem combinations. It is a continued interest of our group on exploring alternative outer-sphere redox shuttles with novel characteristic to deal with the dual energy constraints of regeneration and recombination in combination with novel semiconductor materials and sensitizers.

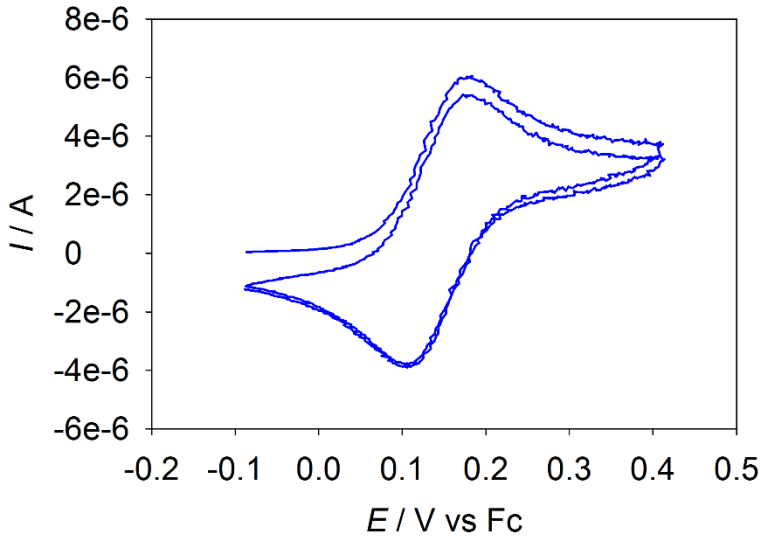

Figure 6.3 Cyclic voltammogram of $Co^{III}(ptpy)_3$ in acetonitrile. Working electrode: gold disk, supporting electrolyte: 0.1 M $TBAPF_6$, counter electrode: Pt mesh, ferrocene was used as an internal standard.

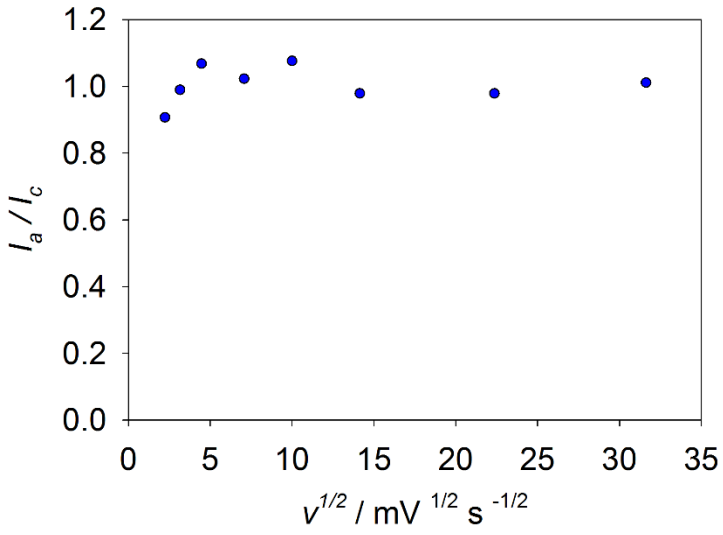

Figure 6.4 Plot of anodic/cathodic (I_a / I_c) peak current ratio of $Co(ptpy)_3$ in acetonitrile.

APPENDIX

APPENDIX

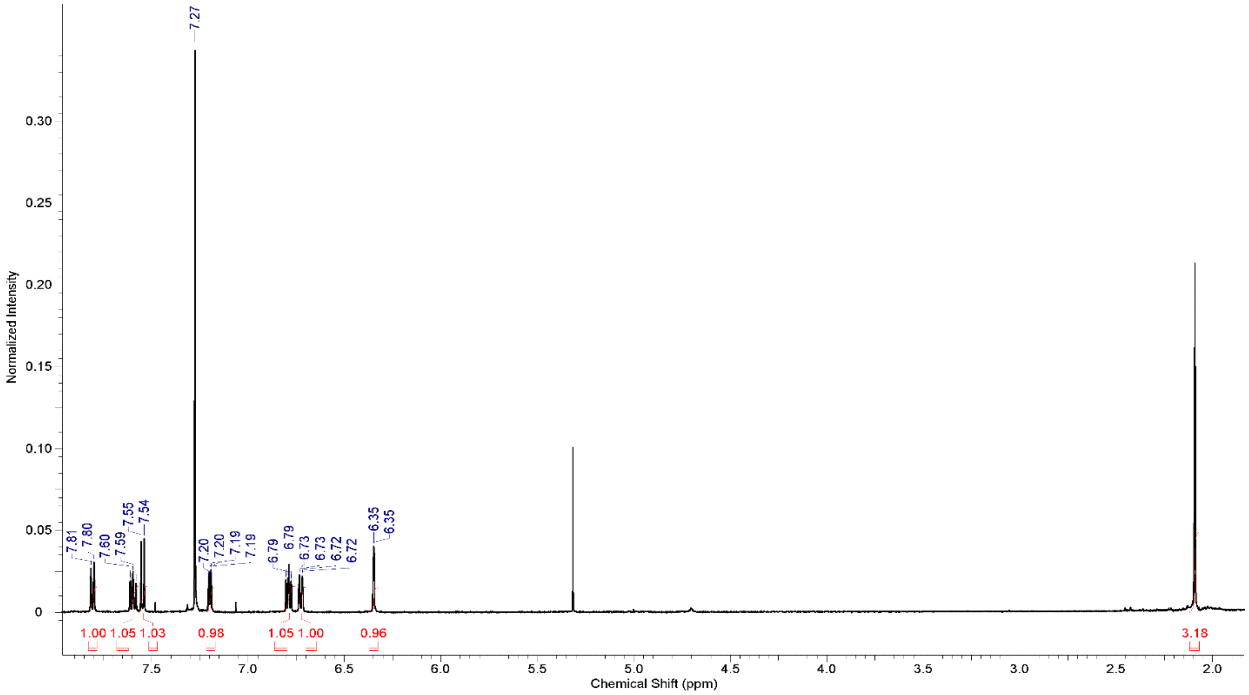

Figure 6.5 ^{1}HNMR spectrum of $Co(ptpy)_3$ in $CDCl_3$.

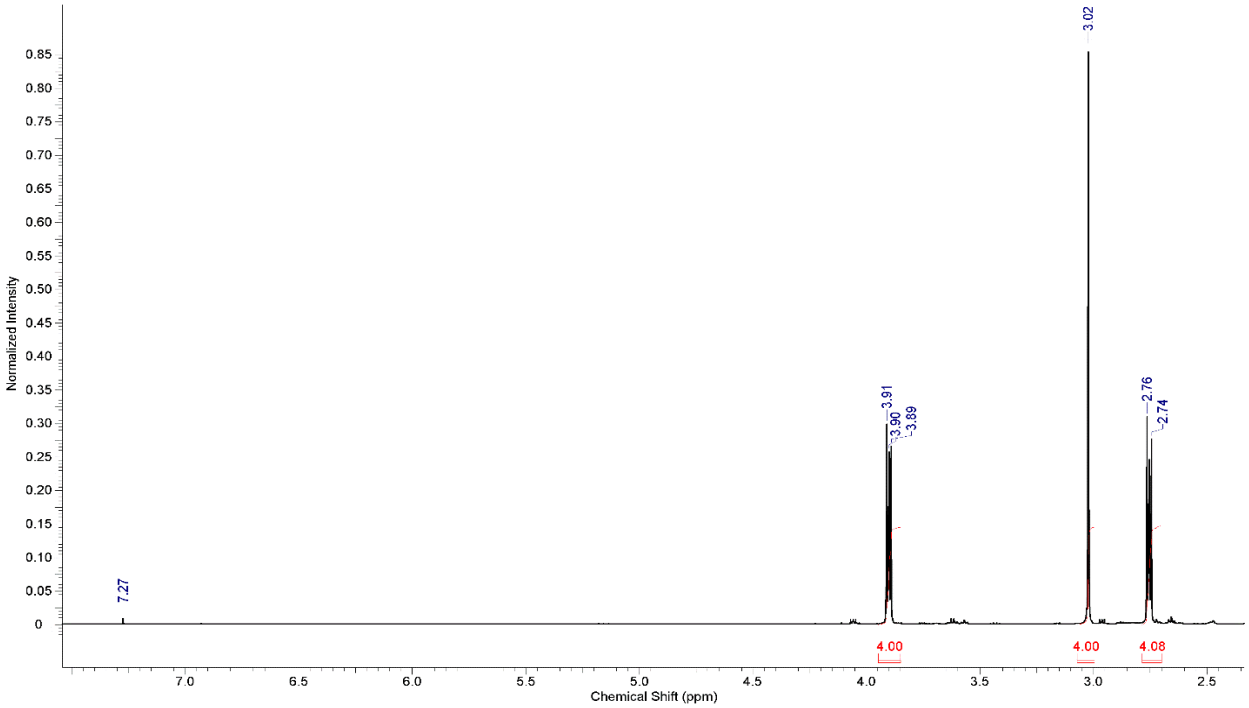

Figure 6.6 1HNMR spectrum of 9S2O in $CDCl_3$.

REFERENCES

REFERENCES

(1) Hamann, T. W.; Ondersma, J. W. *Energy Environ. Sci.* **2011**, *4*, 370.

(2) Yum, J.-H.; Baranoff, E.; Kessler, F.; Moehl, T.; Ahmad, S.; Bessho, T.; Marchioro, A.; Ghadiri, E.; Moser, J.-E.; Yi, C.; Nazeeruddin, M. K.; Grätzel, M. *Nat. Commun.* **2012**, *3*, 631.

(3) Ondersma, J. W.; Hamann, T. W. *J. Am. Chem. Soc.* **2011**, *133*, 8264–8271.

(4) Grant, G. J.; Jones, M. W.; Loveday, K. D.; VanDerveer, D. G.; Pennington, W. T.; Eagle, C. T.; Mehne, L. F. *Inorganica Chim. Acta* **2000**, *300-302*, 250–263.

(5) Ondersma, J. W.; Hamann, T. W. *Energy Environ. Sci.* **2012**, *5*, 9476–9480.

(6) Mathew, S.; Yella, A.; Gao, P.; Humphry-Baker, R.; Curchod, B. F. E.; Ashari-Astani, N.; Tavernelli, I.; Rothlisberger, U.; Nazeeruddin, M. K.; Grätzel, M. *Nat. Chem.* **2014**, *6*, 242–247.

(7) Xie, Y.; Hamann, T. W. *J. Phys. Chem. Lett.* **2013**, *4*, 328–332.

(8) Xie, Y.; Baillargeon, J.; Hamann, T. W. *J. Phys. Chem. C* **2015**, *119*, 28155-28166.

(9) Cong, J.; Hao, Y.; Boschloo, G.; Kloo, L. *ChemSusChem* **2015**, *8*, 264–268.

(10) Ohkubo, K.; Fukuzumi, S. *J. Phys. Chem. A* **2005**, *109*, 1105–1113.

(11) Ren, X.; Alleyne, B. D.; Djurovich, P. I.; Adachi, C.; Tsyba, I.; Bau, R.; Thompson, M. E. *Inorg. Chem.* **2004**, *43*, 1697–1707.